

# Lampray: Multi-group long characteristics ray tracing for adaptive mesh radiation hydrodynamics

Troels Frosthholm,<sup>1\*</sup> Troels Haugbølle,<sup>1†</sup> and Tommaso Grassi,<sup>1,2,3‡</sup>

<sup>1</sup>Centre for Star and Planet Formation, Niels Bohr Institute, and Natural History Museum of Denmark, University of Copenhagen, Øster Voldgade 5–7, DK-1350 Copenhagen, Denmark

<sup>2</sup>Universitäts-Sternwarte München, Scheinerstr. 1, DE-81679 München, Germany

<sup>3</sup>Excellence Cluster Origin and Structure of the Universe, Boltzmannstr. 2, DE-85748 Garching bei München, Germany

in original form 2018 September XX

## ABSTRACT

We present LAMPRAY: a multi-group long characteristics ray tracing method for adaptive mesh radiation hydrodynamics in the RAMSES code. It avoids diffusion, captures shadows, and treats colliding beams correctly, and therefore complements existing moment-based ray tracing in RAMSES. LAMPRAY includes different options for interpolation between ray and cell domain, and use either integral, Fourier, or an implicit C2RAY method for hydrogen ionization to solve the radiative transfer. The opacity can either be tabulated or computed through a coupling to the general non-equilibrium astro-chemistry framework KROME. We use an H-He-C-O network with 36 species and 240 reactions to track the photo-chemistry in the interstellar medium across 6 and 10 orders of magnitude in temperature and density. Self-shielding prescriptions for H<sub>2</sub> and CO are used together with a new model for the diffuse interstellar UV-field. We also track the dust temperature, formation of H<sub>2</sub> on grains, and H<sub>2</sub>O and CO ices in detail. LAMPRAY is tested against standard benchmarks for molecular cloud and star formation simulations, including the formation of a Strömgren sphere, the expansion of an ionization front, the photo-evaporation of a dense clump, and the H-He-C-O chemistry in a static photo-dissociation front. Efficient parallelisation is achieved with a separate domain decomposition for rays where points along a ray reside in the same memory space, and data movement from cell- to ray-domain is done with a direct hash-table lookup algorithm. Point sources are treated without splitting rays, and therefore the method currently only scales to a few point sources, while diffuse radiation has excellent scaling.

**Key words:** radiative transfer – astrochemistry – ISM: abundances – ISM: HII regions

## 1 INTRODUCTION

The interaction between radiation and matter is important for a majority of objects in the Universe, and often required for accurate, quantitative numerical modelling in astrophysics. In the interstellar medium (ISM) the role of radiative stellar feedback versus feedback from supernovae and galactic dynamics is debated (Dale et al. 2013; Krumholz et al. 2014; Padoan et al. 2016; Peters et al. 2017; Butler et al. 2017; Howard et al. 2017). Numerical models that can address several of these issues at once are therefore needed to explore the importance of the different effects.

Star forming regions harbour a complex filamentary distribution of gas and dust driven by supersonic turbulence. They can be observed through the thermal emission from cold dust, and in atomic and molecular line transitions, but observations only provide a two-dimensional projected snapshot in time. Due to the complex nature of the system synthetic observations of numerical models that can aid in interpreting the observations and unravel what are the dominating physical processes at play, are highly desirable (Haworth et al. 2018). Connecting numerical models to observations requires accurate modelling of the chemistry and radiation field. Many tools exist to post process models creating dust and line radiation maps, but either assumed or calculated chemical abundances have to be provided as input. In star forming regions, in particular close to pre-stellar cores, the chemical equilibrium time scale can be longer than the dy-

\* Contact e-mail: frosthholm@nbi.ku.dk

† Contact e-mail: haugboel@nbi.ku.dk

‡ Contact e-mail: tgrassi@usm.lmu.de

namical time scale, and assuming chemical and radiative equilibrium is in many cases not a good assumption. Consequently it is useful to treat the non-equilibrium chemical evolution directly in the numerical model. At lower optical depths and in the vicinity of protostars the chemistry is to a large extent controlled by the radiation, and a proper model therefore requires a solution of both radiative transfer and photo-chemistry.

On smaller scales the collapse of dense clouds, the formation of protostellar systems and accretion on to the protostar is controlled by the environment in which it takes place (Kuffmeier et al. 2017), as well as by several physical processes including magnetic fields, radiative heating and cooling, and thermal and radiative ionization (Tan et al. 2014). The formation of a possibly rotationally stable first core is controlled by radiative cooling in changing opacity regimes, and its subsequent evolution is affected by radiative heating from the accretion shock on the forming protostar (Vaytet & Haugbølle 2017). The protoplanetary disc surface temperature and degree of ionization is to a large degree controlled by radiation from the protostar, and the inner thermal structure by radiative and turbulent diffusive heat transport (Dullemond & Monnier 2010). Massive protostars are sources of copious high-energy radiation, launch radiatively driven disc winds, and ionize their immediate surroundings creating HII regions (Peters et al. 2010). Radiative transfer is therefore desirable for detailed modelling of protostellar systems in different evolutionary stages and in particular at high masses.

In molecular clouds the energy cascades from large to small scales, generating a roughly self-similar structure down to the collapsing cores. This process is multi-scale in nature, coupling the dynamics of molecular clouds at the tens of pc scale to proto-planetary systems through the accretion history and magnetic field anchoring. The gravitational collapse channels gas through a disc to the star, in a delicate balance with the environment. The connection of scales in the above processes can only be addressed with adaptive multi-scale mesh or meshless numerical methods (Kuffmeier et al. 2017).

RAMSES (Teyssier 2002) is a multi-physics oct-based adaptive mesh refinement code for astrophysics, which is used by a large community. An abundance of radiative transfer codes have been implemented in RAMSES. ATON (Aubert & Teyssier 2008) is a time-dependent radiative transfer tool for cosmic reionization based on the M1 moment method, used in conjunction with RAMSES. Both flux-limited diffusion (González et al. 2015; Commerçon et al. 2014, 2011) and the M1 method (Rosdahl et al. 2013; Rosdahl & Teyssier 2015) have been implemented on adaptive mesh for use in radiation-hydrodynamics. RAYRAMSES (Barreira et al. 2016) is a ray-tracing tool for post-processing of cosmological simulations using curved rays to capture gravitational lensing, while Valdivia & Henebelle (2014) provide an algorithm to estimate column densities taking advantage of the fully threaded tree in RAMSES.

In this paper we present a new algorithm for radiative transfer in RAMSES that we call LAMPFRAY: Long characteristics AMr Parallel RAY tracing. It stands out from the current radiative transfer algorithms in RAMSES in two key aspects: Firstly it is a multi-group long characteristics ray tracing method, allowing for an accurate treatment of shad-

ows and colliding beams. Secondly it is coupled to the non-equilibrium chemistry code KROME, enabling relatively easy construction of complex photo-chemical models.

There already exists a number of algorithms for parallel ray tracing radiation hydrodynamics (RHD) on adaptive meshes. Wise & Abel (2011) introduced ray tracing RHD from point sources on the block adaptive mesh of the ENZO code, using adaptive ray tracing (Abel & Wandelt 2002), where the set of directions being traced from the source are split as the distance grows to maintain a high angular resolution. Rijkhorst et al. (2006) did the same for the FLASH code, also on a block AMR grid, using so-called hybrid characteristics, where the local radiation field is found on blocks using long characteristics, and these are connected with short characteristics between blocks. Bunttemeyer et al. (2016) extended this method to the diffuse radiation field component. These methods are however unsuited for RAMSES' octree grid due to the high computational cost of looking up neighbour cells. Also worth mentioning is the TRECOCOL method by Clark et al. (2012), which estimates column depths by tracing along HEALPIX directions in an octree. LAMPFRAY has been carefully optimised for running at scale with a hash-table based ray tracing algorithm and uses a dual parallel decomposition where the solution of the radiative transfer is performed in a separate ray-centric domain with near-perfect parallel load-balancing. The implementation is modular and contains several different modules for solving the radiative transfer along the rays, for computing the opacities, and for applying the result to gas heating/cooling, chemistry etc.

In section 2 we describe the numerical methods used for solving radiation hydrodynamics with an emphasis on the equation of radiative transfer, photo-chemistry, and gas heating/cooling. Section 3 describes the implementation of ray tracing, how the change of domain decomposition and scaling is achieved, and how boundary conditions are handled. Section 4 checks the validity of the code in a number of benchmark simulations, performance, and scaling is reported in section 5, while section 6 summarises our method and discusses future applications.

## 2 NUMERICAL METHODS

Radiation hydrodynamics model the interaction and evolution of radiation and matter with a fluid description. Radiation can transport energy and momentum through emission, absorption, and scattering. In addition, when high-energy photons are present radiation has important consequences for the chemical composition of the gas, and the photo-chemistry can drive the gas out of local thermal equilibrium. A comprehensive description of radiation hydrodynamics therefore contains three main components: *hydrodynamics*, *radiative transfer*, and *chemical evolution*.

*Hydrodynamics* describes the bulk transport and mixing of matter and is captured in the equations for conservation of mass and species, balance of energy, and the Navier-Stokes equation for the momentum. Written in conservative form

they are

$$\frac{\partial \rho}{\partial t} + \nabla \cdot [\rho \mathbf{u}] = 0 \quad (1)$$

$$\frac{\partial \rho X_s}{\partial t} + \nabla \cdot [\rho X_s \mathbf{u}] = m_s (F_s - D_s) \quad (2)$$

$$\frac{\partial \rho \mathbf{u}}{\partial t} + \nabla \cdot [\rho \mathbf{u} \otimes \mathbf{u} + P \mathbb{I}] = 0 \quad (3)$$

$$\frac{\partial \rho e_{\text{tot}}}{\partial t} + \nabla \cdot [(\rho e_{\text{tot}} + P) \mathbf{u}] = \Gamma_{\text{gas}} - \Lambda_{\text{gas}}, \quad (4)$$

where  $\rho$  is the density,  $\mathbf{u}$  the velocity,  $X_s$  the mass abundance,  $m_s$  the mass, and  $F_s$ ,  $D_s$  the rates of formation and destruction of species  $s$ . The corresponding number density is  $n_s = \rho X_s / m_s$ .  $P$  is the gas pressure,  $\rho e_{\text{tot}}$  is the total energy density of the fluid, which is the sum of the internal energy density  $e_{\text{int}}$  and the kinetic energy density

$$\rho e_{\text{tot}} = \rho e_{\text{int}} + \frac{1}{2} \rho u^2, \quad (5)$$

and  $\Gamma_{\text{gas}}$ ,  $\Lambda_{\text{gas}}$  are the total volumetric heating and cooling rates describing the exchange of energy from other processes, such as release and storage of chemical energy, and absorption or emission of radiation. We assume that the equation of state is that of an ideal gas relating the pressure and internal energy as  $P = (\gamma - 1)e_{\text{int}}$ , but allow the adiabatic index to be a function of the state and composition of the gas  $\gamma(\rho, T, X_s)$ . The gas temperature is related to the pressure as  $P = n_{\text{gas}} k_B T$ , and the total number density can be found from the density and abundances as  $\rho = \mu n_{\text{gas}}$ . The molecular weight of the gas is  $\mu = 1 / (\sum X_s / m_s)$ .

LAMPRAY does not compute the radiative pressure and momentum, and we have for clarity left out other contributions from e.g. magnetic fields, self-gravity, and external forces, which are included in RAMSES.

The dynamical time-scale of the fluid is dictated by the bulk motion and the speed of sound. The chemistry, contained in the terms  $F_s$ ,  $D_s$ , often evolves on a different and faster time-scale, and the same is true for the radiation, which affects the chemistry. The chemistry and the radiation determine the heating and cooling. In RAMSES we assume a decoupling between the three components and use operator splitting, to avoid evolving the hydrodynamics on the much shorter time-scale of the other processes, which would be prohibitively expensive in three dimensional models. First, the *hydrodynamics* is evolved with a single explicit hydrodynamical timestep, disregarding the source terms, corresponding to setting  $F_s = D_s = \Lambda_{\text{gas}} = \Gamma_{\text{gas}} = 0$  in the equations above. Then, the *radiative transfer* is calculated with LAMPRAY. The chemical species,  $\rho X_s$ , and the average radiation field together with the temperature in each computational cell is then used as an input for the *chemical evolution* and the heating and cooling. KROME is used to evolve the species,  $\rho X_s$ , and compute the change in the temperature,  $T$ . If a model is run without chemistry,  $\Gamma_{\text{gas}} - \Lambda_{\text{gas}}$  is obtained directly from the radiative transfer.

*Radiative transfer* is the flow of photons through a medium governed by a transport equation, which includes the advection of photons in a given direction  $\mathbf{n}$  and the absorption and emission of new photons, described by the extinction coefficient  $\alpha_\nu$  and emissivity  $j_{*,\nu}$  at frequency  $\nu$ . We are interested in radiation in the ISM and around new-born stars, and the light-crossing time is much lower than the

dynamical time, which in a non-cosmological setting corresponds to having non-relativistic velocities. LAMPRAY therefore solves the time-independent equation of radiative transfer

$$\mathbf{n}(\mathbf{x}) \cdot \nabla I_\nu(\mathbf{x}, \Omega) = j_{*,\nu}(\mathbf{x}) - \alpha_\nu(\mathbf{x}) I_\nu(\mathbf{x}, \Omega), \quad (6)$$

where  $I_\nu(\mathbf{x}, \Omega)$  is the intensity in a direction  $\Omega$  at a point  $\mathbf{x}$ , and we have neglected scattering. The mean intensity, which is the main input to compute the effect of radiation on matter, is

$$J_\nu(\mathbf{x}) = \frac{1}{4\pi} \int_0^{4\pi} I_\nu(\mathbf{x}, \Omega) d\Omega, \quad (7)$$

while the intensity of the emitted radiation is given by the source function

$$S_\nu(\mathbf{x}) = \frac{j_{*,\nu}(\mathbf{x})}{\alpha_\nu(\mathbf{x})}. \quad (8)$$

Using the non-dimensional optical depth  $d\tau_\nu = \alpha_\nu d\mathbf{x}$  that measures the fractional decrease in intensity we can rewrite Eqn.(6) along a given direction  $\mathbf{n}$  as

$$\frac{dI_\nu(\tau_\nu)}{d\tau_\nu} = S_\nu(\tau_\nu) - I_\nu(\tau_\nu). \quad (9)$$

This looks deceptively simple, but in principle has to be solved along every ray connecting points inside the model for each frequency, making it a six dimensional problem. Further contributing to the problem, the absorption coefficients depend on the microphysics, including the abundance and state of the gas, and the amount and nature of the dust. A popular approach is to tabulate the absorption as a function of density and temperature using a table specifically crafted for the problem at hand. An alternative is to compute it directly from the state of the system  $(\rho X_s, T)$ . To do this we need to know the chemical composition.

The *chemical evolution* is found by solving the rate equations individually in each cell of the simulation domain, assuming that no mixing or advection takes place. This is most conveniently formulated in terms of the number densities  $n_s$

$$\frac{dn_s}{dt} = F_s - D_s, \quad (10)$$

where the formation and destruction rates of a species are

$$F_s = \sum_{j \in \mathcal{F}_s} \left( k_j \prod_{r \in \mathcal{R}_j} n_r \right) \quad (11)$$

$$D_s = \sum_{j \in \mathcal{D}_s} \left( k_j \prod_{r \in \mathcal{R}_j} n_r \right), \quad (12)$$

$\mathcal{R}_j$  is the set of reactants for reaction  $j$  of the form  $r_1 + r_2 + \dots \rightarrow p_1 + p_2 + \dots$ , and the sums are over reactions where species  $s$  is formed ( $\mathcal{F}_s$ ) or destroyed ( $\mathcal{D}_s$ ). The rate coefficients  $k_j$  may depend on temperature and/or radiation field among other factors. In particular, for a photo-ionization or photo-dissociation reaction

$$k_j = 4\pi \int_{\nu_{\text{th}}}^{\infty} \frac{\sigma_{j,\nu} J_\nu}{h\nu} d\nu, \quad (13)$$

where  $\sigma_{j,\nu}$  is the frequency dependent photo cross section for reaction  $j$  and  $\nu_{\text{th}}$  is the energy threshold of the reaction. The removal of photons by these processes along with

the extinction coefficient of dust  $\alpha_v^d = \kappa_v^d f_d \rho$  gives a total extinction coefficient

$$\alpha_v = \alpha_v^d + \sum_{j \in \mathcal{P}} \sigma_{j,v} \prod_{r \in \mathcal{R}_j} n_r, \quad (14)$$

where  $\mathcal{P}$  is the set of all photo-chemical reactions,  $f_d$  is the dust to gas mass ratio and  $\kappa_v^d$  the dust opacity. In addition to evolving the chemistry, KROME also evolves the temperature inside each cell accounting for heating and cooling because of the radiation field or because of other processes such as e.g. exo/endothermic reactions. The temperature evolves according to

$$k_B \frac{dT}{dt} = (\gamma - 1) \frac{\Gamma_{\text{gas}} - \Lambda_{\text{gas}}}{n_{\text{gas}}}. \quad (15)$$

In this paper, our main concern is LAMPRAY, and we refer to Grassi et al. (2014, 2017) for an overview of the different cooling and heating processes that are included in KROME.

## 2.1 Radiative transfer

The radiative transfer equation is solved explicitly using long characteristics ray tracing. We discretise the intensity in frequency into a set of bins so  $I_{\text{bin}} = \int_{\nu_l(\text{bin})}^{\nu_u(\text{bin})} I_\nu d\nu$ , where  $\nu_u(\text{bin})$  and  $\nu_l(\text{bin})$  are the upper and lower frequency limits of the bin. In direction and space, we discretise along individual, global, rays with constant  $\mathbf{n}$  along which Eqn.(9) takes the form

$$\frac{dI_{\text{bin}}}{d\tau_{\text{bin}}} = S_{\text{bin}} - I_{\text{bin}}, \quad (16)$$

with source function  $S_{\text{bin}} = j_{*,\text{bin}}/\alpha_{\text{bin}}$  and optical depth element  $d\tau_{\text{bin}} = \alpha_{\text{bin}} dl$ , where  $l$  is the coordinate along the ray. In RAMSES the computational domain is covered by an adaptive mesh described with a fully threaded octree, and the rays are considered to go through leaf cells on all levels of the mesh, and each extend from one end of the simulation box to the other. Each ray is discretised into points that lie centred on the coordinate axis of fastest propagation within each leaf cell. The radiation field is separated into two components: a diffuse field and a point source field. In both cases, the discretisation in direction uses the HEALPIX scheme, which provides  $N_{\text{dir}} = 12N_{\text{side}}^2$  equal area directions at resolution  $N_{\text{side}}$ . In the diffuse field, for a given direction a set of rays are chosen such that at a given level of refinement the spacing between rays is equal, and such that every leaf cell is covered by at least one ray. In the point source field, every point source is simply intersected by one ray in each direction (see Sect. 3.1).

Several algorithms are provided for solving Eqn.(16) including Feautrier's method (Feautrier 1964; Hummer & Rybicki 1971) and the integral method of orders 0, 1 and 2. Since rays are not discretized at cell centres, interpolation is required of  $\alpha_{\text{bin}}$  and  $j_{*,\text{bin}}$  from cell centres to ray points, and of  $I_{\text{bin}}$  from the ray points to the cell centres (see Sect. 3.2). The intensity is finally averaged over  $N_{\text{dir}}$  directions

$$J_{\text{bin}} = \frac{1}{N_{\text{dir}}} \sum_{i=1}^{N_{\text{dir}}} I_{\text{bin},i}, \quad (17)$$

where we have exploited that by construction HEALPIX is an equal-area covering of the sphere.

The three components, radiative transfer, chemistry, and hydrodynamics are treated as independent within a time step, and are combined using operator splitting as follows. In a single timestep, first RAMSES evolves the hydrodynamics, then, the radiative transfer equation is solved with the updated densities and temperatures, and the chemical compositions inside the cells of the previous time step. Finally, the chemical network is evolved in each cell ignoring any  $PdV$  work using the new radiation field in each cell, giving a net heating / cooling term by which the total energy is changed. A new mean molecular weight and adiabatic index is also computed after the chemistry update. The timestep can be adaptively sub-cycled, proportional to the cell size. Since radiation propagation is treated as instantaneous, it connects regions with short time steps separated by regions with long time steps. Therefore, in the current version of LAMPRAY, the radiative transfer is solved globally at shortest timestep, updated in the leaf cells, and then propagated by averaging to the coarser levels.

## 2.2 Coupling to chemistry

We have implemented two methods that solve Eqn.(10), Eqn.(13) and Eqn.(14). The first method (Sect. 2.2.1) solves it for any set of photo-reactions and in connection with an arbitrary chemical network using the KROME package. It however requires a fairly restrictive time step if a correct propagation speed of fast ionization fronts is required, though it should be emphasized that it is photon-conserving and converges to the right radius once front has propagated. The second method (Sect. 2.2.2) is well suited for solving the propagation of fast moving ionization fronts, but only treats ionization of H, and was used for the StarBench benchmark (Bisbas et al. 2015).

### 2.2.1 Photo-chemistry with KROME

KROME (Grassi et al. 2014) is a framework that generates code from a description of a chemical network to efficiently solve its time-dependent evolution. It is able to compute photo-chemical rate coefficients based on frequency-binned mean intensities and on frequency-dependent photo cross-sections where available, and include the latter to evaluate the total frequency-binned opacity. Additionally, dust opacities may also be applied through the use of well-established lookup tables<sup>1</sup>.

Mellema et al. (2006) describes a very stable and accurate implicit method for solving the problem of ionization front propagation (see Sect. 2.2.2). Unfortunately we cannot easily use it with KROME, since it relies on formulating analytical expressions for the ionization fraction assuming a constant ionization rate coefficient during a single time step, and this is not possible for a general chemical network that may also include arbitrary non-photochemical reactions. We can, however, use the part of the method (originally from Abel et al. 1999) where the photo-chemical rate is set directly by the energy lost to extinction. It is equivalent to using the average intensity over a ray element optical depth

<sup>1</sup> <https://www.astro.princeton.edu/~draine/dust/dust.diel.html>

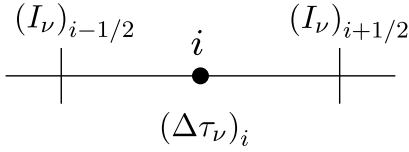


**Figure 1.** Discretisation along a ray.

$\Delta\tau_\nu$ , as shown in the following. Consider the discretisation of intensity and optical depth along a ray given in Fig. 1.

The ionization rate per frequency  $\Gamma_\nu$  at frequency  $\nu$  can be written

$$\Gamma_\nu = \sigma_\nu \frac{\langle I_\nu \rangle_i}{h\nu}, \quad (18)$$

with  $\sigma_\nu$  the cross section of the photo-chemical reaction in question, and  $\langle I_\nu \rangle_i$  the average intensity over ray element  $i$ . Within ray element  $i$ , the intensity, subject to extinction due to ionization events, is

$$I_\nu \left( \tau_\nu - (\tau_\nu)_{i-1/2} \right) = (I_\nu)_{i-1/2} e^{-\left( \tau_\nu - (\tau_\nu)_{i-1/2} \right)}, \quad (19)$$

so the average intensity over the optical depth element is

$$\langle I_\nu \rangle_i = \frac{(I_\nu)_{i-1/2}}{\Delta\tau_\nu} \int_0^{\Delta\tau_\nu} e^{-\tau_\nu} d\tau_\nu. \quad (20)$$

Given reactant number density  $n$  and ray element size  $\Delta l$ , the ray element optical depth is  $\Delta\tau_\nu = \sigma_\nu n \Delta l$ , so we have

$$\Gamma_\nu = \frac{(I_\nu)_{i-1/2}}{h\nu} \frac{1 - e^{-\Delta\tau_\nu}}{n\Delta l}. \quad (21)$$

The final expression corresponds to the one suggested by Abel et al. (1999), but for Cartesian geometry instead of spherical-polar. The expression also holds for more than one photo-reaction. In this case, the optical depth element is

$$\Delta\tau_\nu = \sum_{r \in \mathcal{P}} \sigma_{\nu,r} n_{s(r)} \Delta l, \quad (22)$$

where the sum is over all photo-reactions  $\mathcal{P} : s(r) + \gamma \rightarrow p(r)$ .  $s(r)$  is the reactant and  $p(r)$  is the product in reaction  $r$ . The per-volume photon absorption rate is then

$$\dot{n}_{\text{photon},\nu} = \sum_{r \in \mathcal{P}} \Gamma_{r,\nu} n_{s(r)} \quad (23)$$

$$= \frac{\sum_{r \in \mathcal{P}} \sigma_{\nu,r} n_{s(r)} \langle I_\nu \rangle_i}{h\nu} \quad (24)$$

$$= \frac{(I_\nu)_{i-1/2}}{h\nu} \frac{1 - e^{-\Delta\tau_\nu}}{\Delta l}, \quad (25)$$

where the cross sections are assumed to be zero below the threshold frequency. Using the average intensity thus allows us to interpolate frequency-binned opacities to the rays, and compute optical-depth averaged intensities there. This is crucial because the cost of interpolation and communication is decided by the choice of frequency binning, instead of being dictated by the often large number of species. Photons can also be lost to excitations of molecules that do not result in a reactive process, and to take into account such non-reactive cross-sections, these interactions can be included as dummy reactions in the chemical network. In this paper we ignore such extra processes, but we do include  $\text{H}_2$  and CO self-shielding (see Sect. 2.4), since their contribution is important in photo-dissociation regions (PDRs).

Assuming a constant source function over a ray element,

the average intensity over  $\Delta\tau$  is (dropping the explicit dependence on frequency  $\nu$ )

$$\langle I \rangle_i = \frac{1}{2} \left( I_{i-1/2}^+ + I_{i+1/2}^- - 2S_i \right) \frac{1 - e^{-\Delta\tau}}{\Delta\tau} + S_i. \quad (26)$$

We solve for the staggered intensity using a 0th order integral method, since this is stable even for unresolved ionization- and dissociation fronts. This works in the cases we consider, where the emission comes entirely from optical thin regions. To use the method for e.g. an emitting atmosphere, Eqn.(26) could still be used with a solver that is more accurate in thick regions, as long as the optical surface is resolved, since Eqn.(26) goes to the correct limit in the optically thick case.

When discretising in frequency, we need to define an appropriate frequency-mean opacity. In our example calculation of the structure of a photo-ionized region irradiated with the spectrum from Black (1987) (Sect. 4.4), we find that the most accurate method is to use the unweighted average, combined with careful placement of bin limits. To describe the ionization transitions of H and He as accurately as possible with few frequency bins, we compared the following three approaches to a reference solution using 100 logarithmically spaced bins. (1) Three bins above the ionization threshold of H (13.6 eV) that includes separations corresponding to the ionization threshold of H, He, and  $\text{He}^+$ , giving bin limits in eV: (13.6, 24.6, 54.4, 100). Photo cross sections are evaluated at the midpoint value in each bin. (2) The same frequency bins, but using the convolution of the cross section with the ISRF, i.e.

$$\langle \sigma \rangle_{\text{bin}} \equiv \frac{\langle \sigma J_{\text{Black}} \rangle_{\text{bin}}}{\langle J_{\text{Black}} \rangle_{\text{bin}}}. \quad (27)$$

(3) The cross section at the midpoint, but with an extra bin in the H and He regions to improve these two important transitions. The location of the extra bin limits were optimised to minimize the error in the optically thin rate coefficients, resulting in two additional bin limits of 16.50 and 31.43 eV. The approaches were compared to a uniform atomic hydrogen only medium with  $n_{\text{H}} = 100 \text{ cm}^{-3}$ . As seen in Fig. 2, approach (1) underestimates the rate coefficient of H ionization by an order of magnitude, while (2) by definition is correct in the optically thin region, but overestimates the opacity at larger optical depths, which should in reality fall as energy would preferentially be removed where the cross section is large. The extra bins in (3) however reduce the optically thin error to roughly 20%, and is even better at large optical depth, so this is the approach that is used in the following.

For some photo-reactions, a cross section is not available in the literature, but instead a parameterisation of the rate coefficient in terms of visual extinction ( $A_\nu$ ) and external field strength ( $G_0$ ) in units of the Draine Interstellar Radiation Field (ISRF) (Draine 1978) is available. In that case we parameterise the actual radiation field in terms of  $G_0$  and  $A_\nu$  as

$$J_{\text{bin}} = G_0 J_{\text{bin,Draine}} \exp(-\tau_{\text{bin}}), \quad (28)$$

where  $J_{\text{bin,Draine}}$  is the ISRF and we assume  $G_0$  to be constant. The optical depth can be expressed in terms of the dust column density, as well as the visual extinction as

$$\tau_{\text{bin}} = \kappa_{\text{bin,d}} f_{\text{d}} \frac{N_{\text{H}} m_{\text{p}}}{x_{\text{H}}} = \gamma_{\text{bin}} A_\nu. \quad (29)$$

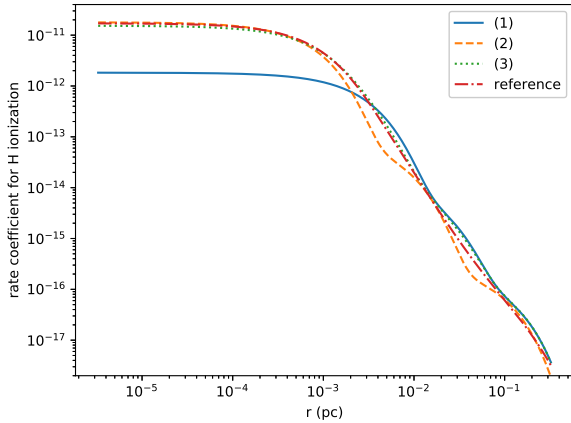


**Figure 2.** Test 4: Three approaches to frequency binning and average photo cross section. (1) Bin limits 13.6, 24.6, 54.4, 100 eV and unweighted average. (2) Same bin limits, but cross section according to Eqn.(27). (3) Direct average, with two extra bins with limits 16.50 and 31.43 eV. Reference has direct average and 200 logarithmic bins from 5 to 100 eV. The test is in a pure  $n_{\text{H}} = 100$  medium using the ISRF from Black.

Here,  $f_{\text{d}}$  is the dust mass fraction,  $N_{\text{H}}$  the column density of hydrogen,  $m_{\text{p}}$  the proton mass, and  $x_{\text{H}}$  the hydrogen mass fraction. Observationally, the visual extinction is approximately  $A_{\text{v}} = \frac{N_{\text{H}}}{1.8 \times 10^{21}}$  mag. Using this relation we have

$$\gamma_{\text{bin}} = 1.8 \times 10^{21} \kappa_{\text{bin,d}} f_{\text{d}} \frac{m_{\text{p}}}{x_{\text{H}}}. \quad (30)$$

Taking the logarithm of Eqn.(28) gives

$$\ln(J_{\text{bin}}) - \ln(J_{\text{bin,Draine}}) = \ln(G_0) - \gamma_{\text{bin}} A_{\text{v}} \quad (31)$$

To determine  $\ln(G_0)$  and  $A_{\text{v}}$  needed for the reaction rates we make a linear fit by least squares to the above equation over the relevant frequency bins with a photon energy between 5 and 13.6 eV.

### 2.2.2 Hydrogen ionization with c2ray

In an explicit method, the evolution of radiatively driven ionization fronts can require a very small time step and cell size to resolve correctly the ionization front, and obtain the right propagation speed. C2RAY (Mellema et al. 2006) is an explicitly photon-conserving and causally implicit photo-ionization method that takes the ionization rate to be explicitly set by the flux attenuation, and uses of an analytical expression for the time evolution to compute the time-step averaged ionization fraction. This makes it a robust method that converges with a more or less arbitrary time step and spatial resolution. It is implemented here for the ionization of pure hydrogen, by interpolating, not opacity and emissivity, but the abundance of H and  $\text{H}^+$  to the rays, solving along the rays as described in Mellema et al. (2006), and interpolating back the resulting ionization and recombination rate to the cell centres, where they are applied. The entire procedure is repeated until the neutral fraction converges. While robust and elegant, this approach is very specific to the case of hydrogen ionization.

### 2.3 Interstellar radiation field as diffuse emission

In earlier 3D dynamical models of PDRs, the external radiation field has been simulated as an ISRF, attenuated through a column density measured from the edge of the simulation box (e.g. Nelson & Langer 1997; Glover & Mac Low 2007). While this works well when modelling an isolated cloud that stays more or less centred in the simulated box, when simulating turbulent clouds in a periodic box, this choice introduces an artificial asymmetry by predominantly irradiating regions closer to the boundaries. To respect the periodicity of the box we instead choose to simulate the external field as an artificial emission in the hot, dilute inter-cloud medium. This is somewhat similar to the proposal by Walch et al. (2015), where each point is irradiated from a constant distance, but does not introduce such a distance cut-off.

For the emission, we use the spectral energy distribution due to Black (1987). The criteria for which cells will contain a source is adhoc in nature. We have chosen to use a chemical cutoff; we place an emission  $j_{*,\text{c},\nu} = j_{*,0,\nu} V \frac{w_{\text{c}}}{w_{\text{tot}}}$  in sufficiently ionized cells according to a weighting function

$$w_{\text{c}} = \begin{cases} \rho^2 & n_{\text{H}} \leq n_{\text{th}} \\ 0 & n_{\text{H}} > n_{\text{th}}, \end{cases} \quad (32)$$

where  $n_{\text{th}}$  is a threshold neutral number density,  $V$  is entire the simulation volume, and  $w_{\text{tot}} = \sum_{\text{c}} \Delta V_{\text{c}} w_{\text{c}}$  is a normalising factor, with  $\Delta V_{\text{c}}$  the cell volume. By weighting with  $\rho^2$  we balance the recombination rate equally well in low and high density regions in a simulation, and do not artificially drive the expansion or collapse of HII regions. The normalisation corresponds to assuming a constant amount of photons to be created per unit time, and therefore help in avoiding feedback loops. In principle this could be refined to depend on e.g. the instantaneous star formation rate, but we find the constant to be a good compromise given that a diffuse radiation field really represent the radiation *external* to the region coming from the larger galactic environment, and not a self-consistently created radiation field generated by the stellar feedback inside the box.

### 2.4 Self-shielding of $\text{H}_2$ and CO

The self-shielding of  $\text{H}_2$  and CO needs to be treated carefully to get qualitatively correct results for the two most abundant molecules in the ISM. Since this requires that one follows in detail their excited states and the associated frequencies (Visser et al. 2009), this is not currently achievable in 3D radiation hydrodynamics calculations. We follow a common approach (Glover & Mac Low 2007; Safranek-Shrader et al. 2017) where a prescription for self-shielding as a function of column density and temperature is used to find the dissociation rate. The prescription used here is from Richings et al. (2014b), and is derived from detailed calculations with the 1D photochemistry code CLOUDY (Ferland et al. 1998, 2013). In it, the dissociation rates in optically thick regions are found as (Richings et al. 2014b, Eqn. 3.18 and 3.19)

$$\Gamma_{\text{H}_2,\text{thick}} = \Gamma_{\text{H}_2,\text{thin}} f_{\text{s}}^{\text{H}_2} \quad (33)$$

and

$$\Gamma_{\text{CO},\text{thick}} = \Gamma_{\text{H}_2,\text{thin}} f_{\text{s}}^{\text{CO}} \quad (34)$$

where  $\Gamma_{x,\text{thin}}$  is the dissociation rate of species  $x$  given an unattenuated ISRF, and  $f_s^x$  is a total shielding factor for that species, given by

$$f_s^{\text{H}_2} = S_{\text{d}}^{\text{H}_2} (N_{\text{dust}}) S_{\text{self}}^{\text{H}_2} (N_{\text{H}_2}) \quad (35)$$

and

$$f_s^{\text{CO}} = S_{\text{d}}^{\text{CO}} (N_{\text{dust}}) S_{\text{self,CO}}^{\text{CO}} (N_{\text{CO}}, N_{\text{H}_2}), \quad (36)$$

where  $N_x$  is column density of dust,  $\text{H}_2$ , and CO respectively. The dust column density is proportional to the total Hydrogen column density and the dust to gas mass fraction. For the individual shielding factors for dust  $S_{\text{d}}^x$  and self-shielding  $S_{\text{self}}^x$  we refer to Richings et al. (2014b). As noted in Glover & Mac Low (2007), turbulent Doppler-shift of lines is not taken into account and this approximation will tend to overestimate self-shielding. Another reservation is that the prescription is based on the equilibrium solutions to a static dissociation front, while we intent to use it in the non-equilibrium, dynamical environment of a turbulent ISM.

Our approach is similar to how Safranek-Shrader et al. (2017) post-process simulations by ray-tracing the galactic disc using a uniform emission in the galactic plane that represents the stellar radiation field. They replace the usual solution to the 1D radiative transfer equation by the following double sum (their Eqn. 23, slightly relabelled here)

$$I_{\text{bin}}(n) = \sum_{i=0}^{n-1} \Delta l_i j_{*,\text{bin},i} S_{\text{bin}} \left( \sum_{j=i}^n \mathbf{n}_{\text{spec},j} \Delta l_j \right), \quad (37)$$

where  $I_{\text{bin}}(n)$  is the intensity in the frequency range ‘‘bin’’ in cell  $n$ ,  $\Delta l_i$  is the path length of the ray through cell  $i$ ,  $j_{*,\text{bin},i}$  is the emissivity in cell  $i$  in the frequency bin,  $S_{\text{bin}}$  is the shielding function and  $\mathbf{n}_{\text{spec},i}$  is a vector of the number densities of the relevant species in cell  $i$ . The double sum must be computed in every cell. If the sum over column depth is performed as a series of running sums, one for each source, this method has complexity  $\mathcal{O}(N^2)$  in the number of points along the ray. Since in our case the sources are by definition placed in optically thin regions, we can to a good approximation gather a set of neighbouring sources into a single source. Computing only running sums from cells with a source, the complexity reduces to  $\mathcal{O}(NN_r)$  where  $N_r$  is the number of emitting regions along the ray, which is usually low in realistic situations. In this method, it is  $n_{\text{H}_2}$ ,  $n_{\text{CO}}$ ,  $n_{\text{H}_{\text{tot}}}$ ,  $T_{\text{gas}}$  and  $j_{*,c} = \int_0^\infty j_{*,c,v} dv$  that are interpolated from cell centres to rays. The resulting frequency-integrated solid-angle mean intensity  $J^{\text{dis}}$  is interpolated back to cell centres, and the dissociation rate per molecule is found as

$$\Gamma_{\text{dis,thick}} = \frac{J^{\text{dis}}}{\int_0^\infty J_{\text{v}}^{\text{Black}} dv} \Gamma_{\text{dis,thin}} \quad (38)$$

where  $\Gamma_{\text{dis,thin}}$  is the optically thin dissociation rate given the Black ISRF, with values  $\Gamma_{\text{H}_2,\text{thin}} = 7.5 \times 10^{-11} \text{ s}^{-1}$  (Richings et al. 2014a), and  $\Gamma_{\text{CO,thin}} = 2.6 \times 10^{-10} \text{ s}^{-1}$  (Visser et al. 2009).

## 2.5 Thermal balance of dust grains

Grain surface chemistry depends on the temperature of the dust grains, and is used in our chemical network for calcu-

lating the  $\text{H}_2$  formation rate, and the freeze-out and evaporation of  $\text{H}_2\text{O}$  and CO ices. The kinetic cooling or heating of the gas also depends on the temperature differential between dust and gas. In Grassi et al. (2017) we demonstrated how these functions can be tabulated given a radiation environment. The core assumption is that the time-scale for dust grains to be in thermal equilibrium is shorter than any relevant dynamical timescales, which is usually the case. Then Kirchhoff’s law holds. The radiation absorbed ( $\Gamma_{\text{abs}}$ ) by the dust grain is equal to the emitted radiation ( $\Gamma_{\text{em}}$ ) plus the kinetic cooling due to interaction with gas molecules ( $\Lambda_{\text{gas}}^{\text{col}}$ )

$$\Gamma_{\text{abs}} = \Gamma_{\text{em}} + \Lambda_{\text{gas}}^{\text{col}}. \quad (39)$$

Integrating over a distribution of dust grains embedded in a gas in the *optically thin regime* this becomes (Tielens 2010; Grassi et al. 2017)

$$\begin{aligned} \Gamma_{\text{abs}} &= \int_0^\infty dE \int da \pi a^2 \varphi(a) \frac{Q_{\text{abs}}(a, E) J(E)}{h} \\ \Gamma_{\text{em}} &= \int_0^\infty dE \int da \pi a^2 \varphi(a) \frac{Q_{\text{abs}}(a, E) B[E, T_d(a)]}{h} \end{aligned} \quad (40)$$

$$\Lambda_{\text{gas}}^{\text{col}} = 2f v_{\text{gas}} n_{\text{gas}} \int da \pi a^2 \varphi(a) k_B [T - T_d(a)],$$

where  $\pi a^2$  is the geometrical cross section of a dust grain with radius  $a$ , and  $\varphi(a)$  is the distribution function, e.g. the number density of grains per grain size.  $Q_{\text{abs}}(a, E)$  is the absorption coefficient of the grains,  $B[E, T_d(a)]$  is the black-body spectral radiance with dust grain temperature  $T_d(a)$ ,  $J(E)$  is the mean intensity at energy  $E$ , and  $v_{\text{gas}}$  is the thermal gas speed. The factor  $f$  accounts for gas-grain collisions with atoms and molecules other than atomic hydrogen, and it depends not only on the gas composition, but also on the grain charge distribution (see Draine 2009 sect. 24.1.2). We will assume it to be  $f = 0.5$ , which corresponds to a cold partially molecular gas. In this paper, we model the radiation as being constant inside each bin:  $J(E) = J_i$ , if  $E_{\text{min},i} < E < E_{\text{max},i}$ . Then the radiation absorbed by the dust grains can be calculated as

$$\Gamma_{\text{abs}} = \sum_{i \in \text{bins}} J_i \tilde{\Gamma}_{\text{abs},i}, \quad (41)$$

where

$$\tilde{\Gamma}_{\text{abs},i} = \int_{E_{\text{min},i}}^{E_{\text{max},i}} dE \int da \pi a^2 \varphi(a) \frac{Q_{\text{abs}}(a, E)}{h}. \quad (42)$$

To implement this in actual code we precalculate  $\tilde{\Gamma}_{\text{abs},i}$ , and then construct log-spaced 3D tables for the  $\text{H}_2$  formation rate, surface averaged dust temperature  $T_{\text{d}}$ , and gas cooling  $\Lambda_{\text{gas}}^{\text{col}}$  as a function of  $\Gamma_{\text{abs}}$ ,  $T$ , and  $n_{\text{gas}}$ , following the methodology of Grassi et al. (2017). The formalism allow the  $\text{H}_2$  formation rate to be tabulated for the specific dust distribution with individual dust temperatures for each species and size bins (we used 20 logarithmically spaced size bins for the distribution with a mixture of silicate and carbonaceous grains). But to calculate the absorption and desorption of  $\text{H}_2\text{O}$  and CO ices we need a single averaged dust temperature in the network. For that we chose to use a number density weighted temperature

$$T_{\text{d}} = \frac{\int da \varphi(a) T_{\text{d}}(a)}{\int da \varphi(a)}. \quad (43)$$

Notice that to be fully consistent one would need to calculate the ice to gas rates based on the temperatures of the individual bins, which could be done by introducing additional lookup tables. Alternative definitions, such as a surface averaged or emission averaged temperatures could be used, though this does only change the dust temperature with up to a few degrees, and therefore only lead to very minor changes in the results. We also note that in very dense and dusty regions the assumption that the thermal radiation is optical thin may not hold. This can be dealt with either by a suitable parameterisation of the self-absorption and escape fraction inside a single cell (Grassi et al. 2017) or explicitly through the introduction of infrared frequency bins and an account of scattered light (Rosdahl & Teyssier 2015).

Ideally, each set of tables should be made for the specific environment, and we caution that the 3D tables currently available through KROME are made for the tests in this paper. In all our tests we have used a MRN power law grain size distribution with  $\varphi(a) \propto a^{-3.5}$  (Mathis et al. 1977), and a size range from  $5 \times 10^{-7}$  cm to  $2.5 \times 10^{-5}$  cm. We use a mixture of carbonaceous and silicate grains in the ratio 9:1 (same as the ratio of the key elements C and Si at Solar metallicity) and assume a solar dust to gas mass ratio of 0.00934.

## 2.6 Adsorption and desorption of CO and H<sub>2</sub>O ices

For the adsorption reaction rate coefficients per gas molecule for species  $s$ ,  $k_{\text{ads},s}$ , we follow Hollenbach & McKee (1979); Hocuk & Cazaux (2015).

$$k_{\text{ads},s} = \sigma_s v_{\text{gas},s} n_{\text{dust}}, \quad (44)$$

where  $\sigma_s$  is the cross section,  $v_{\text{gas},s}$  is the thermal velocity of species  $s$ , and  $n_{\text{dust}}$  is the number density of dust grains. The cross section is given as the product of a sticking rate  $S(T, T_d)$  and the surface area of the dust. Assume an MNR dust distribution with a power law exponent  $p = -3.5$ , minimum and maximum grain sizes  $a_{\text{min}}$  and  $a_{\text{max}}$ , then we have

$$\sigma_s n_{\text{dust}} = S(T, T_d) \frac{f_d \rho_g}{4/3 \rho_m} \frac{p+4}{p+3} \times \frac{a_{\text{max}}^{p+3} - a_{\text{min}}^{p+3}}{a_{\text{max}}^{p+4} - a_{\text{min}}^{p+4}}, \quad (45)$$

where  $\rho_m = 3 \text{ g cm}^{-3}$  is the material density of the dust, and we parametrize the sticking coefficient as

$$S(T, T_d) = \left[ 1 + 0.04 \sqrt{T + T_d} + 0.002 T + 8 \times 10^{-6} T^2 \right]^{-1}. \quad (46)$$

For the desorption we include three contributions: thermal, non-thermal, and cosmic ray desorption. The total rate is then

$$k_{\text{des},s} = k_{\text{th-des},s} + k_{\text{ph-des},s} + k_{\text{cr-des},s}. \quad (47)$$

We assume that the thermal desorption of species  $s$  follows the Wigner-Polyany mechanism

$$k_{\text{th-des},s}(T_d) = \nu_0 \exp\left(-\frac{E_s}{k_b T_d}\right), \quad (48)$$

where  $\nu_0 = 10^{12} \text{ s}^{-1}$  and  $E_s$  is the binding energy of the ice. We include non-thermal desorption due to radiation as (Hollenbach et al. 2009; Hocuk & Cazaux 2015)

$$k_{\text{ph-des},s} = G_0 F_0 a_p^2 Y_s \exp(-1.8 A_v), \quad (49)$$

where  $F_0 = 10^8 \text{ cm}^{-2} \text{ s}^{-1}$  is the number of photodesorbing photons at  $G_0 = 1$  and  $A_v = 0$ ,  $a_p = 3 \times 10^{-8} \text{ cm}$ ,  $Y_{\text{CO}} = 10^{-3}$ , and  $Y_{\text{H}_2\text{O}} = 2 \times 10^{-3}$ . The cosmic-ray photodesorption rate (Hasegawa & Herbst 1993; Reboussin et al. 2014) is

$$k_{\text{cr-des},s} = f(70 \text{ K}) k_{\text{th-des},s}(70 \text{ K}), \quad (50)$$

where the fraction of time spent by the grain at 70 K is  $f(70 \text{ K}) = 3.16 \times 10^{-19} \zeta / \zeta_0$ ,  $\zeta_0 = 1.3 \times 10^{-17} \text{ s}^{-1}$ , and  $\zeta$  is the cosmic ray ionization rate. Although for the adsorption we used a size distribution in accordance with our general model for the dust grains, in this expression assumes dust grains to be of size  $a = 0.1 \mu\text{m}$  (Leger et al. 1985) introducing a small inconsistency.

Including ice evaporation in the chemical network increases the stiffness of the differential equations, in particular when the dust temperature is time-dependent. This is because of the exponential dependence of the ice evaporation on the dust temperature. If the equations are reformulated in terms of the total number density of a species,  $n_{\text{tot}} = n_{\text{gas}} + n_{\text{ice}}$ , and the gas phase number density,  $n_{\text{gas}}$ , the stiffness is significantly reduced (W-F. Thi, private communication). For the ices we solve

$$\dot{n}_{\text{tot}} = \dot{n}_{\text{gas}} + \dot{n}_{\text{ice}} \equiv \dot{n}_{\text{chem}} \quad (51)$$

$$\dot{n}_{\text{gas}} = \dot{n}_{\text{chem}} - (k_{\text{des}} + k_{\text{ads}}) n_{\text{gas}} + k_{\text{des}} n_{\text{tot}}, \quad (52)$$

where  $\dot{n}_{\text{chem}}$  is the change in the species due to gas-phase chemical reactions, and  $k_{\text{des}}$  and  $k_{\text{ads}}$  are the evaporation and freeze-out rate coefficients. Apart from thermal evaporation, in the case of CO we also include non-thermal evaporation by UV photons that can dominate the evaporation rate in low-density regions with infrequent collisions, where dust cools efficiently and keeps cool even when the gas is hot.

## 3 IMPLEMENTATION

The hybrid-characteristics method described for point-sources in Rijkhorst et al. (2006) and diffuse radiation in Buntmeyer et al. (2016) works well on patch-based hierarchical adaptive meshes. RAMSES, however, has a cell-based octree, based on the fully threaded tree by Khokhlov (1998), and the ‘‘patches’’ that would be connected by short-characteristics rays, would consist of only  $2 \times 2 \times 2$  cells. In this structure, neighbour cells are found by first accessing the coarser parent cell of an oct, then finding the neighbour, and then looking for refined cells in the neighbour to the parent oct. This makes repeated access to neighbour cells required by the method fairly expensive, and implies that a short-characteristics-based method would not perform well on a fully threaded tree.

Our solution is instead to use long characteristics rays that cover the entire domain. These are organized in a sense as short characteristics rays that line up and connect the computational domain from one end to the other, so repeated calculation of optical depth through similar paths is avoided (see Fig. 3). Quantities required by radiative transfer are interpolated to the points along the long rays. This happens in the domain decomposition used for the hydrodynamics, which in RAMSES means that an MPI rank owns cells along one or more slices of a Hilbert space-filling curve in physical space. A single long ray therefore typically crosses a number of MPI ranks. To compute efficiently the solution



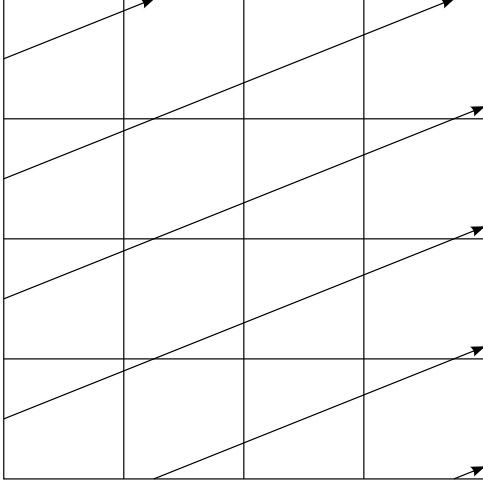


**Figure 3.** Long characteristics rays as lined-up short characteristics. Points along the rays are connected to cell centres by interpolation.

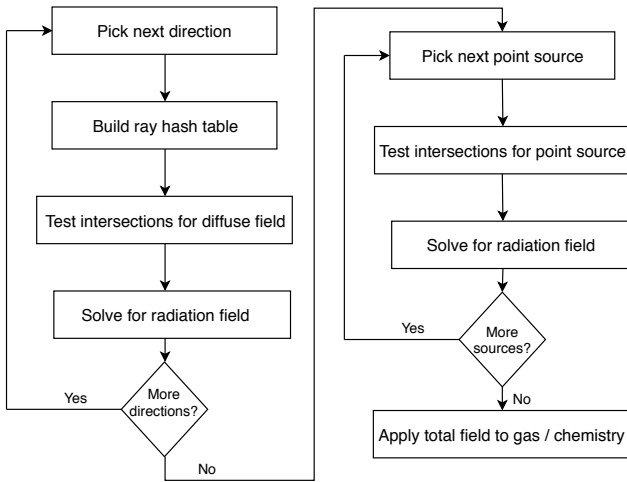


**Figure 4.** Outline of LAMPARRAY in flow chart form. See the text for an explanation of the steps.

to the radiative transfer along rays we change the domain decomposition for the ray points, such that, for the purpose of radiative transfer, all points along a given ray belongs to the same MPI rank, and all ranks own a similar number of ray points. In the new *ray domain* decomposition, the solution to the one-dimensional radiative transfer problem can be obtained efficiently, with near-perfect vectorisation, cache usage and load balancing. Once the solution is known at the ray points, it is communicated back to the cell domain in a similar but reverse exchange of information between the ray and cell decomposition, and interpolated to the cell centres (see Fig. 5).

Although the communication step is extensive, the cost is not as high as one might expect, and turn out to be worth the gains that comes from the decoupling it provides.

This underlying idea was first presented in the masters thesis of Frostholm (2014). In this work most parts of the

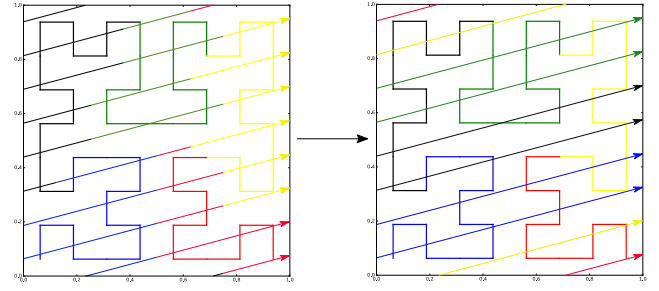


**Figure 5.** The domain decomposition is changed. Colours denote MPI rank ownership.

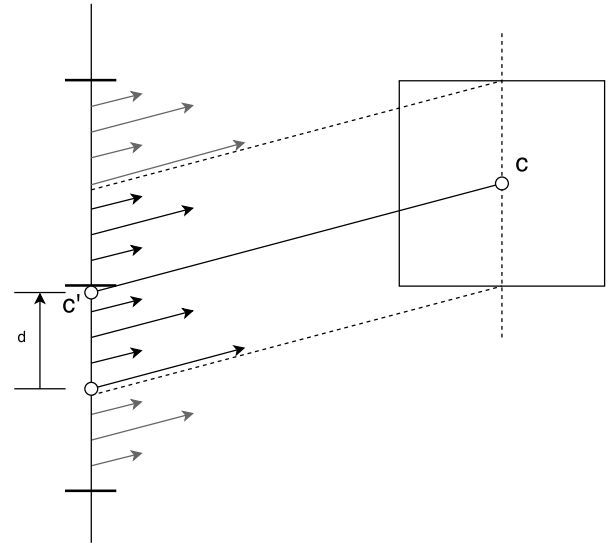


**Figure 6.** Given a ray direction,  $C'$  is the projection of cell centre  $C$  along this direction to the ray plane (solid vertical line), and is located a distance  $d$  from the nearest ray origin at that level of refinement on the ray plane (bottom open circle). Rays at lower level of refinement that intersect the cell originate at most half a cell width away from  $C'$ .

implementation have been completely replaced, including methods for ray tracing, interpolation, and handling of periodic boundaries. The photo-chemistry solver is completely new.

The rest of this section will explain how rays are laid out and traced to properly cover the AMR grid, how the interpolation is done between cells and rays, and finally how the MPI parallel nature of RAMSES is handled when tracing rays and by changing domain decomposition. The overall method is sketched in Fig. 4.

### 3.1 Ray Tracing

The radiation field is split into two components: A diffuse field for extended sources of emission, and a point source field. The diffuse field is discretised in solid angle into a set of equal-solid-angle directions using the HEALPIX scheme (Górski et al. 2005), and for each direction into a set of

parallel rays that cover the computational domain end-to-end. For the diffuse field, the radiative transfer problem is solved one direction at a time to limit memory usage.

In order to cover leaf cells at all levels of refinement, rays are chosen as follows. Consider a single ray direction  $\mathbf{r}$ . Let  $a_z$  be the coordinate axis where  $\mathbf{r}$  has its largest component. We will refer to the plane defined by  $a_z = 0$  as the ray plane. At a given refinement level  $\ell$  we define a Cartesian grid on the ray plane, with cell centres  $c_{i,j}^{\text{rp}} = 0.5^\ell L(i + 0.5)$  where  $L$  is the box length. At each level, for all  $(i, j)$ , we choose rays with origin  $c_{i,j}^{\text{rp}}$ . We should however only include rays that intersects leaf cells at level  $\ell$ . Rays at level  $\ell$  that are surrounded in the ray plane by rays originating from all four ray plane child cells at level  $\ell + 1$  can however be excluded. And finally we should honor intersections of rays at level  $\ell$  with leaf cells at lower levels.

The ray plane grids occupied by rays for each level are sparse structures. We choose to represent these as a single hash table, with the triple  $(\ell, i, j)$  as hash key. The table is constructed as follows. For each leaf cell, we project the cell centre along the ray direction on to the ray plane and round the projected coordinate to get integer indices  $i$  and  $j$ . The ray plane cell is marked as containing a ray by placing the arbitrary value 1 under the key  $(\ell, i, j)$ . Exclusion of surrounded rays is deferred to when ray points are constructed. Once the table has been built, the keys are sorted and the table values are replaced by unique ray ids that enumerate the keys.

A point along the ray is defined as the structure that contains the ray id, the id of the intersected cell, the distance along the ray from the ray plane to the back face of the intersected cell, and the values of radiative transfer variables at the ray point. Points along rays are constructed as follows. 1) For each leaf cell we find  $i$  and  $j$  by projecting on the ray plane as before. By construction, the corresponding ray exists. 2) The ray plane cell has four children with keys  $(\ell + 1, 2i, 2j)$ ,  $(\ell + 1, 2i + 1, 2j)$ ,  $(\ell + 1, 2i, 2j + 1)$  and  $(\ell + 1, 2i + 1, 2j + 1)$ . These are looked up to see if they are occupied by rays. If they all are, the ray at level  $\ell$  is excluded, so nothing is done. Otherwise a ray point is created. 3) In any case, rays on level  $\ell + 1$  may also intersect our leaf cell. These may not be the same as the four child rays. If the projected cell centre is more than a quarter cell size above (below) the ray plane cell centre in  $x$ , the intersecting rays at level  $\ell + 1$  will have indices  $2i + 1$  and  $2i + 2$  ( $2i - 1$  and  $2i$ ), and similarly in  $y$ . For those rays that exist, ray points are constructed recursively from point 2.

There is a subtlety in picking out the intersecting rays at the following level at every recursive step. Going from level  $\ell$  to  $\ell + 1$  we can proceed as just described. Lets label by  $d$  the distance from the ray plane cell centre to the projected cell centre in units of the cell size at level  $\ell$ , and the vector of indices at level  $\ell + 1$  by  $\mathbf{i}_{\ell+1} = (2i, 2i + 1) + q_{\ell+1}$ , where

$$q_{\ell+1} = \begin{cases} 1 & d > \frac{1}{4} \\ 0 & \frac{1}{4} \geq d > 0 \\ 0 & 0 \geq d > -\frac{1}{4} \\ -1 & -\frac{1}{4} \geq d \end{cases} \quad (53)$$

Going from level  $\ell + 1$  to  $\ell + 2$  we have  $\mathbf{i}_{\ell+2} = (4i, 4i + 1, 4i + 2, 4i + 3) + q_{\ell+1} + q_{\ell+2}$ . Another way to say this is that at level  $\ell + 2$  we have for each parent index  $i^P \in \mathbf{i}_{\ell+1}$  two child

indices  $\mathbf{i}_{\ell+2}^c = (2i^P, 2i^P + 1) + q_{\ell+2}$ . Here  $q_{\ell+2}$  is determined by the following eight cases (see Fig. 6).

$$q_{\ell+2} = \begin{cases} 0 & d > \frac{3}{8} \\ -1 & \frac{3}{8} \geq d > \frac{1}{4} \\ 1 & \frac{1}{4} \geq d > \frac{1}{8} \\ 0 & \frac{1}{8} \geq d > 0 \\ 0 & 0 \geq d > -\frac{1}{8} \\ -1 & -\frac{1}{8} \geq d > -\frac{1}{4} \\ 1 & -\frac{1}{4} \geq d > -\frac{3}{8} \\ 0 & -\frac{3}{8} \geq d \end{cases} \quad (54)$$

At this point a pattern emerges. If we were to continue to level  $\ell + 3$ , we would get the offsets  $0, -1, 1, 0$  repeated 4 times, at level  $\ell + 4$  repeated 8 times etc. So if we define  $\mathbf{Q} = (0, -1, 1, 0)$  and at child level  $\ell + L$  we define  $d'_L = \lceil (\frac{1}{2})^L d - 1 \rceil \bmod 4$ , we can write  $q_L = \mathbf{Q}(d'_L)$ .

For point sources, radiative transfer is solved one source at a time. The point source field is covered by the rays given by vectors at a given HEALPIX resolution. Using the HEALPIX library, tracing point source rays is simple. Given a cell located at  $\mathbf{c}$  and a point source at  $\mathbf{p}$ , we translate  $\mathbf{c} \rightarrow \mathbf{c}' = \mathbf{c} - \mathbf{p}$ , and use the `query_polygon` HEALPIX routine to find the HEALPIX vectors that intersect the square defined by the intersection between the plane perpendicular to the largest component of  $\mathbf{c}'$  and the cell outline around  $\mathbf{c}'$ . The ray segment centres are chosen as the intersection between this plane and the HEALPIX vectors. We use the HEALPIX nested pixel index as unique ray id for matching up ray points and load balancing rays.

### 3.2 Interpolation

When interpolating from cells to rays, we are interpolating in three dimensions from a uniform grid so we can get a second-order accurate, conservative interpolation with triangular-shaped cloud (TSC) interpolation. Where support points are missing, they are reconstructed from the eight surrounding parent cells using cell-in-cloud (CIC) interpolation.

When the radiative transfer problem has been solved along the rays, and we need to interpolate back from rays to cells, we interpolate from a less structured set of points. As interpolation errors can be hard to avoid at refinement boundaries, we made a few preliminary tests in two dimensions. The setup is as follows. We have a 2D simulation box  $16 \times 16$  cells large with the central  $8 \times 8$  cells each split into four. The physical size is  $1 \times 1$  in arbitrary units. The extinction coefficient is uniform at  $\alpha = 1$  and a radiation field with intensity  $I_0 = 1$  is applied at one face, with a single ray direction with angle  $\theta$  with the  $x$ -axis. We use two ray coverage strategies: R1) The fine region is covered by rays as described above, so they extend to the coarse region and cover the coarse cells twice as densely. R2) The same as R1, but with dense coverage extended by one cell in each direction. Coarse rays are considered to cover a width of  $\Delta a = \sin(\theta)\Delta x$  with  $\Delta x$  the coarse cell size, and fine rays cover half that width. The quantity that is interpolated is  $Q = I\Delta a\Delta l$  where  $\Delta l$  is the length of the ray segment through the cell. After interpolation, an intensity is recovered by dividing by the cell area  $I = Q/(\Delta x)^2$ .

Interpolation on refinement boundaries is treated as fol-

lows. A ray point in a fine boundary cell gets interpolated to either fine cell centres, or – where those points are in a coarse cell – to a virtual fine cell in the coarse cell. From here it is further interpolated by one of the mentioned conservative methods to the surrounding coarse cell centres. The highest order method for deposition from virtual fine cells that has support is CIC. A ray point in a coarse boundary cell is interpolated to a fine cell by first interpolating to the coarse parent cell, and then adding the contribution to the fine cell.

For each interpolation method, we try out two cases: Firstly interpolation in two dimensions on our 2D grid (corresponding to 3D if implemented in RAMSES). Secondly interpolation in one dimension, namely along the line perpendicular to the main propagation axis (corresponding to 2D in the plane perpendicular to the main propagation axis in RAMSES).

In the test, all combinations of the described methods conserve energy to machine precision as expected, but none give a maximal interpolation error below 30%. We therefore also try to relax the conservation requirement and use an irregular mesh interpolation method. This consists of interpolating as described above, but dividing the result by the total weight. Because of the normalisation, the intensity is interpolated directly without weighting by volume. With the irregular method using TSC, with NGP used for fine-coarse virtual grid propagation, the R1 coverage strategy, and the interpolation done in 1D, the maximal error reduces to just below 1% with a relative deficit of total energy of less than  $5 \times 10^{-7}$ . Both maximal error and energy conservation error depend on the field gradient, and grow roughly linearly with  $\alpha$ . Selected results are summarised in Tab. 1. Ray discretisation and error for tests I3 and I8 are shown in Fig. 7.

Based on these tests, we choose to use the unstructured variant of TSC interpolation in the plane perpendicular to the main ray direction and the R1 coverage strategy.

### 3.3 Parallelisation

The RAMSES grid is distributed over different MPI ranks, and when constructing the hash table of rays in Sect. 3.1, we need to merge them before constructing ray points. This is done by extracting an array of the keys and values on each rank, gathering them on a single master rank, inserting them into the master rank’s table, and then scattering keys and values to all ranks.

When ray points have been constructed, and radiation variables interpolated to them, they represent ray intersections with the leaf cells present at a given rank, and they have the same cell-centric domain decomposition as RAMSES’ grid. We now change to a ray-centric domain decomposition. The load is balanced between ranks by dividing rays into equally sized chunks according to ray id, and sending ray points to the ranks that correspond to the ray they belong to.

Before sending data from cell- to ray domain, the ray points, initially gathered in the order they were created, are sorted in memory according to ray id, so continuous blocks can be sent. The switch consists of a large communication step, where a number of ray points (typically on the order of the number of leaf cells on one rank) are exchanged, and all domains potentially could need to communicate with each other. Once received in the ray domain, the ray points must

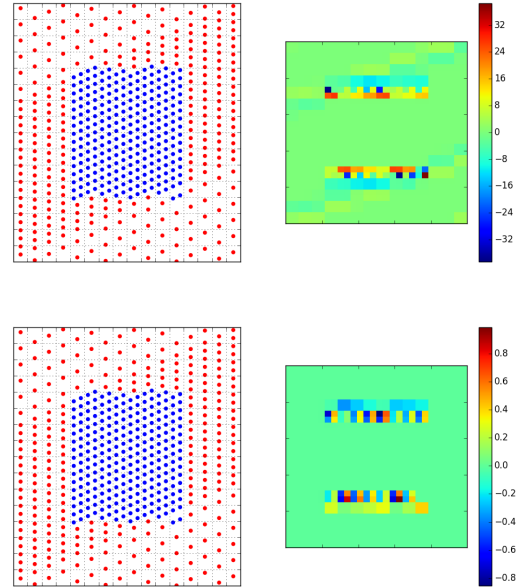


**Figure 7.** Ray discretisation (left) and relative interpolation errors in percent (right) for the tests of interpolation method labelled I3 (top) and I8 (bottom).

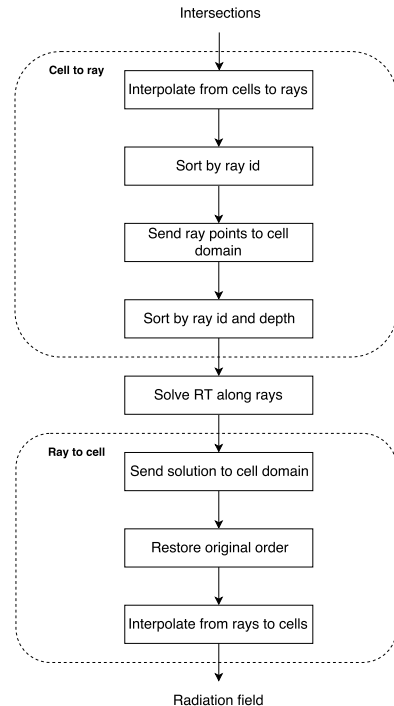


**Figure 8.** Flow chart indicating the steps involved in changing the domain decomposition from cell-based to ray-based and back.

Test	Interpolation	Reconstruction on boundaries	Ray coverage	Maximum relative error	Relative conservation error
I1	TSC (2D)	NGP	R1	34.99 %	$1.8 \times 10^{-14}\%$
I2	TSC (2D)	CIC	R1	40.35 %	$5.4 \times 10^{-14}\%$
I3	TSC (1D)	NGP	R1	38.57 %	$1.8 \times 10^{-14}\%$
I4	TSC (1D)	NGP	R2	35.50%	$5.4 \times 10^{-14}\%$
I5	CIC (1D)	NGP	R1	44.61%	$7.2 \times 10^{-14}\%$
I6	QSP (2D)	NGP	R1	63.74%	$1.8 \times 10^{-14}\%$
I7	TSC unstructured (2D)	NGP	R1	1.76%	$1.2 \times 10^{-2}\%$
I8	TSC unstructured (1D)	NGP	R1	0.99%	$4.2 \times 10^{-5}\%$

**Table 1.** Summary of tests of interpolation method and ray coverage strategy. NGP, CIC, TSC, and QSP are B-spline interpolation of order zero, to four, respectively.

be sorted into the order in which they will be traversed when solving the radiative transfer equation along rays according to ray id and distance along the ray. Sorting is accomplished with the Quicksort algorithm. The resulting order of the two sorting operations is saved and reused to get the solution returned to the cell domain back into the original order.

For some applications, the communication step can become too large to be handled correctly by a variant of an MPI\_ALLTOALL operation, and is therefore split into a series of smaller communications. The domain decomposition switch is summarised in Fig. 8.

### 3.4 Scaling considerations

As described, each rank must have access to a global hash table of all rays. Inevitably, for a large enough number of ranks, merging of tables will dominate computational time, and holding the table will dominate memory usage. Here we describe a way to solve this problem. The method is however not currently implemented into the code.

For the ray plane cell at level  $L$  with position  $(i_x, i_y)$  counted in number of cells, we define the unique index

$$i = \left[ \sum_{l=L_{min}}^{L-1} 4^l \right] + i_x + 2^L i_y + 1, \quad (55)$$

where  $L_{min}$  is the level of RAMSES' uniform root grid. Each rank constructs a ray hash table as previously described, but using  $i$  as table value instead of an enumeration of the rays. Consider an arbitrary rank  $R$ . RAMSES holds a set of Hilbert key intervals that describe which cells belongs to each rank. We proceed to compute a set of bounding boxes for the cells on rank  $R$  from the Hilbert key intervals. Sets of bounding boxes are likewise computed on  $R$  for the remaining ranks. The projection of such a bounding box on the ray plane corresponds to a set of hash keys. For each rank  $r$ , we can take the union of its projected bounding boxes with those of  $R$ . These areas are mapped to a set of hash keys. Those keys and their values are extracted and sent to rank  $r$ . After applying this operation on all ranks, every rank has a table of all rays that intersects it's cells. Ray points are generated, and interpolated to, as previously described. We can however not achieve uniform load balancing by taking equal size domains in the ray index, since it is now sparse. We can instead get a statistically approximately uniform load balancing by shuffling the rays over the ranks. This can be done in many ways. An example is to assign ray  $i$  to rank  $r$  according to  $r = i \bmod n_{\text{ranks}}$ , where  $n_{\text{ranks}}$  is the total number of ranks.

With these modifications the rest of the method can proceed as previously described. Note that in order to support more than 21 levels of refinement, an 8 byte integer is not enough to represent the ray index, so one must construct an integer type of 16 bytes. Likewise the hash keys must be triples of 8-bit integers.

### 3.5 Boundary conditions

We have implemented the following boundary conditions for the radiation. A prescribed incoming intensity ( $I(0) = I_0$ ,  $I(L) = I_L$ ), which is useful in test problems, radiative equilibrium ( $I(0) = S(0)$ ,  $I(L) = S(L)$ ), and periodic boundaries for the radiation. Periodicity is useful in situations with periodic boundaries for the hydrodynamics, when the optical depth is also a fraction of the domain size. Intersection between a cell, given by its centre  $\mathbf{c}$  and size  $\Delta x$ , and a ray, given by a direction vector  $\mathbf{r}$  and a displacement vector  $\mathbf{p}$ , is tested by transporting  $\mathbf{c}$  along  $\mathbf{r}$  to the ray plane and looking up the ray at the location in a hash table, as described in Sect. 3.1. Let  $a_z$  denote the axis along which  $\mathbf{r}$  has the largest component, and  $\mathbf{c}'$  the transported cell centre. To get periodicity around the four faces perpendicular to  $a_z$ , we can simply take  $\mathbf{c}' \rightarrow (\mathbf{c}' \bmod L)$  before consulting the hash table. To also get periodicity along axis  $a_z$ , we repeat the intersection test twice more, with  $\mathbf{c}$  translated one box length along axis  $a_z$  in the positive and negative direction, i.e.  $\mathbf{c}'' = \mathbf{c}_a \pm L\mathbf{a}$ . The intersection is further discarded if  $\mathbf{c}''$  is more than a fraction  $f$  of  $L$  outside the box, where  $f$  is an adjustable parameter. The solution on the part of the ray that is outside the box along axis  $a_z$  is discarded, as the domain is already covered entirely by rays periodic over four faces. The discarded part only acts to provide a similar environment, which will be the case if the optical depth over the distance  $f \cdot L$  is large. A boundary condition is however still required for the ray, and can be one of those mentioned in the beginning of the section. If a significant fraction of the volume is optically thin, this will not accomplish a perfectly periodic box, but still be a very good approximation. If this is critical for a model convergence can be checked by running several simulations with different values of  $f$ .

## 4 TESTS

LAMPRAY is applied to a set of test problems where the result can be compared to a well-known analytical solution or to other established codes. The tests include the expansion of an HII region around a new star (Test 1), trapping

of an ionization front by a dense clump of gas (Test 2), photo-evaporation of a dense clump by ionising radiation (Test 3), the chemical structure of a plane-parallel photon dominated region (Test 4), and of a spherical, externally irradiated molecular cloud (Test 5).

The C2RAY-based ionization chemistry implementation has previously been tested in a code comparison on the D-type expansion of an HII region (Bisbas et al. 2015).

#### 4.1 TEST 1: HII region expansion

The cosmological code comparison papers Iliev et al. (2006) and Iliev et al. (2009) include a series of four tests with the expansion of an HII region around a point source. We reproduce three of these here, starting with a monochromatic source in an isothermal, static, uniform density medium, then replacing the source with a  $T = 10^5$  K black body and including heating and cooling, and finally also including hydrodynamics.

We use KROME to evolve the chemistry, with a network consisting of H,  $H^+$ , and electrons, and the only reactions are photo-ionization with cross section given in Verner & Ferland (1996), and electron recombination, where the test specifies a case B recombination rate of  $\alpha_B = 2.59 \times 10^{-13} (T/10^4 \text{K})^{-3/4} \text{cm}^6 \text{s}^{-1}$ . When heating and cooling is included, this is done as follows. Photo-ionization heating is given by

$$G(H) = n_H \int_{\nu_0}^{\infty} F_\nu h(\nu - \nu_0) \sigma_\nu(H) d\nu \quad (56)$$

(e.g. Osterbrock (1989)). The dominant cooling processes are recombination cooling and free-free emission cooling. We also include collisional ionization and excitation cooling of H. All cooling rates are from Cen (1992a). We employ 6 logarithmically spaced frequency bins with photon energy from 13.6 to 100 eV.

In all three tests, the initial number density is  $n_H = 10^{-3} \text{cm}^{-3}$  of only atomic hydrogen, ionising photon rate  $\dot{N}_\gamma = 5 \times 10^{48} \text{photons s}^{-1}$ , a recombination coefficient for  $H^+ + e^-$  of  $\alpha_B = 2.59 \times 10^{-13} (T/10^4 \text{K})^{-3/4}$ , and simulation time  $t_{\text{sim}} = 500 \text{Myr}$ .

##### 4.1.1 TEST 1.1: Isothermal gas

The first test reproduces Iliev et al. (2006) Test 1, which has monochromatic radiation with photon energy 13.6 eV, is isothermal at  $T = 10^4$  K, has box length  $L = 6.6$  kpc, and is resolved by  $128^3$  cells. At the final time, the ionization front is spherical (Fig. 11) with ionization structure in good agreement with the benchmark codes. The transition thickness is close to the theoretically expected  $18\lambda_{\text{mfp}} = 0.74$  kpc for monochromatic radiation, where  $\lambda_{\text{mfp}}$  is the photon mean free path. After the very early time, the size of the front differs by less than 5% from the analytically predicted radius (Fig. 9). Being explicit in time, our method requires a relatively small time step to follow the time evolution correctly. The bump around  $t = 0.3 t_{\text{rec}}$  is due to a change in the time step there, which is set explicitly rather than by a Courant condition. Looking at spherically averaged profiles of the ionization and neutral fraction (Fig. 10), the result agrees very well with the benchmarked ray tracing codes at both  $t = 30 \text{Myr}$  and  $t = 500 \text{Myr}$ .

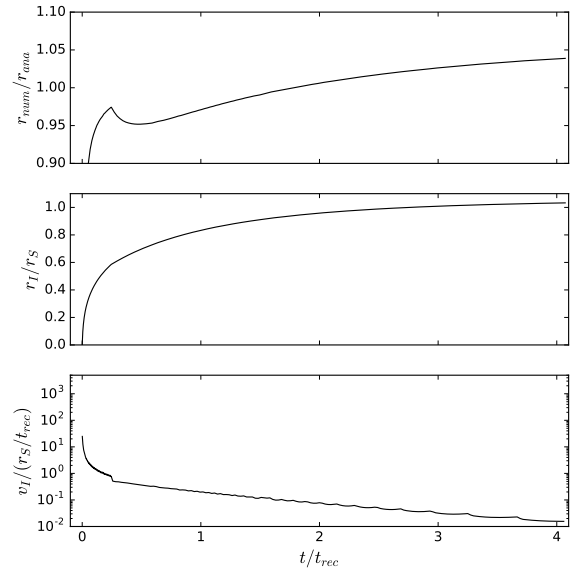


Figure 9. Test 1.1: Position and velocity of the ionization front in a uniform gas at fixed temperature.

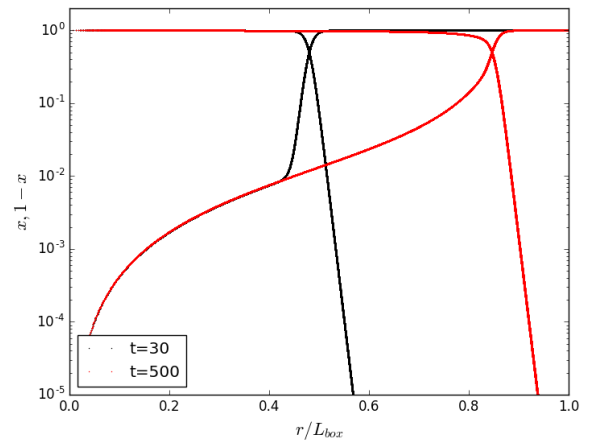
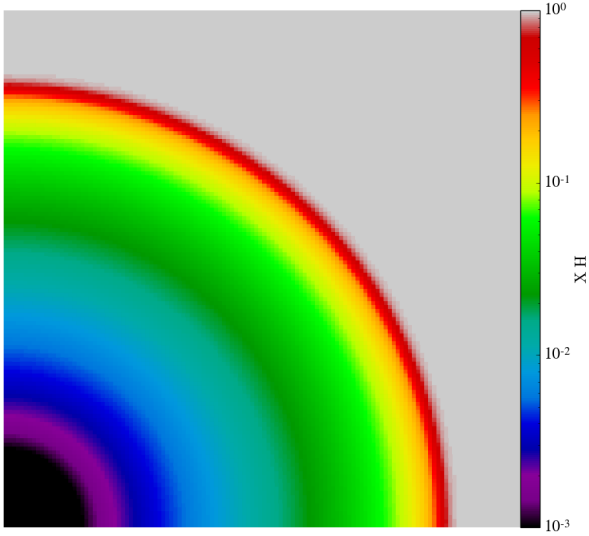


Figure 10. Test 1.1: ionization fraction ( $x = n_{H^+}/n_{H_{\text{tot}}}$ ) and neutral fraction ( $x - 1$ ). All cells are plotted, so the width of the lines show the spread at a given radius.

##### 4.1.2 TEST 1.2: Non-isothermal gas

The second test reproduces Iliev et al. (2006) Test 2, which has initial temperature  $T = 100$  K and includes heating and cooling. The box length is still  $L = 6.6$  kpc. Again, the ionization structure agrees well, especially with the ray tracing codes (Fig. 14), and the temperature structure is similar to that of especially RSPH, with significant pre-heating due to spectral hardening, i.e. the effect that high energy photons are predominately preserved at high optical depth since the cross section is lower at high energy. The time evolu-



**Figure 11.** Test 1.1: Neutral fraction, cut through volume at  $z=0$  at time  $t=500$  Myr. The entire 6.6 kpc box is shown.

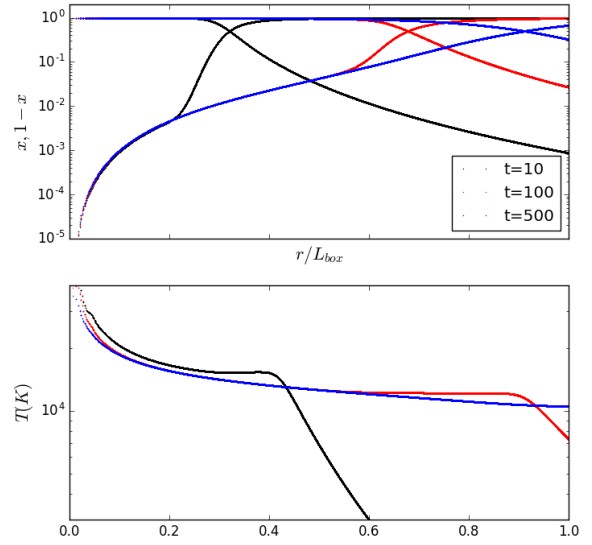


**Figure 13.** Test 1.2: Ionized and neutral fraction (top) and gas temperature (bottom) at 10, 100 and 500 Myr.

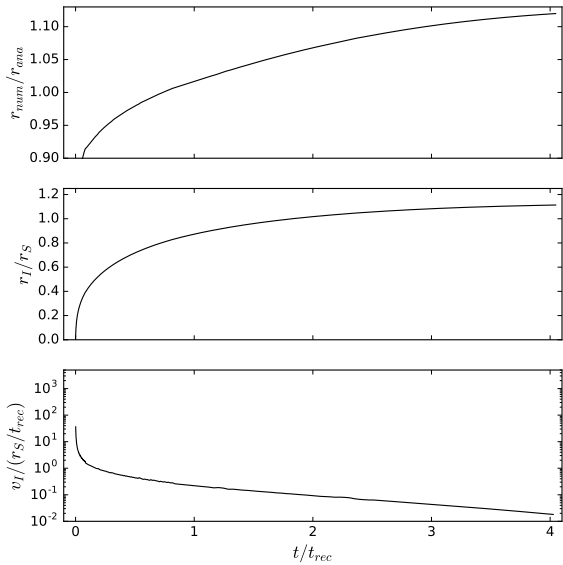


**Figure 12.** Test 1.2: Position and velocity of the ionization front in a uniform gas with varying temperature.

tion of the ionization front (Fig. 12) is similar to that of C2RAY, RSPH, and FTTE, the final size being larger than the isothermal Strömgen radius due to a higher temperature and consequently lower recombination rate. Spherically averaged profiles (Fig. 13) confirms this agreement in ionized and neutral fraction at all radii, and the agreement on temperature with RSPH.

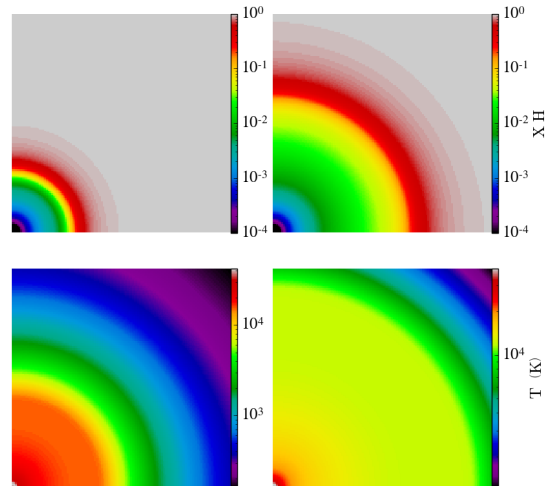


**Figure 14.** Test 1.2: Neutral fraction (top) and temperature (bottom), cut through volume at  $z=0$  at time  $t=10$  (left) and  $t=100$  Myr (right).

#### 4.1.3 TEST 1.3: Hydrodynamics

The third test reproduces Iliev et al. (2009) Test 5. It has the same parameters as Test 1.2, except that the box length is  $L = 15$  kpc and hydrodynamics is included. The position of the ionization front (Fig. 16) follows the agreement of all the benchmarked codes except ENZO, which is monochromatic. In density and Mach number, the double peak at  $t \approx 200$  Myr due to thermal expansion from pre-heating by

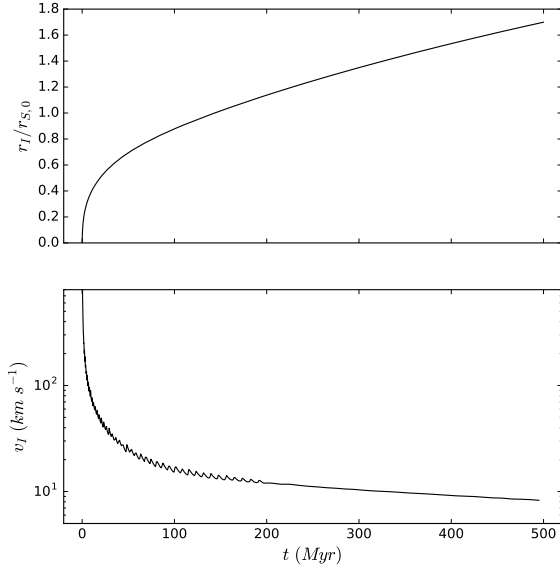


**Figure 15.** Test 1.3: Position and velocity of ionization front with gas expansion in an initially uniform gas.

hard photons seen by the remaining codes is recovered, and the radial structure lies within the relatively large scatter between the codes, most closely resembling those with similar temperature structure in the previous test. Cuts through  $z = 0$  (Fig. 17 and Fig. 18) show nicely spherical profiles that resemble those of the same codes. The test is repeated on an adaptive mesh using a  $32^3$  root grid and 2 levels of refinement with a similar result (Fig. 19).

## 4.2 TEST 2: ionization front trapping by a dense clump

This test is a replication of Test 3 from the code comparison paper Iliev et al. (2006). It tests hydrogen photo-ionization chemistry and related heating and cooling processes, as well as the diffusivity of radiation transport and ability to form a shadow. The setup is briefly repeated here. The simulated volume is resolved by  $128^3$  cells, is cubic with side length  $L = 6.6$  kpc, filled with only atomic hydrogen of uniform number density  $n_{\text{out}} = 2 \times 10^{-4} \text{ cm}^{-3}$  and initial temperature  $T_{\text{out,init}} = 8000$  K. A dense clump with radius  $r_{\text{clump}} = 0.8$  kpc has centre  $(x_c, y_c, z_c) = (5, 3.3, 3.3)$  kpc, number density  $n_{\text{clump}} = 200 n_{\text{out}}$  and initial temperature  $T_{\text{clump,init}} = 40$  K. A photon flux  $F = 10^6 \text{ cm}^{-2} \text{ s}^{-1}$  with a black body spectrum with effective temperature  $T_{\text{eff}} = 10^5$  K enters the box at  $x = 0$  and propagates along the x-axis. The chemical model is the same as in Test 1.

The time evolution of the ionization front after it reaches the clump, agrees well with the other codes, trapping the front a bit beyond the clump centre (Fig. 20). However, the position at the first two time steps deviates, because our time step of 0.2 Myr is too large to resolve the fast propagation through the thin medium. When at 1 Myr the clump reaches the front, but is not yet trapped, the clump

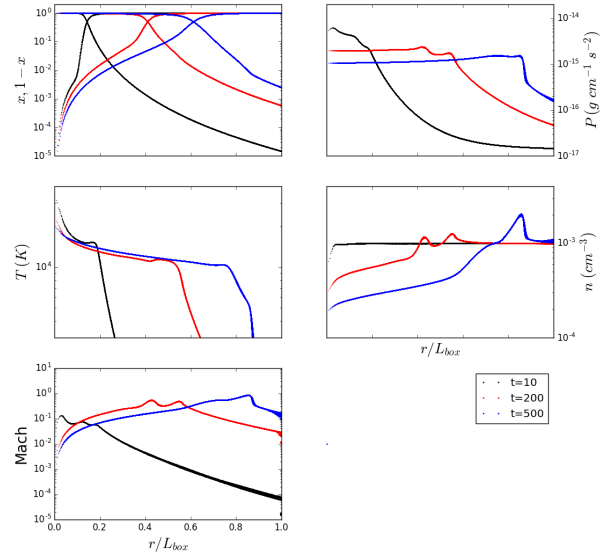


**Figure 16.** Test 1.3: The panels show the ionization and neutral fraction, pressure, temperature, total number density and Mach number.

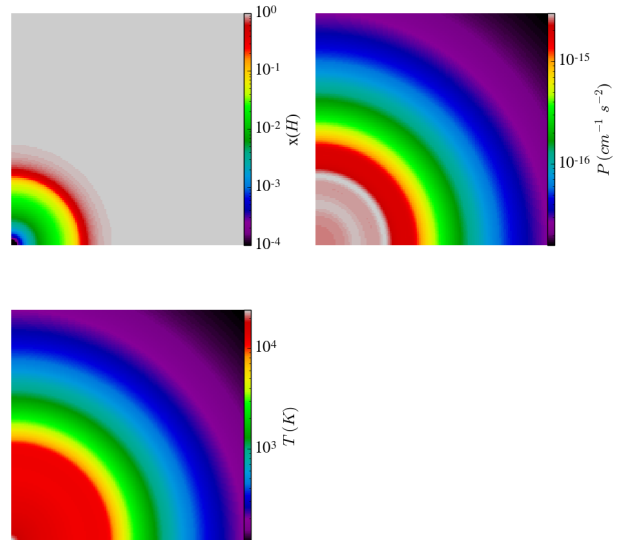


**Figure 17.** Test 1.3: Neutral fraction, pressure and temperature, cut through volume at  $z=0$  at time  $t=100$  Myr

casts a sharp shadow (Fig. 21), which is both apparent in neutral fraction and temperature. Note that though similar, the color scale is not identical to the one used by Iliev et al. (2006). The final ionization structure at 15 Myr also agrees well with the other codes except CRASH, which ionizes a smaller region and forms a stronger shadow. The temperature structure mostly resembles that of FLASH-HC, RSPH, and CORAL, which find relatively low self-shielding, and correspondingly higher temperatures in the shadow. The loca-

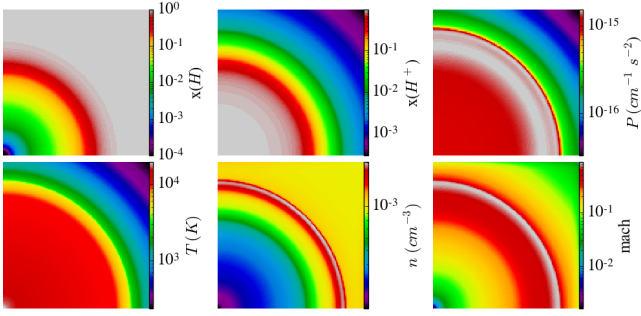


**Figure 18.** Test 1.3: Neutral fraction, ionized fraction, pressure, temperature, total number density and Mach number, cut through volume at  $z=0$  at time  $t=500$  Myr

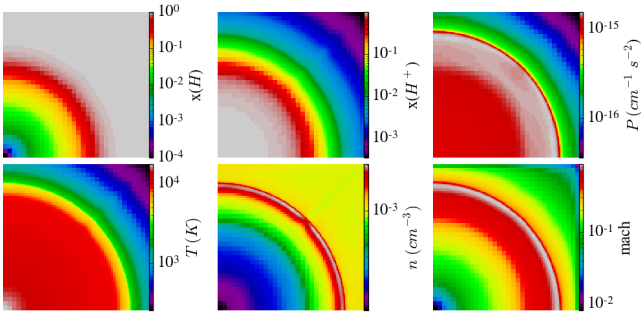


**Figure 19.** Test 1.3: Same as Fig. 18 except run with adaptive mesh refinement turned on using a  $32^3$  root grid and 2 levels of refinement.

tion of the ionization front agrees well with the majority of the other codes (Fig. 22), with a sharp transition when the clump is reached at 1 Myr, and a final extent above average of the participating codes, due to the lower recombination rate caused by the higher temperature. And like the majority of the codes, we see pre-heating of the clump, and no significant heating of the shadow at 3 Myr. Like the codes with low self-shielding, at 15 Myr the shadow has heated up, in our case by roughly a factor of 2.

### 4.3 TEST 3: Photo-evaporation of a dense clump

This test corresponds to Test 7 from the code comparison paper [Iliev et al. \(2009\)](#). It is identical to the above test, except hydrodynamics is included, allowing the clump to evaporate. At 1 Myr, the gas is still almost static, and the structure resembles the previous test, with virtually no flaring from the ionization front (Fig. 23). The evolution of position and velocity also agrees well with the majority of the other codes (Fig. 24). Like for FLASH-HC, there is a small asymmetry on the side facing the radiation at 10 Myr, which is magnified by the expansion to be clearly visible at 50 Myr (Fig. 23). It is due to the discretisation of the initial condition, and is absent for the other grid codes because their initial conditions have been smoothed ([Iliev et al. 2009](#)). The evolution of position, temperature, and pressure along the axis of symmetry generally agrees well with other codes (Fig. 25). The

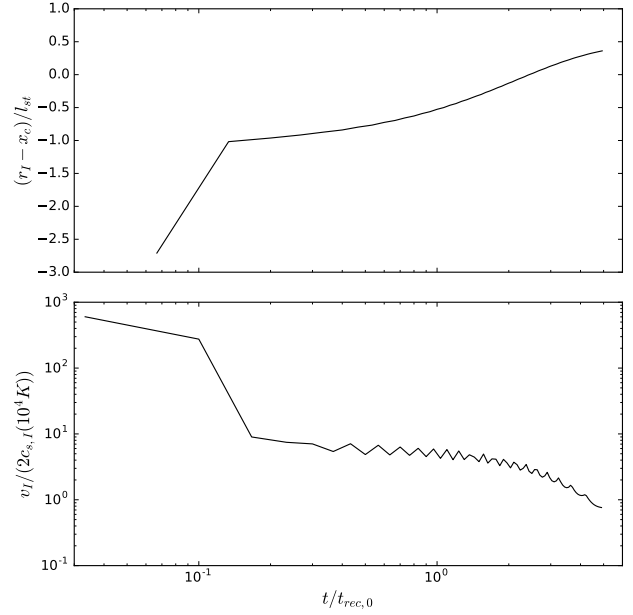


**Figure 20.** Test 2: Position and velocity of the ionization front along the axis of symmetry through the clump in a static density field.

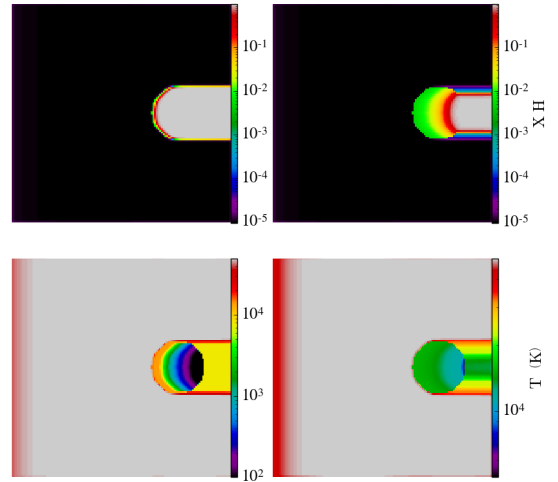


**Figure 21.** Test 2: Slices through the central plane showing the neutral fraction and temperature at times 1, 3 and 15 Myr.

test is repeated on an adaptive mesh using a  $32^3$  root grid, and 2 levels of refinement with similar results (Fig. 26).

### 4.4 TEST 4: Plane-parallel PDR

A motivation for developing the present method is to study the effect of the interstellar radiation field on molecular clouds. Therefore we wish to test it on the case of a PDR.



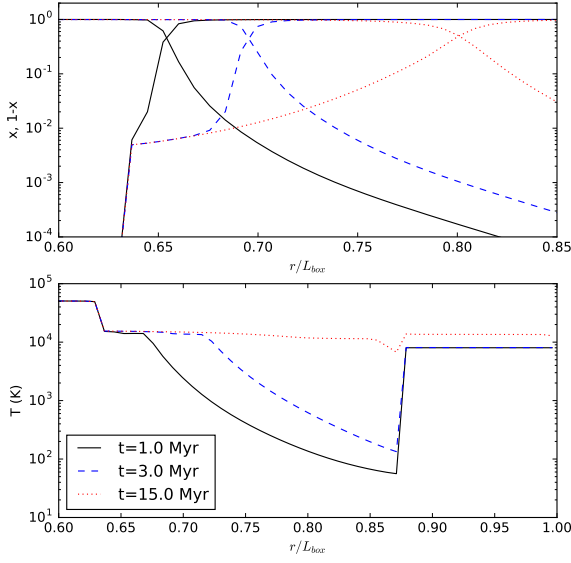


**Figure 22.** Test 2: Neutral and ionized fraction, and temperature along the axis of symmetry through the clump.

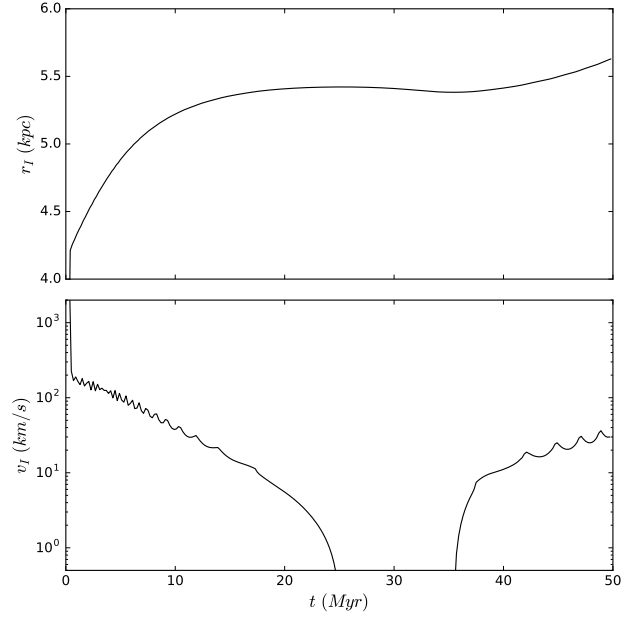


**Figure 24.** Test 3: Position and velocity of the ionization front along the axis of symmetry through the photo-evaporating clump.

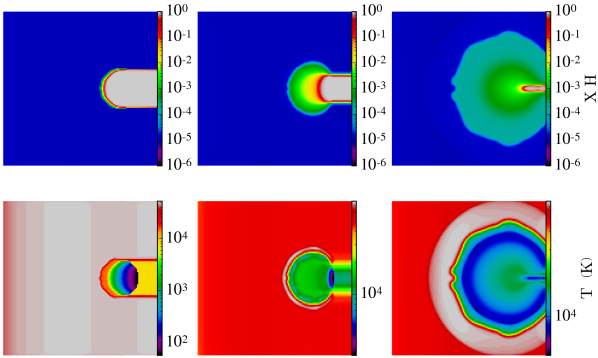


**Figure 23.** Test 3: Slices through the central plane showing the neutral fraction and temperature at times 1, 10 and 50 Myr.

The problem is so rich in micro-physical processes that no consensus solution exists, even in the simplified case of a uniform density, plane parallel PDR (see e.g. the code comparison by Röllig et al. 2007). Major codes use very large chemical networks, a large number of frequency bins and track excitation states of species in detail. For 3D hydrodynamical simulations we need to restrict ourselves to a simple network and a handful of frequency bins.

We have tested our code using the PDR setup described

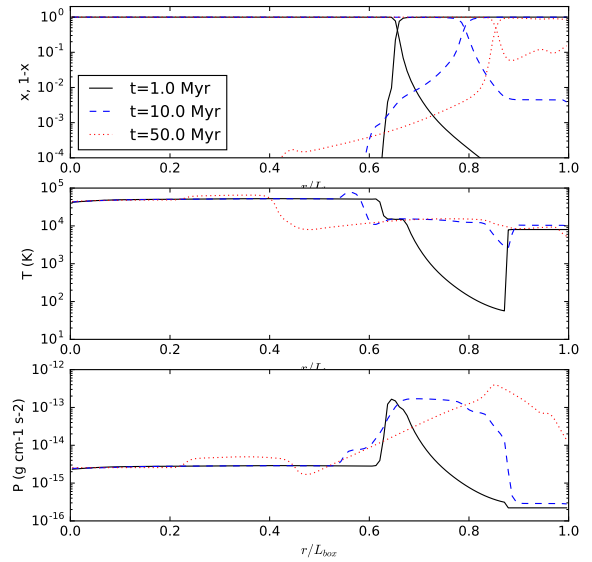


**Figure 25.** Test 3: Neutral and ionized fraction, and temperature along the axis of symmetry through the photo-evaporating clump.

in Richings et al. (2014a,b). They employ an H-He-C-O network with additional metals that are important for cooling, the ISRF from Black (1987), and a modified version of the H<sub>2</sub> and CO self-shielding prescriptions by Draine & Bertoldi (1996). Compared to our network, Richings et al. (2014b) includes additional metal coolants, but does not include ices.

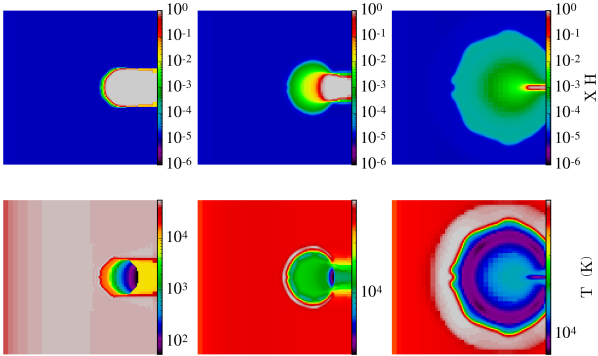


**Figure 26.** Test 3: Same as Fig. 23, but with adaptive mesh refinement turned on using a  $32^3$  root grid and 2 levels of refinement.

The complete network we are using, including references and explicit formulas for the reaction rates, is detailed in appendix A. Seven frequency bins are used, with limits in eV (5, 11.26, 13.6, 16.50, 24.6, 31.43, 54.4, 100) corresponding to a region for the dust-dominated UV part, plus the ionization threshold of C, H, He, and  $\text{He}^+$ , where 16.50 eV and 31.43 eV are two additional limits added to improve the accuracy (see Sect. 2.2.1).

The tests fall in two parts. The first part aims to test the network. This part is conducted as stand-alone tests where a simple 1D solver<sup>2</sup> coupled to KROME is used together with the choice of frequency bins, and the self-shielding prescription. The second part aims to test the network, frequency bins, and self-shielding incorporated in RAMSES, where additional issues can arise because of the coordinate geometry and the interpolation from rays to cells.

The first test attempts to reproduce the results reported in Fig. 2 of Richings et al. (2014b). The setup is 1D with a uniform gas with fixed density  $n_{\text{H,tot}} = 100 \text{ cm}^{-3}$ , gas temperature  $T_{\text{gas}} = 100 \text{ K}$ , and dust temperature  $T_{\text{d}} = 10 \text{ K}$ , and incident radiation corresponding to the ISRF from Black (1987). The initial composition is solar (Wiersma et al. 2009), neutral, and atomic, except for hydrogen, for which initially  $n_{\text{H}} = n_{\text{H}_2} = \frac{1}{3}n_{\text{H,tot}}$ , giving initial number densities  $n_{\text{H}} = 33.3 \dots \text{ cm}^{-3}$ ,  $n_{\text{H}_2} = 33.3 \dots \text{ cm}^{-3}$ ,  $n_{\text{He}} = 10 \text{ cm}^{-3}$ ,  $n_{\text{C}} = 2.46 \times 10^{-2} \text{ cm}^{-3}$ ,  $n_{\text{O}} = 4.90 \times 10^{-2} \text{ cm}^{-3}$ . The grid consists of 256 logarithmically spaced points. We use the chemical network described above, except, to ease comparison, in this test we use the same rate coefficient for  $\text{H}_2$  formation on dust grains (reaction 236 in Tab. A1) as is used in Richings et al. (2014b). The ionization transition to  $\text{H}^+$  and  $\text{He}^+$ , and the dissociation transition for  $\text{H}_2$  agrees well with Richings'

result (Fig. 27). There is roughly a 50% deviation in the optically thin ionization degree of  $\text{He}^+$ , which is due to the coarseness of frequency bins. The locations of the molecular transitions for CO and OH resemble those of Richings et al. (2014b), but their optically thick abundances differ factors of 2 and 7 respectively. This is mainly due to a different electron balance. Our model has almost two orders of magnitude less electrons here because we leave out the heavier metals, which would otherwise donate electrons through cosmic ray ionization. Among other things, this allows for a higher abundance of  $\text{H}_3\text{O}^+$ , which is the main reactant in the production of OH, and of  $\text{HCO}^+$  which recombines to CO and H.

In Fig. 28 the formation of  $\text{H}_2\text{O}$  and CO ice is also included. In this case, O is bound in ice in the optically thick region, so the OH abundance is lowered by a factor of around 30. The abundances of  $\text{HCO}^+$  and  $\text{H}_3\text{O}^+$  are lowered by a similar amount, resulting in an increase in electron abundance on the same order and lower production of CO and OH. This result implies that ice formation can significantly affect observationally important molecules like OH and  $\text{HCO}^+$ . Note that our model does not consider charged dust, which could also affect the electron density.

As has been mentioned, the previous two runs were performed with a constant dust temperature of 10 K, and the same rate of formation of  $\text{H}_2$  on dust grains as is used in Richings et al. (2014b). In Fig. 29 is shown the result of using a tabulated dust temperature and  $\text{H}_2$  formation on dust treated as described in Sect. 2.5. The dust temperature now depends on intensity, and is therefore higher in the optically thin region. This in turn gives a higher  $\text{H}_2$  formation rate, which gives a higher  $\text{H}_2$  abundance here, and moves the dissociation front of  $\text{H}_2$ , as well as the fronts of CO and OH that are controlled by shielding from  $\text{H}_2$ , to lower  $A_{\text{V}}$ . In the optically thick region, the dust temperature becomes slightly lower, leading to a higher degree of freezeout, mainly visible in CO.

Richings et al. (2014b) also compute a pressure and thermal equilibrium model, given in their Fig. 4. We use the resulting density and temperature profile as input to our model. In this test, to ease comparison, we again use  $T_{\text{d}} = 10 \text{ K}$  and the same rate coefficient for  $\text{H}_2$  formation on dust gains as is used in Richings et al. (2014b). The results are compared in Fig. 30. The location of the ionization front of H, and the dissociation fronts of  $\text{H}_2$ , CO, and OH agree fairly well. However, there are some differences in the optically thick part. As compared with the previous test, the temperature here is lower ( $T_{\text{gas}} \approx 50 \text{ K}$ ) as is the density ( $n_{\text{H,tot}} \approx 14 \text{ cm}^{-3}$ ). In contrast to the previous test, the electron density is now in agreement. Our CO abundance is roughly a factor of four higher, but our OH abundance is now lower, where in the previous test it was higher.

We now turn to the tests of the implementation in RAMSES. They are similar to the previous test in that they use constant pressure, with  $nT = 10^3 \text{ K cm}^{-3}$  as a model for an ISM in pressure equilibrium, except that at high densities a temperature floor is imposed at  $T = 10 \text{ K}$  for the gas temperature, to emulate an isothermal molecular cloud. The num-

<sup>2</sup> <https://bitbucket.org/troelsfrostholtm/tinypdr> (commit 1ba85af)

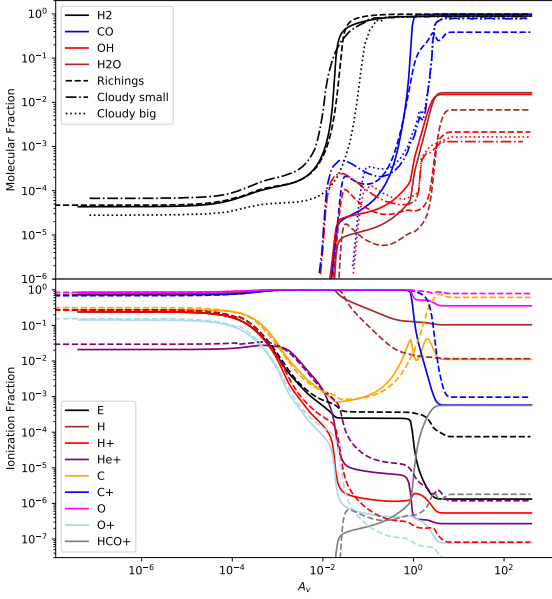


**Figure 27.** Test 4: ionization and molecular fractions of 1D PDR test in a uniform density medium. Dashed lines are from Richings et al. (2014b) Fig. 2, and include their results compared to a small and large Cloudy PDR model. We use the same formation rate of H<sub>2</sub> on dust grains as Richings, at a constant dust temperature of 10 K. In the top panel are shown H<sub>2</sub>:  $n_{\text{H}_2}/n_{\text{H}_{\text{tot}}}$ , CO:  $n_{\text{CO}}/n_{\text{C}_{\text{tot}}}$ , OH:  $n_{\text{OH}}/n_{\text{O}_{\text{tot}}}$  and H<sub>2</sub>O:  $n_{\text{H}_2\text{O}}/n_{\text{O}_{\text{tot}}}$ . In the lower panel are shown E:  $n_e/n_{\text{H}_{\text{tot}}}$ , H:  $n_{\text{H}}/n_{\text{H}_{\text{tot}}}$ , H<sup>+</sup>:  $n_{\text{H}^+}/n_{\text{H}_{\text{tot}}}$ , He<sup>+</sup>:  $n_{\text{He}^+}/n_{\text{He}_{\text{tot}}}$ , C:  $n_{\text{C}}/n_{\text{C}_{\text{tot}}}$ , C<sup>+</sup>:  $n_{\text{C}^+}/n_{\text{C}_{\text{tot}}}$ , O:  $n_{\text{O}}/n_{\text{O}_{\text{tot}}}$ , O<sup>+</sup>:  $n_{\text{O}^+}/n_{\text{O}_{\text{tot}}}$ , and HCO<sup>+</sup>:  $n_{\text{HCO}^+}/n_{\text{C}_{\text{tot}}}$ .

ber density is

$$n(r) = \begin{cases} n_0 & r < r_0 \\ n_0 \cdot 10^{\beta r} & r_0 < r < r_1 \\ n_1 & r_1 < r \end{cases} \quad (57)$$

with  $n(r_1) = n_1$ . We choose  $n_0 = 10^{-2} \text{ cm}^{-3}$ ,  $n_1 = 10^3 \text{ cm}^{-3}$ , and  $A_{v,1} = 10$ , and derive

$$\beta = \frac{n_0}{N_1 \ln(10)} \left( \frac{n_1}{n_0} - 1 \right) = 5.36 \cdot 10^{-2} \text{ pc}^{-1} \quad (58)$$

with  $N_1 = \frac{1}{4 \times 10^{-22}} A_{v,1}$  (conversion factor from Krumholz et al. 2011)) and

$$r_1 = \beta^{-1} \log\left(\frac{n_1}{n_0}\right) = 93.28 \text{ pc}. \quad (59)$$

We set  $r_0 = \frac{1}{4} r_1$ . The region  $r < r_0$  initially has H ionized. In this test we further use the representation of the ISRF as a diffuse emission as described in Sect. 2.3, with emissivity set such that the total energy flux is consistent with an external ISRF from Black (1987), namely to  $j_{*,\nu,0} = \frac{J_{\nu,\text{Black}}}{L}$ , where  $L$  is the side length of the simulation box. The RAMSES run is in 3D, using plane-parallel slab geometry, a single ray direction, and periodic boundaries

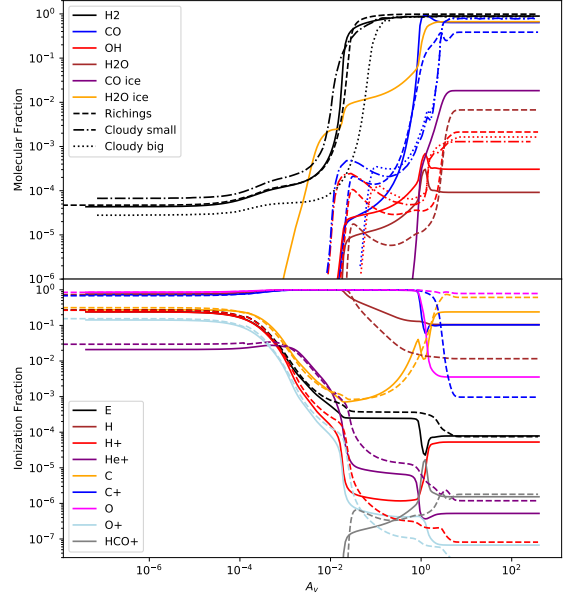


**Figure 28.** Test 4: Same as Fig. 27, except that H<sub>2</sub>O and CO ices are included in the network. In the top panel the additional labels are CO ice:  $n_{\text{CO(ice)}}/n_{\text{C}_{\text{tot}}}$  and H<sub>2</sub>O ice:  $n_{\text{H}_2\text{O(ice)}}/n_{\text{O}_{\text{tot}}}$ .

on the four orthogonal faces. The result is shown in Fig. 31, where the expected agreement between the stand-alone code and the implementation in RAMSES is seen.

#### 4.5 TEST 5: Spherical PDR

The final PDR test uses the same density and temperature profile as above, but with  $r$  being the radius in a spherically symmetric cloud. 192 HEALPIX directions are used ( $N_{\text{side}} = 4$ ), with outflow boundaries for the radiation on all faces. The emission is set such that we get one Black flux at a distance of  $r_0 + r_1$ . This is equivalent to a total photon rate in the emitting region of

$$\dot{N}_{\text{phot}} = (4\pi)^2 (r_0 + r_1)^2 \int_0^\infty J_\nu^{\text{Black}} / (h\nu) d\nu. \quad (60)$$

The resolution is  $64^3$  cells. Results are in Fig. 32. In the stand-alone reference run, the geometry of the problem must be taken into account. The mean (angle averaged) intensity  $J$  due to absorption only, a distance  $x$  from the centre of a spherical cloud of radius  $r$ , assuming an isotropic radiation field outside the cloud of  $J_{\text{out}} = 1$  is given by

$$J(x) = \frac{1}{2x} \{E_3(r-x) - E_3(r+x) + rE_2(r-x) - rE_2(r+x)\} \quad (61)$$

(van de Hulst 1987, Eqn. 26), where  $x$  and  $r$  are in units of optical depth and  $E_n(x) = \int_1^\infty \frac{e^{-xt}}{t^n} dt$  is the  $n$ -th exponential integral. We use this equation to attenuate an external intensity due to Black (1987), where the optical depth is computed from the chemical composition and temperature

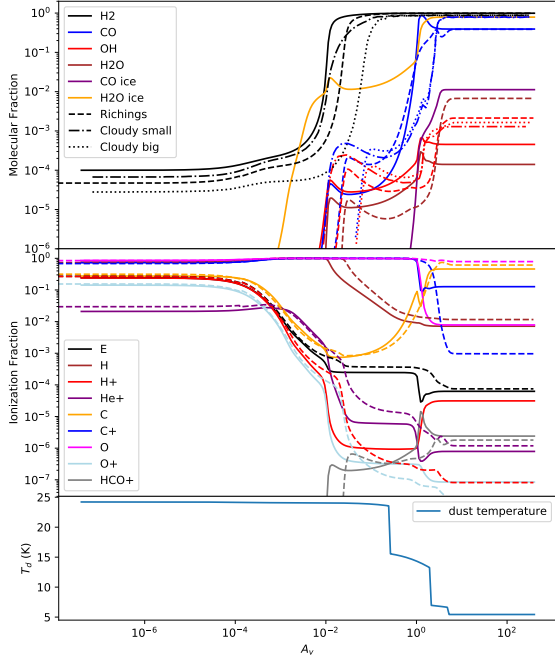


**Figure 29.** Test 4: Same as Fig. 28, except that the dust temperature (bottom panel) and  $\text{H}_2$  formation is calculated as described in Sect. 2.5.

by KROME as usual. For the photo-dissociation rates of  $\text{H}_2$  and  $\text{CO}$ , where the prescription for attenuation including self-shielding due to Richings et al. (2014b) is used, we can strictly speaking not use Eqn.(61), because the self-shielding attenuation does not follow an exponential decay along a given direction, and therefore does not correspond to a single well-defined optical depth. Ignoring this fact, from the shielding factors  $f_s^{\text{H}_2} = \mathcal{S}_d^{\text{H}_2} \mathcal{S}_{\text{self}}^{\text{H}_2}$  and  $f_s^{\text{CO}} = \mathcal{S}_d^{\text{CO}} \mathcal{S}_{\text{self}}^{\text{CO}}$  along the radial direction (see Sect. 2.4) we compute an equivalent optical depth  $\tau^i = -\log f_s^i$ , which is then transformed back to a shielding factor for the spherical cloud using Eqn.(61). The deviations seen in Fig. 32 can be due to this inconsistency, to the fact that the emission in the 3D case is not perfectly isotropic, as the emitting region is bounded by a finite cube, and/or to differences in resolution. The 1D standalone test is resolved by 256 cells.

The test is repeated with two additional levels of active mesh refinement (Fig. 33). Refinement is activated where the relative gradient in the abundance of  $\text{H}$ ,  $\text{H}^+$ , or  $\text{H}_2$  exceeds 0.2, and the corresponding abundance is above 1% by mass. In this case, the shapes of the different transitions are better resolved. In particular, the small bumps around 65 pc in  $\text{He}^+$  and  $\text{C}$  are recovered. But the construction and removal of refined mesh following the front as it expands introduces a small amount of asymmetry, which results in the scatter in the plot, with a width of roughly a single coarse cell. As seen in Fig. 34, the actual transition is perfectly smooth, and the

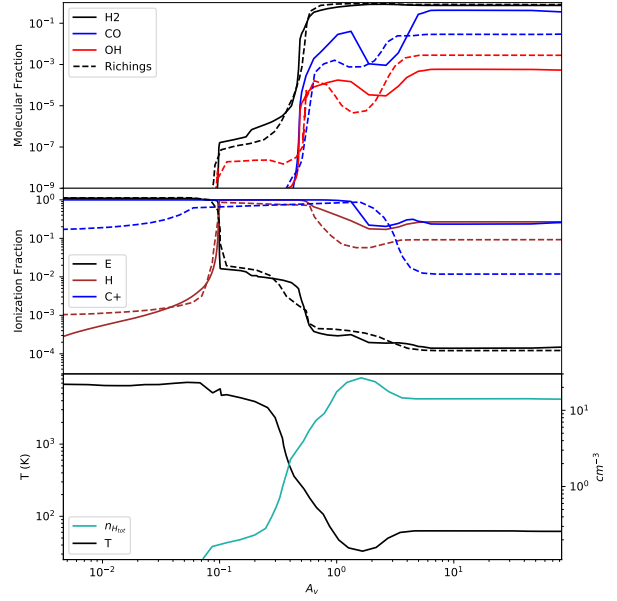


**Figure 30.** Test 4: ionization and molecular fractions of 1D PDR test with uniform pressure, but temperature and density as given in Richings et al. (2014b) Fig. 4. Species labels are as in Fig. 27

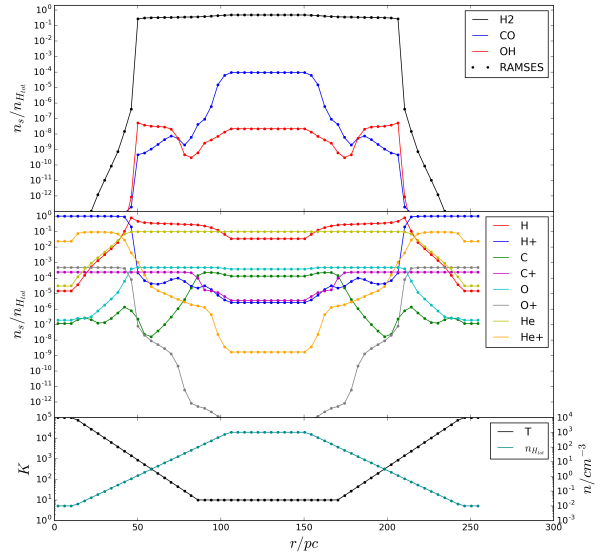


**Figure 31.** Test 4: Comparison of 1D stand-alone code (solid line) and RAMSES (dots) in an iso-pressure plane-parallel toy PDR model with a power-law density and temperature profile that roughly covers the range found in the ISM.

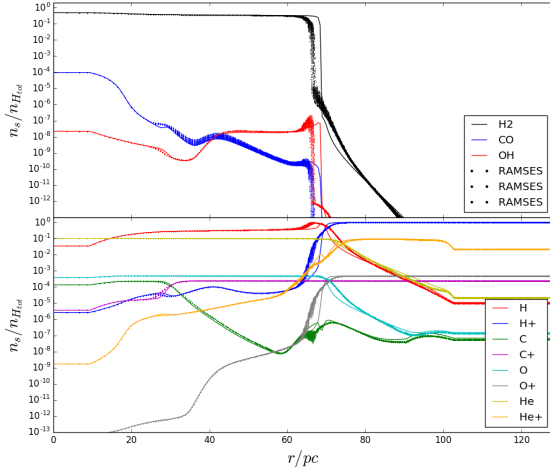


**Figure 32.** Test 5: Comparison of 1D stand-alone code (solid lines) and RAMSES (dots) in a spherically symmetric cloud with the same density and temperature profile as shown in Fig. 31. In the 1D solution, Eqn.(61) is used to account for the clouds spherical shape.

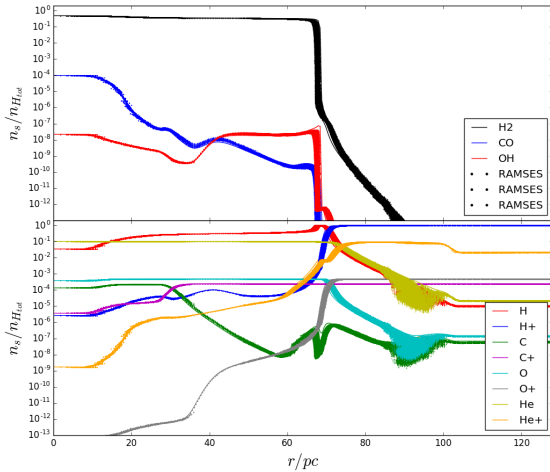


**Figure 33.** Test 5: Same as Fig. 32, but with two extra adaptive mesh levels. Refinement is applied where the relative gradient in H, H<sup>+</sup> or H<sub>2</sub> exceeds 0.2, and the abundance of that species is above 1% by mass.

scatter is due to an ever so slight non-spherical form of the ionization fronts. The noise around  $r = 90$  pc is located at the outer refinement boundary, where the abundance of H has dropped below 1%.

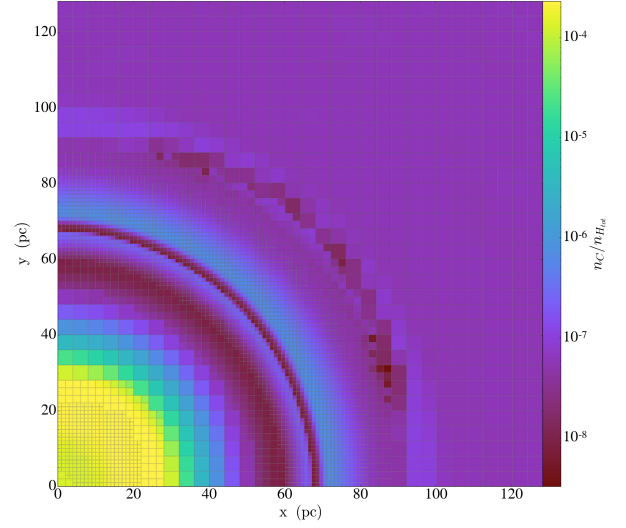


**Figure 34.** Test 5: Slice through the centre of the cloud, showing neutral C normalised to total number density of H. The noise at the edge of the cloud is at a very low abundance, and is a consequence of the specific AMR refinement criteria.

Case	level	cells	MPI ranks	OPENMP threads
A	6	64 <sup>3</sup>	8	5
	7	128 <sup>3</sup>	64	5
	8	256 <sup>3</sup>	512	5
B	6	64 <sup>3</sup>	4	8
	7	128 <sup>3</sup>	32	8
	8	256 <sup>3</sup>	256	8

**Table 2.** Resolution and resources for the weak scaling test.

## 5 PERFORMANCE AND SCALING

The weak-scaling properties of the photo-chemistry solver with KROME are measured on the spherical cloud setup of Test 5, except using 48 HEALPIX directions instead of 192. The test is performed on the local HPC cluster at University of Copenhagen using nodes with 2x 10-core Xeon E5-2680v2 running at 2.8 GHz with 64 GB DDR3-1866 MHz RAM per node interconnected with FDR infiniband. Two sets of runs are performed – one with 5 OPENMP threads per MPI rank (A) and one with 8 threads per rank (B). In both cases we exploit hyper threading and run 2 threads per core. Resolution and computational resources are given in table 2. The results are given in Fig. 35 and Fig. 36, where running time is in core  $\mu$ s per cell update averaged over 5 time steps.

While the rest of RAMSES used in Copenhagen and the coupling to KROME is OPENMP parallelised, this is not yet the case for the radiative transfer. It therefore naturally runs longer per core in case B where more OPENMP threads are available. In case B with twice as many cells per MPI rank, and which goes up to half the number of ranks as case A, the running time is roughly constant. At 256<sup>3</sup> cells on 512 ranks, the time in RT doubles. As can be seen from Fig. 37, it is because the cost of communication in RT more than doubles at this point, and becomes dominant.

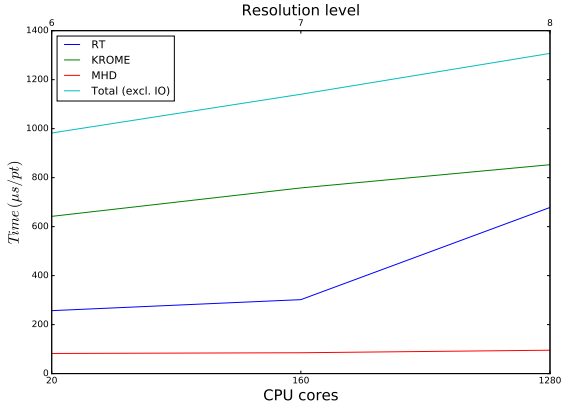


**Figure 35.** Weak scaling (case A) using 5 OPENMP threads per MPI rank.

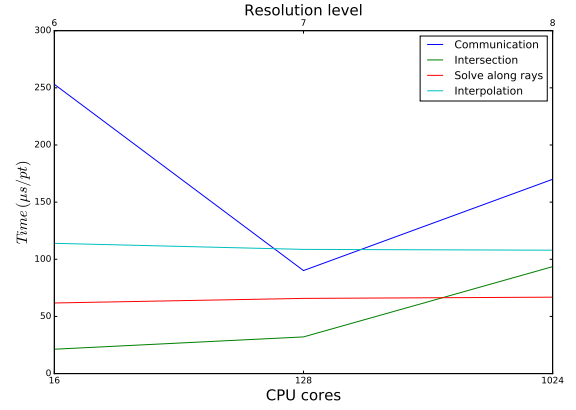


**Figure 38.** Weak scaling (case B) – timing of radiative transfer steps.

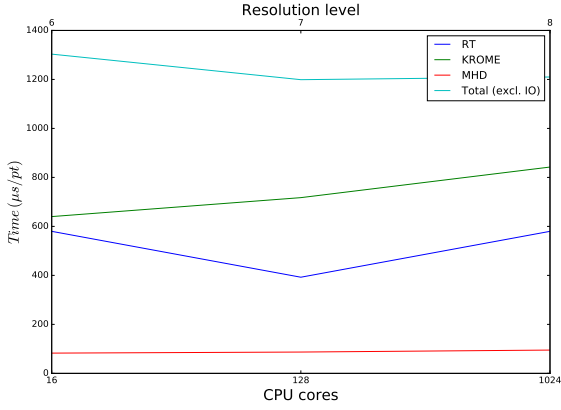


**Figure 36.** Weak scaling (case B) using 8 OPENMP threads per MPI rank.

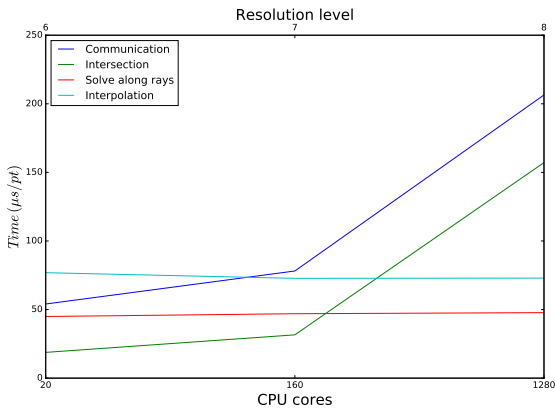


**Figure 37.** Weak scaling (case A) – timing of radiative transfer steps.

## 6 SUMMARY AND FUTURE WORK

We have presented a new method we call LAMPFRAY, and its implementation into the RAMSES code, for solving the time-independent radiative transfer problem on an adaptive octree mesh by means of tracing rays, that each cover the entire length of the domain. The diffuse radiation field is represented by rays that uniformly cover leaf cells at each refinement level for each of a set of directions chosen by the HEALPIX scheme. Because rays in highly refined cells extend into coarser cells, the coarse cells will be covered by several rays in a given direction. The radiation field due to point sources is represented by a fixed set of rays that intersects the source, also with directions chosen by the HEALPIX scheme.

The LAMPFRAY code is parallelised for computer clusters with MPI by changing the domain decomposition of the already MPI parallel RAMSES code in such a way that points along any given ray is placed optimally in the same memory space. The method is shown to scale to at least 1280 CPUs in a weak scaling test. It is shown to perform well enough to support radiation hydrodynamics with photo-ionization and -dissociation chemistry using a simplified H-He-C-O chemical network, spending between 1000 and 1300 core  $\mu$ s per point.

The radiation field is either coupled to hydrogen ionization chemistry using an implicit, photon-conserving method similar to what is used in C2RAY, or to arbitrary photo-ionization and -dissociation chemistry through a time-explicit method using the non-equilibrium chemistry code KROME. The former has previously participated in the STARBENCH code comparison on the D-type expansion of an HII region (Bisbas et al. 2015). The latter has been tested here in the following circumstances.

Using a minimal hydrogen ionization chemistry network, most of the benchmark tests in Iliev et al. (2006, 2009) have been reproduced, with good results. These include 1.1) the expansion of an HII region in static, isothermal gas, 1.2) the previous, except with heating and cooling included, 1.3) the previous, except with hydrodynamics included, 2) the trapping of an ionization front by a dense clump in a static gas, 3) and with active hydrodynamics,

letting the clump evaporate. Because the method is time-explicit, the early fast propagation of the ionization front is not well resolved, and there is some deviation in ionization front position and velocity in the earliest part of the evolution in all the tests. There is generally some disagreement among the benchmarked codes regarding the level of shielding and the temperature structure. LAMPRAY tends to agree with those that predict a relatively low level of shielding, and high temperatures, namely FLASH-HC, RSPH, and CORAL. Test 3 has been repeated with active mesh refinement, producing almost identical results.

A new model for the H-He-C-O chemistry in photon dominated regions, for use in 3D hydrodynamic simulations, has been presented. It is in part based on the network presented in Glover et al. (2010), but updated with newer reaction rates and broader temperature coverage, a better treatment of dust, explicit photo chemistry including cross sections, and inclusion of H<sub>2</sub>O and CO ices. It is compared with the model in Richings et al. (2014a,b). It includes 240 reactions, among which are photo-ionization, photo-dissociation, recombinations on dust grains, and formation of CO and H<sub>2</sub>O ices. It reproduces the ionization transitions for H, He, and C, and dissociation transition for H<sub>2</sub>, while for CO and OH, only the transition location is reproduced, while the shape differs. Electron and OH density in the optically thick part differs due to the omission of metals that would donate electrons if included.

A new method for including an interstellar radiation field in periodic boundary gas simulations has been presented, in which the interstellar field is modelled as an emissivity in the diffuse ionized medium. Using this, the above chemical model has been tested on a 3D hydrostatic model of a spherical molecular cloud. This results in stable, spherically symmetric ionization and molecular transitions that agree well with a corresponding 1D simulation presented here. The test has been repeated with active mesh refinement, which allows certain transition features to be better resolved, but also introduces a small degree of asymmetry into the solution, that slightly deforms the spherical transitions.

We envision a number of future improvements. As mentioned, coarse cells in the adaptive mesh are covered by more rays than necessary. Alleviating this problem would require fundamental changes to the method. One solution for the diffuse field would be to use the fact that one can decompose the solution to the radiative transfer equation in a set of regions into an intrinsic solution in each region, and a solution at the region boundaries (Heinemann et al. 2006). This could be exploited to find the intrinsic solution one level of refinement at a time, in the regions that are at that level. These solutions would then finally be recomposed in the ray domain, using interpolation at refinement boundaries. The downside of this method is that the solution for all ray directions, at least at the refinement boundaries, must be held in memory at once, multiplying memory consumption roughly by the number of directions. It also requires an additional communication of the intensity at refinement boundaries. For point sources, a common technique is to split rays as the distance to the source increases (Abel & Wandelt 2002).

As described, photo-ionization chemistry using the coupling with KROME is time-explicit, and therefore not well suited for tracking fast ionization fronts. By modifying the

ODE solver in KROME to also compute time-averaged ionization fractions over the time step, an implicit method like that of C2RAY could be implemented.

In RAMSES, stars may be represented as accreting point particles. The accretion history has previously been used as input to the stellar structure model MESA (Jensen & Haugbølle 2018; Kuffmeier et al. 2018), showing a significant influence on the luminosity of young stellar objects. In the future, we plan to use the stellar properties of such models to determine the spectrum of point sources, by evolving MESA in parallel with RAMSES.

## ACKNOWLEDGEMENTS

We thank Remo Collet and Åke Nordlund for useful discussions and for their contributions to the initial version of the radiative transfer framework in the version of RAMSES used at the Centre for Star and Planet Formation. We thank Alexander James Richings for kindly sharing his simulation data, to which we compare our model in the present paper. We thank the developers of the python-based analysing tool YT <http://yt-project.org> (Turk et al. 2011) that has been used to produce some of the figures. The research leading to these results has received funding from the Danish Council for Independent Research through a Sapere Aude Starting Grant to TH. The Centre for Star and Planet Formation is financed by the Danish National Research Foundation (DNRF97). We acknowledge PRACE for awarding us access to the computing resource MARCONI based in Italy at CINECA for carrying out part of the development and tests. Computing nodes at the University of Copenhagen HPC centre, funded with a research grant (VKR023406) from Villum Fonden, were used for carrying out part of the simulations and the post-processing.

## REFERENCES

- Abel T., Wandelt B. D., 2002, *MNRAS*, **330**, L53  
 Abel T., Anninos P., Zhang Y., Norman M. L., 1997, *New Astron.*, **2**, 181  
 Abel T., Norman M. L., Madau P., 1999, *ApJ*, **523**, 66  
 Adams N. G., Smith D., 1977, *Chemical Physics Letters*, **47**, 383  
 Adams N. G., Smith D., Millar T. J., 1984, *MNRAS*, **211**, 857  
 Aldrovandi S. M. V., Pequignot D., 1973, *A&A*, **25**, 137  
 Alge E., Adams N. G., Smith D., 1983, *Journal of Physics B Atomic Molecular Physics*, **16**, 1433  
 Andreazza C. M., Singh P. D., 1997, *MNRAS*, **287**, 287  
 Anicich V. G., 2003, JPL Publication 03-19, 1-1194  
 Aubert D., Teyssier R., 2008, *MNRAS*, **387**, 295  
 Azatyan V., Aleksandrov E., Troshin A., , *Kinet. Catal. (USSR)* (Engl. Transl.), v. 16, no. 2, pp. 261-265  
 Barinovs Ģ., van Hemert M. C., 2006, *ApJ*, **636**, 923  
 Barreira A., Llinares C., Bose S., Li B., 2016, *J. Cosmology Astropart. Phys.*, **5**, 001  
 Baulch D. L., et al., 1992, *Journal of Physical and Chemical Reference Data*, **21**, 411  
 Baulch D. L., et al., 2005, *Journal of Physical and Chemical Reference Data*, **34**, 757  
 Bisbas T. G., et al., 2015, *MNRAS*, **453**, 1324  
 Black J. H., 1987, in Hollenbach D. J., Thronson Jr. H. A., eds, *Astrophysics and Space Science Library* Vol. 134, *Interstellar Processes*. pp 731–744, doi:10.1007/978-94-009-3861-8\_27

- Buntemeyer L., Banerjee R., Peters T., Klassen M., Pudritz R. E., 2016, *New Astron.*, **43**, 49
- Butler M. J., Tan J. C., Teyssier R., Rosdahl J., Van Loo S., Nickerson S., 2017, *ApJ*, **841**, 82
- Cazaux S., Spaans M., 2009, *A&A*, **496**, 365
- Cen R., 1992a, *ApJS*, **78**, 341
- Cen R., 1992b, *ApJS*, **78**, 341
- Clark P. C., Glover S. C. O., Klessen R. S., 2012, *MNRAS*, **420**, 745
- Cohen N., Westberg K., 1979, *Journal of Physical Chemistry*, **83**, 46
- Commerçon B., Teyssier R., Audit E., Hennebelle P., Chabrier G., 2011, *A&A*, **529**, A35
- Commerçon B., Debout V., Teyssier R., 2014, *A&A*, **563**, A11
- Coppola C. M., Longo S., Capitelli M., Palla F., Galli D., 2011, *ApJS*, **193**, 7
- Corrigan S. J. B., 1965, *J. Chem. Phys.*, **43**, 4381
- Dale J. E., Ercolano B., Bonnelli I. A., 2013, *MNRAS*, **430**, 234
- Dalgarno A., Lepp S., 1987, in Vardya M. S., Tarafdar S. P., eds, *IAU Symposium Vol. 120, Astrochemistry*. pp 109–118
- Dean A. J., Davidson D. F., Hanson R. K., 1991, *The Journal of Physical Chemistry*, **95**, 183
- Draine B. T., 1978, *ApJS*, **36**, 595
- Draine B. T., 2009, in Henning T., Grün E., Steinacker J., eds, *Astronomical Society of the Pacific Conference Series Vol. 414, Cosmic Dust - Near and Far*. p. 453 ([arXiv:0903.1658](https://arxiv.org/abs/0903.1658))
- Draine B. T., Bertoldi F., 1996, *ApJ*, **468**, 269
- Dullemond C. P., Monnier J. D., 2010, *ARA&A*, **48**, 205
- Dunn G. H., 1968, *Physical Review*, **172**, 1
- Fairbairn A. R., 1969, *Proceedings of the Royal Society of London Series A*, **312**, 207
- Feautrier P., 1964, *SAO Special Report*, **167**, 80
- Federer W., Villinger H., Howorka F., Lindinger W., Tosis P., Bassi D., Ferguson E., 1984, *Physical Review Letters*, **52**, 2084
- Ferland G. J., Peterson B. M., Horne K., Welsh W. F., Nahar S. N., 1992, *ApJ*, **387**, 95
- Ferland G. J., Korista K. T., Verner D. A., Ferguson J. W., Kingdon J. B., Verner E. M., 1998, *PASP*, **110**, 761
- Ferland G. J., et al., 2013, *Rev. Mex. Astron. Astrofis.*, **49**, 137
- Forrey R. C., 2013, *ApJ*, **773**, L25
- Frostholtm T., 2014, Master's thesis, University of Copenhagen, Denmark
- Geppert W. D., et al., 2005, in Wolf A., Lammich L., Schmelcher P., eds, *Journal of Physics Conference Series Vol. 4, Journal of Physics Conference Series*. pp 26–31, [doi:10.1088/1742-6596/4/1/004](https://doi.org/10.1088/1742-6596/4/1/004)
- Gerlich D., Horning S., 1992, *Chemical Reviews*, **92**, 1509
- Glover S. C. O., Abel T., 2008, *MNRAS*, **388**, 1627
- Glover S. C. O., Jappsen A.-K., 2007, *ApJ*, **666**, 1
- Glover S. C. O., Mac Low M.-M., 2007, *ApJS*, **169**, 239
- Glover S. C. O., Savin D. W., 2009, *MNRAS*, **393**, 911
- Glover S. C. O., Federrath C., Mac Low M.-M., Klessen R. S., 2010, *MNRAS*, **404**, 2
- González M., Vaytet N., Commerçon B., Masson J., 2015, *A&A*, **578**, A12
- Górski K. M., Hivon E., Banday A. J., Wandelt B. D., Hansen F. K., Reinecke M., Bartelmann M., 2005, *ApJ*, **622**, 759
- Grassi T., Krstić P., Merlin E., Buonomo U., Piovani L., Chiosi C., 2011, *A&A*, **533**, A123
- Grassi T., Bovino S., Schleicher D. R. G., Prieto J., Seifried D., Simoncini E., Gianturco F. A., 2014, *MNRAS*, **439**, 2386
- Grassi T., Bovino S., Haugbølle T., Schleicher D. R. G., 2017, *MNRAS*, **466**, 1259
- Guberman S. L., 1995, *J. Chem. Phys.*, **102**, 1699
- Harada N., Herbst E., Wakelam V., 2010, *ApJ*, **721**, 1570
- Harding L. B., Guadagnini R., Schatz G. C., 1993, *The Journal of Physical Chemistry*, **97**, 5472
- Hasegawa T. I., Herbst E., 1993, *MNRAS*, **261**, 83
- Haworth T. J., Glover S. C. O., Koepferl C. M., Bisbas T. G., Dale J. E., 2018, *New Astron. Rev.*, **82**, 1
- Heinemann T., Dobler W., Nordlund Å., Brandenburg A., 2006, *A&A*, **448**, 731
- Hocuk S., Cazaux S., 2015, *A&A*, **576**, A49
- Hollenbach D., McKee C. F., 1979, *ApJS*, **41**, 555
- Hollenbach D., Kaufman M. J., Bergin E. A., Melnick G. J., 2009, *ApJ*, **690**, 1497
- Howard C. S., Pudritz R. E., Harris W. E., 2017, *MNRAS*, **470**, 3346
- Huebner W. F., Keady J. J., Lyon S. P., 1992, *Ap&SS*, **195**, 1
- Hummer D. G., Rybicki G. B., 1971, *MNRAS*, **152**, 1
- Iliev I. T., et al., 2006, *MNRAS*, **371**, 1057
- Iliev I. T., et al., 2009, *MNRAS*, **400**, 1283
- Janev R. K., Langer W. D., Post Jr. D. E., Evans Jr. K., eds, 1987, *Elementary processes in hydrogen-helium plasmas: Cross sections and reaction rate coefficients*, Springer Series on Atoms and Plasmas Vol. 4. Springer-Verlag
- Jensen S. S., Haugbølle T., 2018, *MNRAS*, **474**, 1176
- Jensen M. J., Bilodeau R. C., Safvan C. P., Seiersen K., Andersen L. H., Pedersen H. B., Heber O., 2000, *ApJ*, **543**, 764
- Jones J. D. C., Birkinshaw K., Twiddy N. D., 1981, *Chemical Physics Letters*, **77**, 484
- Karpas Z., Anicich V., Huntress W. T., 1979, *J. Chem. Phys.*, **70**, 2877
- Khokhlov A., 1998, *Journal of Computational Physics*, **143**, 519
- Kimura M., Dalgarno A., Chantranupong L., Li Y., Hirsch G., Buenker R. J., 1993, *ApJ*, **417**, 812
- Kreckel H., Bruhns H., Čížek M., Glover S. C. O., Miller K. A., Urbain X., Savin D. W., 2010, *Science*, **329**, 69
- Krumholz M. R., Leroy A. K., McKee C. F., 2011, *ApJ*, **731**, 25
- Krumholz M. R., et al., 2014, *Protostars and Planets VI*, pp 243–266
- Kuffmeier M., Haugbølle T., Nordlund Å., 2017, *ApJ*, **846**, 7
- Kuffmeier M., Frimann S., Jensen S. S., Haugbølle T., 2018, *MNRAS*, **475**, 2642
- Larson Å., et al., 1998, *ApJ*, **505**, 459
- Le Teuff Y. H., Millar T. J., Markwick A. J., 2000, *A&AS*, **146**, 157
- Leger A., Jura M., Omont A., 1985, *A&A*, **144**, 147
- Lepp S., Shull J. M., 1983, *ApJ*, **270**, 578
- Linder F., Janev R., Botero J., 1995, in , *Atomic and Molecular Processes in Fusion Edge Plasmas*. Springer, pp 397–431
- Loison J.-C., Wakelam V., Hickson K. M., Bergeat A., Mereau R., 2014, *MNRAS*, **437**, 930
- Mathis J. S., Rimpl W., Nordsieck K. H., 1977, *ApJ*, **217**, 425
- McCall B. J., et al., 2004, *Phys. Rev. A*, **70**, 052716
- McElroy D., Walsh C., Markwick A. J., Cordiner M. A., Smith K., Millar T. J., 2013, *A&A*, **550**, A36
- McEwan M. J., Scott G. B. I., Adams N. G., Babcock L. M., Terzieva R., Herbst E., 1999, *ApJ*, **513**, 287
- Mellema G., Iliev I. T., Alvarez M. A., Shapiro P. R., 2006, *New Astron.*, **11**, 374
- Millar T. J., Farquhar P. R. A., Willacy K., 1997, *A&AS*, **121**, 139
- Mitchell J. B. A., 1990, *Phys. Rep.*, **186**, 215
- Mitchell G. F., Deveau T. J., 1983, *ApJ*, **266**, 646
- Murrell J., Rodriguez J., 1986, *Journal of Molecular Structure: THEOCHEM*, **139**, 267
- Nahar S. N., 1999, *ApJS*, **120**, 131
- Nahar S. N., Pradhan A. K., 1997, *ApJS*, **111**, 339
- Nelson R. P., Langer W. D., 1997, *ApJ*, **482**, 796
- O'Connor A. P., Urbain X., Stützel J., Miller K. A., de Ruette N., Garrido M., Savin D. W., 2015, *ApJS*, **219**, 6
- Omukai K., 2000, *ApJ*, **534**, 809
- Osterbrock D. E., 1989, *Astrophysics of gaseous nebulae and active galactic nuclei*



- Padoan P., Pan L., Haugbølle T., Nordlund Å., 2016, *ApJ*, **822**, 11
- Peart B., Hayton D. A., 1994, *Journal of Physics B Atomic Molecular Physics*, **27**, 2551
- Peters T., Banerjee R., Klessen R. S., Mac Low M.-M., Galván-Madrid R., Keto E. R., 2010, *ApJ*, **711**, 1017
- Peters T., et al., 2017, *MNRAS*, **466**, 3293
- Petuchowski S. J., Dwek E., Allen Jr. J. E., Nuth III J. A., 1989, *ApJ*, **342**, 406
- Poulaert G., Brouillard F., Claeys W., McGowan J. W., Van Wassenhove G., 1978, *Journal of Physics B Atomic Molecular Physics*, **11**, L671
- Prasad S. S., Huntress Jr. W. T., 1980, *ApJS*, **43**, 1
- Rakshit A. B., Warneck P., 1980, *J. Chem. Soc., Faraday Trans. 2*, **76**, 1084
- Ramaker D. E., Peek J. M., 1976, *Phys. Rev. A*, **13**, 58
- Reboussin L., Wakelam V., Guilloteau S., Hersant F., 2014, *MNRAS*, **440**, 3557
- Richings A. J., Schaye J., Oppenheimer B. D., 2014a, *MNRAS*, **440**, 3349
- Richings A. J., Schaye J., Oppenheimer B. D., 2014b, *MNRAS*, **442**, 2780
- Rijkhorst E.-J., Plewa T., Dubey A., Mellema G., 2006, *A&A*, **452**, 907
- Roberge W. G., Jones D., Lepp S., Dalgarno A., 1991, *ApJS*, **77**, 287
- Röllig M., et al., 2007, *A&A*, **467**, 187
- Rosdahl J., Teyssier R., 2015, *MNRAS*, **449**, 4380
- Rosdahl J., Blaizot J., Aubert D., Stranex T., Teyssier R., 2013, *MNRAS*, **436**, 2188
- Rosén S., et al., 1998, *Phys. Rev. A*, **57**, 4462
- Rosén S., et al., 2000, *Faraday Discussions*, **115**, 295
- Safrank-Shrader C., Krumholz M. R., Kim C.-G., Ostriker E. C., Klein R. I., Li S., McKee C. F., Stone J. M., 2017, *MNRAS*, **465**, 885
- Savin D. W., Krstić P. S., Haiman Z., Stancil P. C., 2004, *ApJ*, **606**, L167
- Schneider I. F., Dulieu O., Giusti-Suzor A., Roueff E., 1994, *ApJ*, **424**, 983
- Sidhu K. S., Miller S., Tennyson J., 1992, *A&A*, **255**, 453
- Singh P. D., Sanzovo G. C., Borin A. C., Ornellas F. R., 1999, *MNRAS*, **303**, 235
- Slack M. W., 1976, *J. Chem. Phys.*, **64**, 228
- Smith D., Adams N. G., 1977, *International Journal of Mass Spectrometry and Ion Processes*, **23**, 123
- Smith D., Spanel P., Mayhew C. A., 1992, *International Journal of Mass Spectrometry and Ion Processes*, **117**, 457
- Smith M. A., Schlemmer S., von Richthofen J., Gerlich D., 2002, *ApJ*, **578**, L87
- Smith I. W. M., Herbst E., Chang Q., 2004, *MNRAS*, **350**, 323
- Stancil P. C., Dalgarno A., 1998, *Faraday Discussions*, **109**, 61
- Stancil P. C., et al., 1998, *ApJ*, **502**, 1006
- Stancil P. C., Schultz D. R., Kimura M., Gu J.-P., Hirsch G., Buenker R. J., 1999, *A&AS*, **140**, 225
- Stenrup M., Larson Å., Elander N., 2009, *Phys. Rev. A*, **79**, 012713
- Sternberg A., Dalgarno A., 1995, *ApJS*, **99**, 565
- Takagi H., Kosugi N., Dourneuf M. L., 1991, *Journal of Physics B: Atomic, Molecular and Optical Physics*, **24**, 711
- Tan J. C., Beltrán M. T., Caselli P., Fontani F., Fuente A., Krumholz M. R., McKee C. F., Stolte A., 2014, *Protostars and Planets VI*, pp 149–172
- Teyssier R., 2002, *A&A*, **385**, 337
- Tielens A. G. G. M., 2010, *The Physics and Chemistry of the Interstellar Medium*. Cambridge University Press
- Tsang W., Hampson R. F., 1986a, *Journal of Physical and Chemical Reference Data*, **15**, 1087
- Tsang W., Hampson R. F., 1986b, *Journal of Physical and Chemical Reference Data*, **15**, 1087
- Turk M. J., Smith B. D., Oishi J. S., Skory S., Skillman S. W., Abel T., Norman M. L., 2011, *The Astrophysical Journal Supplement Series*, **192**, 9
- Valdivia V., Hennebelle P., 2014, *A&A*, **571**, A46
- Vaytet N., Haugbølle T., 2017, *A&A*, **598**, A116
- Verner D. A., Ferland G. J., 1996, *ApJS*, **103**, 467
- Verner D. A., Ferland G. J., Korista K. T., Yakovlev D. G., 1996, *ApJ*, **465**, 487
- Viggiano A. A., Albritton D. L., Fehsenfeld F. C., Adams N. G., Smith D., Howorka F., 1980, *ApJ*, **236**, 492
- Visser R., van Dishoeck E. F., Black J. H., 2009, *A&A*, **503**, 323
- Voronov G. S., 1997, *Atomic Data and Nuclear Data Tables*, **65**, 1
- Wakelam V., et al., 2012, *ApJS*, **199**, 21
- Walch S., et al., 2015, *MNRAS*, **454**, 238
- Walkauskas L., Kaufman F., 1975, *Symposium (International) on Combustion*, **15**, 691
- Warnatz J., 1984, *Rate Coefficients in the C/H/O System*. Springer US, New York, NY, pp 197–360, doi:10.1007/978-1-4684-0186-8\_5, https://doi.org/10.1007/978-1-4684-0186-8\_5
- Wiersma R. P. C., Schaye J., Smith B. D., 2009, *MNRAS*, **393**, 99
- Wise J. H., Abel T., 2011, *MNRAS*, **414**, 3458
- Woodall J., Agúndez M., Markwick-Kemper A. J., Millar T. J., 2007, *A&A*, **466**, 1197
- Yoshida N., Omukai K., Hernquist L., Abel T., 2006, *ApJ*, **652**, 6
- Zhao L. B., et al., 2004, *ApJ*, **615**, 1063
- van Dishoeck E. F., 1987, in Vardya M. S., Tarafdar S. P., eds, *IAU Symposium Vol. 120, Astrochemistry*. pp 51–63
- van Dishoeck E. F., Jonkheid B., van Hemert M. C., 2006, *Faraday Discussions*, **133**, 231
- van de Hulst H. C., 1987, *A&A*, **173**, 115

## APPENDIX A: CHEMICAL NETWORK IN TEST 4 AND TEST 5

This paper has been typeset from a  $\text{\TeX}/\text{\LaTeX}$  file prepared by the author.

**Table A1.** Chemical network in Test 4

No.	Reaction	Rate coefficient	Notes	Ref.
1	$\text{H} + \text{e}^- \rightarrow \text{H}^+ + \text{e}^- + \text{e}^-$	$k_1 = \exp\left(-32.71396 + 13.53655 \ln(T_e) - 5.73932 \ln(T_e)^2 + 1.56315 \ln(T_e)^3 - 0.28770 \ln(T_e)^4 + 0.03482 \ln(T_e)^5 - 0.00263 \ln(T_e)^6 + 0.00011 \ln(T_e)^7 - 2.03914 \times 10^{-6} \ln(T_e)^8\right)$		1
2	$\text{H}^+ + \text{e}^- \rightarrow \text{H} + \gamma$	$k_2 = 3.92 \times 10^{-13} T_e^{-0.6353} = \exp\left(-28.61303 - 0.72411 \ln(T_e) - 0.02026 \ln(T_e)^2 - 0.00238 \ln(T_e)^3 - 0.00032 \ln(T_e)^4 - 1.42150 \times 10^{-5} \ln(T_e)^5 + 4.98910 \times 10^{-6} \ln(T_e)^6 + 5.75561 \times 10^{-7} \ln(T_e)^7 - 1.85676 \times 10^{-8} \ln(T_e)^8 - 3.07113 \times 10^{-9} \ln(T_e)^9\right)$	$2.73 < T \leq 5500 \text{ K}$ $5500 < T < 10^8 \text{ K}$	2
3	$\text{He} + \text{e}^- \rightarrow \text{He}^+ + \text{e}^- + \text{e}^-$	$k_3 = \exp\left(-44.09864 + 23.91596 \ln(T_e) - 10.75323 \ln(T_e)^2 + 3.05803 \ln(T_e)^3 - 0.56851 \ln(T_e)^4 + 0.06795 \ln(T_e)^5 - 0.00500 \ln(T_e)^6 + 0.00020 \ln(T_e)^7 - 3.64916 \times 10^{-6} \ln(T_e)^8\right)$		1
4	$\text{He}^+ + \text{e}^- \rightarrow \text{He} + \gamma$	$k_4 = 3.92 \times 10^{-13} T_e^{-0.6353} = 1.54 \times 10^{-9} \left(1 + 0.3 \exp\left(-\frac{8.09932}{T_e}\right)\right) \times \exp\left(-\frac{40.49664}{T_e}\right) T_e^{-1.5} + 3.92 \times 10^{-13} T_e^{-0.6353}$	$2.73 < T \leq 9280 \text{ K}$ $9280 < T < 10^8 \text{ K}$	3
5	$\text{He}^+ + \text{e}^- \rightarrow \text{He}^{++} + \text{e}^- + \text{e}^-$	$k_5 = \exp\left(-68.71040 + 43.93347 \ln(T_e) - 18.48066 \ln(T_e)^2 + 4.70162 \ln(T_e)^3 - 0.76924 \ln(T_e)^4 + 0.08113 \ln(T_e)^5 - 0.00532 \ln(T_e)^6 + 0.00019 \ln(T_e)^7 - 3.16558 \times 10^{-6} \ln(T_e)^8\right)$		4
6	$\text{He}^+ + \text{H} \rightarrow \text{He} + \text{H}^+$	$k_6 = 3 \times 10^{-16} (T/300)$		5
7	$\text{He} + \text{H}^+ \rightarrow \text{He}^+ + \text{H}$	$k_7 = 1.26 \times 10^{-9} T^{-0.75} \exp\left(-\frac{127500}{T}\right) = 4 \times 10^{-37} T^{4.74}$	$T < 10^4 \text{ K}$ $T > 10^4 \text{ K}$	6
8	$\text{H}_2 + \text{He} \rightarrow \text{H} + \text{H} + \text{He}$	$k_8 = k_{\text{h,He}}^{(1-a_{\text{He}})} k_{\text{l,He}}^{a_{\text{He}}}$		88

Table A1 – continued

No.	Reaction	Rate coefficient	Notes	Ref.
9	$\text{H}_2 + \text{He}^+ \rightarrow \text{He} + \text{H}_2^+$	$k_9 = 7.2 \times 10^{-15}$		8
10	$\text{H}_2 + \text{He}^+ \rightarrow \text{He} + \text{H} + \text{H}^+$	$k_{10} = 3.7 \times 10^{-14} \exp\left(-\frac{35}{T}\right)$		8
11	$\text{H}_2 + \text{He}^+ \rightarrow \text{He}^+ + \text{H} + \text{H}$	$k_{11} = 3 \times 10^{-11} \sqrt{(T/300)} \exp\left(-\frac{52000}{T}\right)$		9
12	$\text{He}^{++} + \text{e}^- \rightarrow \text{He}^+ + \gamma$	$k_{12} = \frac{1.891 \times 10^{-10}}{\sqrt{\frac{T}{9.37}} \left(1 + \sqrt{\frac{T}{9.37}}\right)^{0.2476} \left(1 + \sqrt{\frac{T}{2774000}}\right)^{1.7524}}$		10
13	$\text{H} + \text{e}^- \rightarrow \text{H}^- + \gamma$	$k_{13} = 1.4 \times 10^{-18} T^{0.928} \exp\left(-\frac{T}{16200}\right)$		10
14	$\text{H}^- + \text{H} \rightarrow \text{H}_2 + \text{e}^-$	$k_{14} = \frac{1.35 \times 10^{-9} \left(T^{0.09849} + 0.32852 T^{0.5561} + 2.771 \times 10^{-7} T^{2.1826}\right)}{1 + 0.00619 T^{1.0461} + 8.9712 \times 10^{-11} T^{3.0424} + 3.2576 \times 10^{-14} T^{3.7741}}$		11
15	$\text{H} + \text{H}^+ \rightarrow \text{H}_2^+ + \gamma$	$k_{15} = 2.1 \times 10^{-20} (T/30)^{-0.15}$	$T < 30 \text{ K}$ $T \geq 30 \text{ K}$	12
16	$\text{H}_2^+ + \text{H} \rightarrow \text{H}_2 + \text{H}^+$	$k_{16} = 6 \times 10^{-10}$		13
17	$\text{H}_2 + \text{H}^+ \rightarrow \text{H}_2^+ + \text{H}$	$k_{17} = 10^{\left(-8875.5774 + 10081.246 \log(T) - 4860.6622 \log(T)^2 + 1288.9659 \log(T)^3 - 203.19575 \log(T)^4 + 19.05749 \log(T)^5 - 0.98530 \log(T)^6 + 0.02167 \log(T)^7\right)}$	$T \geq 10^5 \text{ K}$	14
18	$\text{H}_2 + \text{e}^- \rightarrow \text{H} + \text{H} + \text{e}^-$	$k_{18} = 4.38 \times 10^{-10} \exp\left(-\frac{102000}{T}\right) T^{0.35}$		15
19	$\text{H}_2 + \text{H} \rightarrow \text{H} + \text{H} + \text{H}$	$k_{19} = 10^{\left(\log(k_{h,H}) - \frac{\log(k_{h,H}) - \log(k_{1,H})}{1 + \frac{n_{\text{Hrot}}}{n_{\text{cr,H}}}}\right)}$		16
20	$\text{H}^- + \text{e}^- \rightarrow \text{H} + \text{e}^- + \text{e}^-$	$k_{20} = \exp\left(-18.01849 + 2.36085 \ln(T_e) - 0.28274 \ln(T_e)^2 + 0.01623 \ln(T_e)^3 - 0.03365 \ln(T_e)^4 + 0.01178 \ln(T_e)^5 - 0.00165 \ln(T_e)^6 + 0.00010 \ln(T_e)^7 - 2.63128 \times 10^{-6} \ln(T_e)^8\right)$		1
21	$\text{H}^- + \text{H} \rightarrow \text{H} + \text{H} + \text{e}^-$	$k_{21} = 2.56 \times 10^{-9} T_e^{1.78186}$ $= \exp\left(-20.37260 + 1.13944 \ln(T_e) - 0.14210 \ln(T_e)^2 + 0.00846 \ln(T_e)^3 - 0.00143 \ln(T_e)^4 + 0.00020 \ln(T_e)^5 + 8.66396 \times 10^{-5} \ln(T_e)^6 - 2.58500 \times 10^{-5} \ln(T_e)^7 + 2.45550 \times 10^{-6} \ln(T_e)^8 - 8.06838 \times 10^{-8} \ln(T_e)^9\right)$	$T \leq 1160 \text{ K}$ $T > 1160 \text{ K}$	17
22	$\text{H}^- + \text{H}^+ \rightarrow \text{H} + \text{H}$	$k_{22} = \frac{2.96 \times 10^{-6}}{\sqrt{T}} - 1.73 \times 10^{-9} + 2.5 \times 10^{-10} \sqrt{T}$		18
23	$\text{H}^- + \text{H}^+ \rightarrow \text{H}_2^+ + \text{e}^-$	$k_{23} = 10^{-8} T^{-0.4}$		19
24	$\text{H}_2^+ + \text{e}^- \rightarrow \text{H} + \text{H}$	$k_{24} = 10^{-8}$ $= 1.32 \times 10^{-6} T^{-0.76}$	$T \leq 617 \text{ K}$ $T > 617 \text{ K}$	20
25	$\text{H}_2^+ + \text{H}^- \rightarrow \text{H} + \text{H}_2$	$k_{25} = 5 \times 10^{-7} \sqrt{\frac{100}{T}}$		21

**Table A1** – *continued*

No.	Reaction	Rate coefficient	Notes	Ref.
26	$\text{H}_2 + \text{H}_2 \rightarrow \text{H}_2 + \text{H} + \text{H}$	$k_{26} = 10^{\left(\log(k_{\text{h,H}_2}) - \frac{\log(k_{\text{h,H}_2}) - \log(k_{1,\text{H}_2})}{1 + \frac{n_{\text{Htot}}}{n_{\text{crit,H}_2}}}\right)}$		16
27	$\text{H} + \text{H} + \text{He} \rightarrow \text{H}_2 + \text{He}$	$k_{27} = 6.9 \times 10^{-32} T^{-0.4}$		55
28	$\text{H} + \text{H} + \text{H} \rightarrow \text{H}_2 + \text{H}$	$k_{28} = 6 \times 10^{-32} T^{-0.25} + 2 \times 10^{-31} T^{-0.5}$		23
29	$\text{H}_2 + \text{H} + \text{H} \rightarrow \text{H}_2 + \text{H}_2$	$k_{29} = 7.5 \times 10^{-33} T^{-0.25} + 2.5 \times 10^{-32} T^{-0.5}$		24
30	$\text{C}^+ + \text{e}^- \rightarrow \text{C} + \gamma$	$k_{30} = 4.67 \times 10^{-12} (T/300)^{-0.6}$ $= 1.23 \times 10^{-17} (T/300)^{2.49} \exp\left(\frac{21845.6}{T}\right)$ $= 9.62 \times 10^{-8} (T/300)^{-1.37} \exp\left(-\frac{115786.2}{T}\right)$	$T \leq 7950 \text{ K}$ $7950 < T \leq 21\,140 \text{ K}$ $T > 21\,140 \text{ K}$	25
31	$\text{O}^+ + \text{e}^- \rightarrow \text{O} + \gamma$	$k_{31} = 1.3 \times 10^{-10} T^{-0.64}$ $= 1.41 \times 10^{-10} T^{-0.66}$ $+ 0.00074 T^{-1.5} \exp\left(-\frac{175000}{T}\right)$ $\times \left(1 + 0.062 \exp\left(-\frac{145000}{T}\right)\right)$ $6.85 \times 10^{-8} \left(\frac{11.26}{T_e}\right)^{0.25} \exp\left(-\frac{11.26}{T_e}\right)$	$T \leq 400 \text{ K}$ $T > 400 \text{ K}$	26
32	$\text{C} + \text{e}^- \rightarrow \text{C}^+ + \text{e}^- + \text{e}^-$	$k_{32} = \frac{3.59 \times 10^{-8} \left(\frac{13.6}{T_e}\right)^{0.34} \exp\left(-\frac{13.6}{T_e}\right)}{0.193 + 11.26/T_e}$		27
33	$\text{O} + \text{e}^- \rightarrow \text{O}^+ + \text{e}^- + \text{e}^-$	$k_{33} = \frac{0.073 + 13.6/T_e}{0.073 + 13.6/T_e}$		27
34	$\text{O}^+ + \text{H} \rightarrow \text{O} + \text{H}^+$	$k_{34} = 4.99 \times 10^{-11} T^{0.405} + 7.54 \times 10^{-10} T^{-0.458}$		28
35	$\text{O} + \text{H}^+ \rightarrow \text{O}^+ + \text{H}$	$k_{35} = \left(1.08 \times 10^{-11} T^{0.517}\right.$ $\left.+ 4 \times 10^{-10} T^{0.00669}\right) \exp\left(-\frac{227}{T}\right)$		29
36	$\text{O} + \text{He}^+ \rightarrow \text{O}^+ + \text{He}$	$k_{36} = 4.991 \times 10^{-15} \left(\frac{T}{10000}\right)^{0.3794} \exp\left(-8.9206 \times 10^{-7} T\right)$ $+ 2.78 \times 10^{-15} \left(\frac{T}{10000}\right)^{-0.2163} \exp\left(-1.2258 \times 10^{-6} T\right)$		30
37	$\text{C} + \text{H}^+ \rightarrow \text{C}^+ + \text{H}$	$k_{37} = 3.9 \times 10^{-16} T^{0.213}$		29
38	$\text{C}^+ + \text{H} \rightarrow \text{C} + \text{H}^+$	$k_{38} = 6.08 \times 10^{-14} \left(\frac{T}{10000}\right)^{1.96} \exp\left(-\frac{170000}{T}\right)$		29
39	$\text{C} + \text{He}^+ \rightarrow \text{C}^+ + \text{He}$	$k_{39} = 8.58 \times 10^{-17} T^{0.757}$ $= 3.25 \times 10^{-17} T^{0.968}$ $= 2.77 \times 10^{-19} T^{1.597}$	$T \leq 200 \text{ K}$ $200 < T \leq 2000 \text{ K}$ $2000 < T < 10^8 \text{ K}$	31
40	$\text{OH} + \text{H} \rightarrow \text{O} + \text{H} + \text{H}$	$k_{40} = 6 \times 10^{-9} \exp\left(-\frac{50900}{T}\right)$		32
41	$\text{HOC}^+ + \text{H}_2 \rightarrow \text{HCO}^+ + \text{H}_2$	$k_{41} = 3.8 \times 10^{-10}$		33
42	$\text{HOC}^+ + \text{CO} \rightarrow \text{HCO}^+ + \text{CO}$	$k_{42} = 1.604 \times 10^{-9}$ $= 8.68 \times 10^{-10} \left(1 + 0.02427 \sqrt{\frac{300}{T} + \frac{7.1537}{T}}\right)$	$T < 10 \text{ K}$ $T > 10 \text{ K}$	34
43	$\text{C} + \text{H}_2 \rightarrow \text{CH} + \text{H}$	$k_{43} = 6.64 \times 10^{-10} \exp\left(-\frac{11700}{T}\right)$		35
44	$\text{CH} + \text{H} \rightarrow \text{C} + \text{H}_2$	$k_{44} = 1.31 \times 10^{-10} \exp\left(-\frac{80}{T}\right)$		36
45	$\text{CH} + \text{H}_2 \rightarrow \text{CH}_2 + \text{H}$	$k_{45} = 5.46 \times 10^{-10} \exp\left(-\frac{1943}{T}\right)$		32
46	$\text{CH} + \text{C} \rightarrow \text{C}_2 + \text{H}$	$k_{46} = 2.4 \times 10^{-10}$		37
47	$\text{CH} + \text{O} \rightarrow \text{CO} + \text{H}$	$k_{47} = 1.02 \times 10^{-10} \exp\left(-\frac{914}{T}\right)$		38
48	$\text{CH} + \text{O} \rightarrow \text{HCO}^+ + \text{e}^-$	$k_{48} = 1.9 \times 10^{-11} (T/300)^{-2.2} \exp\left(-\frac{165.1}{T}\right)$		39
49	$\text{CH} + \text{O} \rightarrow \text{OH} + \text{C}$	$k_{49} = 2.52 \times 10^{-11} \exp\left(-\frac{2381}{T}\right)$		39
50	$\text{CH}_2 + \text{H} \rightarrow \text{CH} + \text{H}_2$	$k_{50} = 2.2 \times 10^{-10}$		40
51	$\text{CH}_2 + \text{O} \rightarrow \text{CO} + \text{H} + \text{H}$	$k_{51} = 2.04 \times 10^{-10} \exp\left(-\frac{270}{T}\right)$		40
52	$\text{CH}_2 + \text{O} \rightarrow \text{CO} + \text{H}_2$	$k_{52} = 1.36 \times 10^{-10} \exp\left(-\frac{270}{T}\right)$		40
53	$\text{CH}_2 + \text{O} \rightarrow \text{HCO} + \text{H}$	$k_{53} = 5.01 \times 10^{-11}$		40
54	$\text{CH}_2 + \text{O} \rightarrow \text{CH} + \text{OH}$	$k_{54} = 4.98 \times 10^{-10} \exp\left(-\frac{6000}{T}\right)$		40
55	$\text{C}_2 + \text{O} \rightarrow \text{CO} + \text{C}$	$k_{55} = 2 \times 10^{-12} (T/300)^{-0.12}$ $= 2 \times 10^{-12} (T/300)^{0.757}$	$T < 300 \text{ K}$ $T > 300 \text{ K}$	40
56	$\text{O} + \text{H}_2 \rightarrow \text{OH} + \text{H}$	$k_{56} = 1.46 \times 10^{-12} \exp\left(-\frac{9650}{T}\right)$		40
57	$\text{OH} + \text{H} \rightarrow \text{O} + \text{H}_2$	$k_{57} = 6.99 \times 10^{-14} (T/300)^{2.8} \exp\left(-\frac{1950}{T}\right)$ $= 5.45 \times 10^{-17}$	$T < 280 \text{ K}$ $T > 280 \text{ K}$	56
58	$\text{H}_2 + \text{OH} \rightarrow \text{H}_2\text{O} + \text{H}$	$k_{58} = 3.6 \times 10^{-16} T^{1.52} \exp\left(-\frac{1740}{T}\right)$		41

Table A1 – continued

No.	Reaction	Rate coefficient	Notes	Ref.
59	$C + OH \rightarrow H + CO$	$k_{59} = 7.051 \times 10^{-11}$ $= 2.25 \times 10^{-11} (T/300)^{-0.339} \exp\left(-\frac{0.108}{T}\right)$	$T < 10$ K $T > 10$ K	40
60	$O + OH \rightarrow H + O_2$	$k_{60} = 2.4 \times 10^{-11} \exp\left(\frac{110}{T}\right)$ $= 4.997 \times 10^{-11}$	$T > 150$ K $T < 150$ K	40
61	$OH + OH \rightarrow H_2O + O$	$k_{61} = 1.65 \times 10^{-12} (T/300)^{1.14} \exp\left(-\frac{50}{T}\right)$		57
62	$H_2O + H \rightarrow H_2 + OH$	$k_{62} = 1.59 \times 10^{-11} (T/300) \times 1.2 \exp\left(-\frac{9610}{T}\right)$		58
63	$O_2 + H \rightarrow OH + O$	$k_{63} = 3.13 \times 10^{-10} \exp\left(-\frac{8156}{T}\right)$		22
64	$O_2 + H_2 \rightarrow OH + OH$	$k_{64} = 3.16 \times 10^{-10} \exp\left(-\frac{21890}{T}\right)$		59
65	$O_2 + C \rightarrow CO + O$	$k_{65} = 4.7 \times 10^{-11} (T/300)^{-0.34}$ $= 2.48 \times 10^{-12} (T/300)^{1.54} \exp\left(\frac{613}{T}\right)$	$T < 1052$ K $T > 1052$ K	57 22
66	$CO + H \rightarrow C + OH$	$k_{66} = 1.1 \times 10^{-10} (T/300)^{0.5} \exp\left(-\frac{77700}{T}\right)$		32
67	$H_2^+ + H_2 \rightarrow H_3^+ + H$	$k_{67} = 2.24 \times 10^{-9} (T/300)^{0.042} \exp\left(-\frac{T}{46600}\right)$		60
68	$H_3^+ + H \rightarrow H_2^+ + H_2$	$k_{68} = 7.7 \times 10^{-9} \exp\left(-\frac{17560}{T}\right)$		61
69	$C + H_2^+ \rightarrow CH^+ + H$	$k_{69} = 2.4 \times 10^{-9}$		32
70	$C + H_3^+ \rightarrow CH^+ + H_2$	$k_{70} = \frac{1.0218 \times 10^{-9} + 7.2733 \times 10^{-11} \sqrt{T} + 5.9203 \times 10^{-14} T}{T^{0.1667} + 0.04491 \sqrt{T} - 5.9203 \times 10^{-14} T + 2.6397 \times 10^{-6} T^{1.5}}$ $8.5145 \times 10^{-10}$		42
71	$C + H_3^+ \rightarrow CH_2^+ + H$	$k_{71} = \frac{1.0218 \times 10^{-9} + 7.2733 \times 10^{-11} \sqrt{T} + 5.9203 \times 10^{-14} T}{T^{0.1667} + 0.00095 \sqrt{T} - 4.404 \times 10^{-5} T + 2.3496 \times 10^{-6} T^{1.5}}$		42
72	$C^+ + H_2 \rightarrow CH^+ + H$	$k_{72} = 10^{-10} \exp\left(-\frac{4640}{T}\right)$		62
73	$CH^+ + H \rightarrow C^+ + H_2$	$k_{73} = 7.5 \times 10^{-10}$		63
74	$CH^+ + H_2 \rightarrow CH_2^+ + H$	$k_{74} = 1.2 \times 10^{-9}$		63
75	$CH^+ + O \rightarrow CO^+ + H$	$k_{75} = 3.5 \times 10^{-10}$		64
76	$CH_2^+ + H \rightarrow CH^+ + H_2$	$k_{76} = 10^{-9} \exp\left(-\frac{7080}{T}\right)$		64
77	$CH_2^+ + H_2 \rightarrow CH_3^+ + H$	$k_{77} = 1.6 \times 10^{-9}$		65
78	$CH_2^+ + O \rightarrow HCO^+ + H$	$k_{78} = 7.5 \times 10^{-10}$		64
79	$CH_3^+ + H \rightarrow CH_2^+ + H_2$	$k_{79} = 7 \times 10^{-10} \exp\left(-\frac{10560}{T}\right)$		64
80	$CH_3^+ + O \rightarrow HOC^+ + H_2$	$k_{80} = 2.5 \times 10^{-10}$		40
81	$CH_3^+ + O \rightarrow HCO^+ + H_2$	$k_{81} = 2.5 \times 10^{-10}$		40
82	$C_2 + O^+ \rightarrow CO^+ + C$	$k_{82} = 4.8 \times 10^{-10}$		40
83	$O^+ + H_2 \rightarrow H + OH^+$	$k_{83} = 1.69 \times 10^{-9}$		40
84	$O + H_2^+ \rightarrow H + OH^+$	$k_{84} = 1.5 \times 10^{-9}$		64
85	$O + H_3^+ \rightarrow H_2 + OH^+$	$k_{85} = 7.98 \times 10^{-10} (T/300)^{-0.156} \exp\left(-\frac{1.41}{T}\right)$		40
86	$O + H_3^+ \rightarrow H + H_2O^+$	$k_{86} = 3.42 \times 10^{-10} (T/300)^{-0.156} \exp\left(-\frac{1.41}{T}\right)$		40
87	$OH + H_3^+ \rightarrow H_2 + H_2O^+$	$k_{87} = 2.277 \times 10^{-8}$ $= 1.52 \times 10^{-9} (0.62 + 2.62185 (T/300)^{-0.5})$	$T < 10$ K $T > 10$ K	40
88	$OH + C^+ \rightarrow H + CO^+$	$k_{88} = 1.371 \times 10^{-8}$ $= 9.15 \times 10^{-10} (0.62 + 2.62185 (T/300)^{-0.5})$	$T < 10$ K $T > 10$ K	40
89	$OH^+ + H_2 \rightarrow H_2O^+ + H$	$k_{89} = 1.01 \times 10^{-9}$		66
90	$H_2O^+ + H_2 \rightarrow H_3O^+ + H$	$k_{90} = 6.4 \times 10^{-10}$		67
91	$H_2O + H_3^+ \rightarrow H_2 + H_3O^+$	$k_{91} = 2.55 \times 10^{-8}$ $= 1.73 \times 10^{-9} (0.62 + 2.57894 (T/300)^{-0.5})$	$T < 10$ K $T > 10$ K	40
92	$H_2O + C^+ \rightarrow HOC^+ + H$	$k_{92} = 1.8 \times 10^{-9}$		40
93	$H_2O + C^+ \rightarrow HCO^+ + H$	$k_{93} = 5.027 \times 10^{-9}$ $= 3.4093 \times 10^{-10} (0.62 + 2.57894 (T/300)^{-0.5})$	$T < 10$ K $T > 10$ K	40
94	$H_2O + C^+ \rightarrow H_2O^+ + C$	$k_{94} = 2.4 \times 10^{-10}$		40
95	$H_3O^+ + C \rightarrow HCO^+ + H_2$	$k_{95} = 10^{-11}$		64
96	$O_2 + C^+ \rightarrow CO^+ + O$	$k_{96} = 3.42 \times 10^{-10}$		40
97	$O_2 + C^+ \rightarrow CO + O^+$	$k_{97} = 4.53 \times 10^{-10}$		40
98	$O_2 + CH_2^+ \rightarrow HCO^+ + OH$	$k_{98} = 9.1 \times 10^{-10}$		65
99	$C + O_2^+ \rightarrow O + CO^+$	$k_{99} = 5.2 \times 10^{-11}$		32
100	$C + O_2^+ \rightarrow O_2 + C^+$	$k_{100} = 5.2 \times 10^{-11}$		40

**Table A1** – *continued*

No.	Reaction	Rate coefficient	Notes	Ref.
101	$\text{CO} + \text{H}_3^+ \rightarrow \text{H}_2 + \text{HCO}^+$	$k_{101} = 2.468 \times 10^{-9}$ $= 1.88055 \times 10^{-9} \left(1 + 0.02427 (T/300)^{-0.5} + \frac{1.79558}{T}\right)$	$T < 10 \text{ K}$ $T > 10 \text{ K}$	40
102	$\text{CO} + \text{H}_3^+ \rightarrow \text{H}_2 + \text{HOC}^+$	$k_{102} = 1.421 \times 10^{-10}$ $= 1.08256 \times 10^{-10} \left(1 + 0.02427 (T/300)^{-0.5} + \frac{1.79558}{T}\right)$	$T < 10 \text{ K}$ $T > 10 \text{ K}$	40
103	$\text{HCO}^+ + \text{C} \rightarrow \text{CO} + \text{CH}^+$	$k_{103} = 1.1 \times 10^{-9}$		40
104	$\text{HCO}^+ + \text{H}_2\text{O} \rightarrow \text{CO} + \text{H}_3\text{O}^+$	$k_{104} = 7.279 \times 10^{-8}$ $= 8.34 \times 10^{-10} \left(1 + 0.5232 (T/300)^{-0.5} + \frac{834.16588}{T}\right)$	$T < 10 \text{ K}$ $T > 10 \text{ K}$	40
105	$\text{CH} + \text{H}^+ \rightarrow \text{CH}^+ + \text{H}$	$k_{105} = 3.297 \times 10^{-8}$ $= 3.54 \times 10^{-9} \left(0.62 + 1.58741 (T/300)^{-0.5}\right)$	$T < 10 \text{ K}$ $T > 10 \text{ K}$	40
106	$\text{CH}_2 + \text{H}^+ \rightarrow \text{H}_2 + \text{CH}^+$	$k_{106} = 1.765 \times 10^{-9} \left(0.62 + 0.67214 (T/300)^{-0.5}\right)$ $= 1.765 \times 10^{-9} \left(1 + 0.13634 (T/300)^{-0.5} + \frac{56.66255}{T}\right)$	$T < 150 \text{ K}$ $T > 150 \text{ K}$	40
107	$\text{CH}_2 + \text{H}^+ \rightarrow \text{H} + \text{CH}_2^+$	$k_{107} = 1.765 \times 10^{-9} \left(0.62 + 0.67214 (T/300)^{-0.5}\right)$ $= 1.765 \times 10^{-9} \left(1 + 0.13634 (T/300)^{-0.5} + \frac{56.66255}{T}\right)$	$T < 150 \text{ K}$ $T > 150 \text{ K}$	40
108	$\text{CH}_2 + \text{He}^+ \rightarrow \text{He} + \text{H}_2 + \text{C}^+$	$k_{108} = 9.65 \times 10^{-10} \left(0.62 + 0.67214 (T/300)^{-0.5}\right)$ $= 9.65 \times 10^{-10} \left(1 + 0.13634 (T/300)^{-0.5} + \frac{56.66254}{T}\right)$	$T < 150 \text{ K}$ $T > 150 \text{ K}$	40
109	$\text{CH}_2 + \text{He}^+ \rightarrow \text{He} + \text{H} + \text{CH}^+$	$k_{109} = 9.65 \times 10^{-10} \left(0.62 + 0.67214 (T/300)^{-0.5}\right)$ $= 9.65 \times 10^{-10} \left(1 + 0.13634 (T/300)^{-0.5} + \frac{56.66254}{T}\right)$	$T < 150 \text{ K}$ $T > 150 \text{ K}$	40
110	$\text{C}_2 + \text{He}^+ \rightarrow \text{C}^+ + \text{C} + \text{He}$	$k_{110} = 1.6 \times 10^{-9}$		40
111	$\text{OH} + \text{H}^+ \rightarrow \text{OH}^+ + \text{H}$	$k_{111} = 3.745 \times 10^{-8}$ $= 2.5 \times 10^{-9} \left(0.62 + 2.62185 (T/300)^{-0.5}\right)$	$T < 10 \text{ K}$ $T > 10 \text{ K}$	40
112	$\text{OH} + \text{He}^+ \rightarrow \text{O}^+ + \text{He} + \text{H}$	$k_{112} = 2.022 \times 10^{-8}$ $= 1.35 \times 10^{-9} \left(0.62 + 2.62185 (T/300)^{-0.5}\right)$	$T < 10 \text{ K}$ $T > 10 \text{ K}$	40
113	$\text{H}_2\text{O} + \text{H}^+ \rightarrow \text{H} + \text{H}_2\text{O}^+$	$k_{113} = 4.202 \times 10^{-8}$ $= 2.85 \times 10^{-9} \left(0.62 + 2.57894 (T/300)^{-0.5}\right)$	$T < 10 \text{ K}$ $T > 10 \text{ K}$	40
114	$\text{H}_2\text{O} + \text{He}^+ \rightarrow \text{He} + \text{OH} + \text{H}^+$	$k_{114} = 7.562 \times 10^{-9}$ $= 5.1282 \times 10^{-10} \left(0.62 + 2.57894 (T/300)^{-0.5}\right)$	$T < 10 \text{ K}$ $T > 10 \text{ K}$	40
115	$\text{H}_2\text{O} + \text{He}^+ \rightarrow \text{He} + \text{OH}^+ + \text{H}$	$k_{115} = 7.562 \times 10^{-9}$ $= 5.1282 \times 10^{-10} \left(0.62 + 2.57894 (T/300)^{-0.5}\right)$	$T < 10 \text{ K}$ $T > 10 \text{ K}$	40
116	$\text{H}_2\text{O} + \text{He}^+ \rightarrow \text{He} + \text{H}_2\text{O}^+$	$k_{116} = 7.56 \times 10^{-9}$ $= 5.1282 \times 10^{-10} \left(0.62 + 2.57894 (T/300)^{-0.5}\right)$	$T < 10 \text{ K}$ $T > 10 \text{ K}$	40
117	$\text{O}_2 + \text{H}^+ \rightarrow \text{O}_2^+ + \text{H}$	$k_{117} = 2 \times 10^{-9}$		68
118	$\text{O}_2 + \text{He}^+ \rightarrow \text{O}_2^+ + \text{He}$	$k_{118} = 3.3 \times 10^{-11}$		65
119	$\text{O}_2 + \text{He}^+ \rightarrow \text{O}^+ + \text{He} + \text{O}$	$k_{119} = 1.1 \times 10^{-9}$		65
120	$\text{CO} + \text{He}^+ \rightarrow \text{C}^+ + \text{He} + \text{O}$	$k_{120} = 1.4 \times 10^{-9} (T/300)^{-0.5}$		51
121	$\text{CO} + \text{He}^+ \rightarrow \text{C} + \text{He} + \text{O}^+$	$k_{121} = 1.4 \times 10^{-16} (T/300)^{-0.5}$		51
122	$\text{CO}^+ + \text{H} \rightarrow \text{CO} + \text{H}^+$	$k_{122} = 7.5 \times 10^{-10}$		69
123	$\text{C}^- + \text{H}^+ \rightarrow \text{C} + \text{H}$	$k_{123} = 2.3 \times 10^{-7} (T/300)^{-0.5}$		32
124	$\text{O}^- + \text{H}^+ \rightarrow \text{O} + \text{H}$	$k_{124} = 2.3 \times 10^{-7} (T/300)^{-0.5}$		32
125	$\text{He}^+ + \text{H}^- \rightarrow \text{H} + \text{He}$	$k_{125} = 2.3 \times 10^{-7} (T/300)^{-0.5}$		70
126	$\text{H}_3^+ + \text{e}^- \rightarrow \text{H}_2 + \text{H}$	$k_{126} = 2.34 \times 10^{-8} (T/300)^{-0.52}$		71
127	$\text{H}_3^+ + \text{e}^- \rightarrow \text{H} + \text{H} + \text{H}$	$k_{127} = 4.36 \times 10^{-8} (T/300)^{-0.52}$		71
128	$\text{CH}^+ + \text{e}^- \rightarrow \text{C} + \text{H}$	$k_{128} = 7 \times 10^{-8} (T/300)^{-0.5}$		72
129	$\text{CH}_2^+ + \text{e}^- \rightarrow \text{CH} + \text{H}$	$k_{129} = 1.6 \times 10^{-7} (T/300)^{-0.6}$		73
130	$\text{CH}_2^+ + \text{e}^- \rightarrow \text{C} + \text{H}_2$	$k_{130} = 7.68 \times 10^{-8} (T/300)^{-0.6}$		73
131	$\text{CH}_2^+ + \text{e}^- \rightarrow \text{C} + \text{H} + \text{H}$	$k_{131} = 4.03 \times 10^{-7} (T/300)^{-0.6}$		73
132	$\text{CH}_3^+ + \text{e}^- \rightarrow \text{CH}_2 + \text{H}$	$k_{132} = 7.75 \times 10^{-8} (T/300)^{-0.5}$		74
133	$\text{CH}_3^+ + \text{e}^- \rightarrow \text{CH} + \text{H}_2$	$k_{133} = 1.95 \times 10^{-7} (T/300)^{-0.5}$		74
134	$\text{CH}_3^+ + \text{e}^- \rightarrow \text{CH} + \text{H} + \text{H}$	$k_{134} = 2 \times 10^{-7} (T/300)^{-0.5}$		32
135	$\text{OH}^+ + \text{e}^- \rightarrow \text{O} + \text{H}$	$k_{135} = 6.3 \times 10^{-9} (T/300)^{-0.48}$		75
136	$\text{H}_2\text{O}^+ + \text{e}^- \rightarrow \text{O} + \text{H}_2$	$k_{136} = 3.9 \times 10^{-8} (T/300)^{-0.5}$		76
137	$\text{H}_2\text{O}^+ + \text{e}^- \rightarrow \text{OH} + \text{H}$	$k_{137} = 8.6 \times 10^{-8} (T/300)^{-0.5}$		76
138	$\text{H}_2\text{O}^+ + \text{e}^- \rightarrow \text{O} + \text{H} + \text{H}$	$k_{138} = 3.05 \times 10^{-7} (T/300)^{-0.5}$		76

Table A1 – continued

No.	Reaction	Rate coefficient	Notes	Ref.
139	$\text{H}_3\text{O}^+ + \text{e}^- \rightarrow \text{OH} + \text{H} + \text{H}$	$k_{139} = 2.58 \times 10^{-7} (T/300)^{-0.5}$		77
140	$\text{H}_3\text{O}^+ + \text{e}^- \rightarrow \text{O} + \text{H} + \text{H}_2$	$k_{140} = 5.6 \times 10^{-9} (T/300)^{-0.5}$		77
141	$\text{H}_3\text{O}^+ + \text{e}^- \rightarrow \text{H} + \text{H}_2\text{O}$	$k_{141} = 1.08 \times 10^{-7} (T/300)^{-0.5}$		77
142	$\text{H}_3\text{O}^+ + \text{e}^- \rightarrow \text{OH} + \text{H}_2$	$k_{142} = 6.02 \times 10^{-8} (T/300)^{-0.5}$		77
143	$\text{O}_2^+ + \text{e}^- \rightarrow \text{O} + \text{O}$	$k_{143} = 1.95 \times 10^{-7} (T/300)^{-0.7}$		78
144	$\text{CO}^+ + \text{e}^- \rightarrow \text{C} + \text{O}$	$k_{144} = 2.75 \times 10^{-7} (T/300)^{-0.55}$		79
145	$\text{HCO}^+ + \text{e}^- \rightarrow \text{CO} + \text{H}$	$k_{145} = 2.76 \times 10^{-7} (T/300)^{-0.64}$		80
146	$\text{HCO}^+ + \text{e}^- \rightarrow \text{OH} + \text{C}$	$k_{146} = 2.4 \times 10^{-8} (T/300)^{-0.64}$		80
147	$\text{HOC}^+ + \text{e}^- \rightarrow \text{CO} + \text{H}$	$k_{147} = 1.1 \times 10^{-7} (T/300)^{-1}$		32
148	$\text{H}^- + \text{C} \rightarrow \text{CH} + \text{e}^-$	$k_{148} = 10^{-9}$		32
149	$\text{H}^- + \text{O} \rightarrow \text{OH} + \text{e}^-$	$k_{149} = 10^{-10}$		32
150	$\text{H}^- + \text{OH} \rightarrow \text{H}_2\text{O} + \text{e}^-$	$k_{150} = 5 \times 10^{-10}$		32
151	$\text{C}^- + \text{H} \rightarrow \text{CH} + \text{e}^-$	$k_{151} = 10^{-13}$		32
152	$\text{C}^- + \text{H}_2 \rightarrow \text{CH}_2 + \text{e}^-$	$k_{152} = 5 \times 10^{-10}$		32
153	$\text{C}^- + \text{O} \rightarrow \text{CO} + \text{e}^-$	$k_{153} = 5 \times 10^{-10}$		32
154	$\text{O}^- + \text{H} \rightarrow \text{OH} + \text{e}^-$	$k_{154} = 7 \times 10^{-10}$		32
155	$\text{O}^- + \text{H}_2 \rightarrow \text{H}_2\text{O} + \text{e}^-$	$k_{155} = 7 \times 10^{-10}$		32
156	$\text{O}^- + \text{C} \rightarrow \text{CO} + \text{e}^-$	$k_{156} = 5 \times 10^{-10}$		32
157	$\text{H}_2 + \text{H}^+ \rightarrow \text{H} + \text{H} + \text{H}^+$	$k_{157} = 3 \times 10^{-11} (T/300)^{0.5} \exp\left(-\frac{52000}{T}\right)$		22
158	$\text{H}_2 + \text{H}^+ \rightarrow \text{H}_3^+ + \gamma$	$k_{158} = 10^{-16}$		81
159	$\text{C} + \text{e}^- \rightarrow \text{C}^- + \gamma$	$k_{159} = 2.25 \times 10^{-15}$		82
160	$\text{C} + \text{H} \rightarrow \text{CH} + \gamma$	$k_{160} = 10^{-17}$		83
161	$\text{C} + \text{H}_2 \rightarrow \text{CH}_2 + \gamma$	$k_{161} = 10^{-17}$		83
162	$\text{C} + \text{C} \rightarrow \text{C}_2 + \gamma$	$k_{162} = 4.36 \times 10^{-18} (T/300)^{0.35} \exp\left(-\frac{161.3}{T}\right)$		84
163	$\text{C} + \text{O} \rightarrow \text{CO} + \gamma$	$k_{163} = 3.09 \times 10^{-17} (T/300)^{0.33} \exp\left(-\frac{1629}{T}\right)$		85
164	$\text{C}^+ + \text{H} \rightarrow \text{CH}^+ + \gamma$	$k_{164} = 4.46 \times 10^{-16} T^{-0.5} \exp\left(-4.93 T^{-0.6667}\right)$		86
165	$\text{C}^+ + \text{H}_2 \rightarrow \text{CH}_2^+ + \gamma$	$k_{165} = 2 \times 10^{-16} (T/300)^{-1.3} \exp\left(-\frac{23}{T}\right)$		40
166	$\text{C}^+ + \text{O} \rightarrow \text{CO}^+ + \gamma$	$k_{166} = 2.5 \times 10^{-18}$ $= 3.14 \times 10^{-18} (T/300)^{-0.15} \exp\left(-\frac{68}{T}\right)$	$T < 300 \text{ K}$ $T > 300 \text{ K}$	40
167	$\text{O} + \text{e}^- \rightarrow \text{O}^- + \gamma$	$k_{167} = 1.5 \times 10^{-15}$		40
168	$\text{O} + \text{H} \rightarrow \text{OH} + \gamma$	$k_{168} = 9.9 \times 10^{-19} (T/300)^{-0.38}$		40
169	$\text{O} + \text{O} \rightarrow \text{O}_2 + \gamma$	$k_{169} = 4.9 \times 10^{-20} (T/300)^{1.58}$		40
170	$\text{OH} + \text{H} \rightarrow \text{H}_2\text{O} + \gamma$	$k_{170} = 5.26 \times 10^{-18} (T/300)^{-5.22} \exp\left(-\frac{90}{T}\right)$		40
171	$\text{H} + \gamma \rightarrow \text{H}^+ + \text{e}^-$	$k_{171} = \int \text{dE} J(\text{E}) \sigma_{\text{v}96}(E, 0.4298, 54750, 32.88, 2.963, 0, 0, 0)$		10
172	$\text{He} + \gamma \rightarrow \text{He}^+ + \text{e}^-$	$k_{172} = \int \text{dE} J(\text{E}) \sigma_{\text{v}96}(E, 13.61, 949.2, 1.469, 3.188, 2.039, 0.4434, 2.136)$		10
173	$\text{He}^+ + \gamma \rightarrow \text{He}^{++} + \text{e}^-$	$k_{173} = \int \text{dE} J(\text{E}) \sigma_{\text{v}96}(E, 1.72, 13690, 32.88, 2.963, 0, 0, 0)$		10
174	$\text{O} + \gamma \rightarrow \text{O}^+ + \text{e}^-$	$k_{174} = \int \text{dE} J(\text{E}) \sigma_{\text{v}96}(E, 1.24, 1745, 3.784, 17.64, 0.07589, 8.698, 0.1271)$		10
175	$\text{C} + \gamma \rightarrow \text{C}^+ + \text{e}^-$	$k_{175} = \text{table}$		43
176	$\text{H}_2 + \gamma \rightarrow \text{H}_2^+ + \text{e}^-$	$k_{176} = \text{table}$		43
177	$\text{H}^- + \gamma \rightarrow \text{H} + \text{e}^-$	$k_{177} = \text{table}$		43
178	$\text{CH} + \gamma \rightarrow \text{C} + \text{H}$	$k_{178} = \text{table}$		43
179	$\text{CH} + \gamma \rightarrow \text{CH}^+ + \text{e}^-$	$k_{179} = \text{table}$		43
180	$\text{C}_2 + \gamma \rightarrow \text{C} + \text{C}$	$k_{180} = \text{table}$		43
181	$\text{OH} + \gamma \rightarrow \text{O} + \text{H}$	$k_{181} = \text{table}$		43
182	$\text{OH} + \gamma \rightarrow \text{OH}^+ + \text{e}^-$	$k_{182} = \text{table}$		43
183	$\text{H}_2\text{O} + \gamma \rightarrow \text{OH} + \text{H}$	$k_{183} = \text{table}$		43
184	$\text{H}_2\text{O} + \gamma \rightarrow \text{H}_2\text{O}^+ + \text{e}^-$	$k_{184} = \text{table}$		43
185	$\text{O}_2 + \gamma \rightarrow \text{O}_2^+ + \text{e}^-$	$k_{185} = \text{table}$		43
186	$\text{O}_2 + \gamma \rightarrow \text{O} + \text{O}$	$k_{186} = \text{table}$		43
187	$\text{H}_2 + \gamma \rightarrow \text{H}^+ + \text{H} + \text{e}^-$	$k_{187} = \text{table}$		43
188	$\text{CO} \rightarrow \text{C} + \text{O}$	$k_{188} = (\text{see sec. 2.3})$		44
189	$\text{H}_2 \rightarrow \text{H} + \text{H}$	$k_{189} = (\text{see sec. 2.3})$		44

Table A1 – *continued*

No.	Reaction	Rate coefficient	Notes	Ref.
190	$\text{H}_2^+ \rightarrow \text{H} + \text{H}^+$	$k_{190} = 1.1 \times 10^{-9} G_0 \exp(-1.9A_v)$		45
191	$\text{H}_3^+ \rightarrow \text{H}_2 + \text{H}^+$	$k_{191} = 4.9 \times 10^{-13} G_0 \exp(-1.8A_v)$		46
192	$\text{H}_3^+ \rightarrow \text{H}_2^+ + \text{H}$	$k_{192} = 4.9 \times 10^{-13} G_0 \exp(-2.3A_v)$		46
193	$\text{C}^- \rightarrow \text{C} + \text{e}^-$	$k_{193} = 2.4 \times 10^{-7} G_0 \exp(-0.9A_v)$		32
194	$\text{CH}^+ \rightarrow \text{C} + \text{H}^+$	$k_{194} = 2.6 \times 10^{-10} G_0 \exp(-2.5A_v)$		47
195	$\text{CH}_2 \rightarrow \text{CH} + \text{H}$	$k_{195} = 7.1 \times 10^{-10} G_0 \exp(-1.7A_v)$		47
196	$\text{CH}_2 \rightarrow \text{CH}_2^+ + \text{e}^-$	$k_{196} = 5.9 \times 10^{-10} G_0 \exp(-2.3A_v)$		32
197	$\text{CH}_2^+ \rightarrow \text{CH}^+ + \text{H}$	$k_{197} = 4.6 \times 10^{-10} G_0 \exp(-1.7A_v)$		48
198	$\text{CH}_3^+ \rightarrow \text{CH}_2^+ + \text{H}$	$k_{198} = 10^{-9} G_0 \exp(-1.7A_v)$		32
199	$\text{CH}_3^+ \rightarrow \text{CH}^+ + \text{H}_2$	$k_{199} = 10^{-9} G_0 \exp(-1.7A_v)$		32
200	$\text{O}^- \rightarrow \text{O} + \text{e}^-$	$k_{200} = 2.4 \times 10^{-7} G_0 \exp(-0.5A_v)$		32
201	$\text{OH}^+ \rightarrow \text{O} + \text{H}^+$	$k_{201} = 10^{-12} G_0 \exp(-1.8A_v)$		46
202	$\text{H}_2\text{O}^+ \rightarrow \text{H}_2^+ + \text{O}$	$k_{202} = 5 \times 10^{-11} G_0 f_{\text{H}_n\text{O}^+}(A_v)$		49
203	$\text{H}_2\text{O}^+ \rightarrow \text{H}^+ + \text{OH}$	$k_{203} = 5 \times 10^{-11} G_0 f_{\text{H}_n\text{O}^+}(A_v)$		49
204	$\text{H}_2\text{O}^+ \rightarrow \text{O}^+ + \text{H}_2$	$k_{204} = 5 \times 10^{-11} G_0 f_{\text{H}_n\text{O}^+}(A_v)$		49
205	$\text{H}_2\text{O}^+ \rightarrow \text{OH}^+ + \text{H}$	$k_{205} = 1.5 \times 10^{-10} G_0 f_{\text{H}_n\text{O}^+}(A_v)$		49
206	$\text{H}_3\text{O}^+ \rightarrow \text{H}^+ + \text{H}_2\text{O}$	$k_{206} = 2.5 \times 10^{-11} G_0 f_{\text{H}_n\text{O}^+}(A_v)$		49
207	$\text{H}_3\text{O}^+ \rightarrow \text{H}_2^+ + \text{OH}$	$k_{207} = 2.5 \times 10^{-11} G_0 f_{\text{H}_n\text{O}^+}(A_v)$		49
208	$\text{H}_3\text{O}^+ \rightarrow \text{H}_2\text{O}^+ + \text{H}$	$k_{208} = 7.5 \times 10^{-12} G_0 f_{\text{H}_n\text{O}^+}(A_v)$		49
209	$\text{H}_3\text{O}^+ \rightarrow \text{OH}^+ + \text{H}_2$	$k_{209} = 2.5 \times 10^{-11} G_0 f_{\text{H}_n\text{O}^+}(A_v)$		49
210	$\text{H} \xrightarrow{\text{CR}} \text{H}^+ + \text{e}^-$	$k_{210} = 0.46 \zeta_{\text{H}_1}$		40
211	$\text{He} \xrightarrow{\text{CR}} \text{He}^+ + \text{e}^-$	$k_{211} = 0.5 \zeta_{\text{H}_1}$		40
212	$\text{O} \xrightarrow{\text{CR}} \text{O}^+ + \text{e}^-$	$k_{212} = 2.8 \zeta_{\text{H}_1}$		40
213	$\text{CO} \xrightarrow{\text{CR}} \text{C} + \text{O}$	$k_{213} = 5 \zeta_{\text{H}_1}$		40
214	$\text{CO} \xrightarrow{\text{CR}} \text{CO}^+ + \text{e}^-$	$k_{214} = 3 \zeta_{\text{H}_1}$		40
215	$\text{C}_2 \xrightarrow{\text{CR}} \text{C} + \text{C}$	$k_{215} = 237 \zeta_{\text{H}_1}$		40
216	$\text{H}_2 \xrightarrow{\text{CR}} \text{H} + \text{H}$	$k_{216} = 0.1 \zeta_{\text{H}_1}$		40
217	$\text{H}_2 \xrightarrow{\text{CR}} \text{H}^+ + \text{H}^-$	$k_{217} = 0.0003 \zeta_{\text{H}_1}$		40
218	$\text{H}_2 \xrightarrow{\text{CR}} \text{H}_2^+ + \text{e}^-$	$k_{218} = 0.93 \zeta_{\text{H}_1}$		40
219	$\text{C} \xrightarrow{\text{CR}} \text{C}^+ + \text{e}^-$	$k_{219} = 1020 \zeta_{\text{H}_1}$		40
220	$\text{CH} \xrightarrow{\text{CR}} \text{C} + \text{H}$	$k_{220} = 730 \zeta_{\text{H}_1}$		40
221	$\text{O}_2 \xrightarrow{\text{CR}} \text{O} + \text{O}$	$k_{221} = 750 \zeta_{\text{H}_1}$		40
222	$\text{O}_2 \xrightarrow{\text{CR}} \text{O}_2^+ + \text{e}^-$	$k_{222} = 117 \zeta_{\text{H}_1}$		40
223	$\text{OH} \xrightarrow{\text{CR}} \text{O} + \text{H}$	$k_{223} = 510 \zeta_{\text{H}_1}$		40
224	$\text{CH}_2 \xrightarrow{\text{CR}} \text{CH}_2^+ + \text{e}^-$	$k_{224} = 500 \zeta_{\text{H}_1}$		40
225	$\text{H}_2\text{O} \xrightarrow{\text{CR}} \text{OH} + \text{H}$	$k_{225} = 970 \zeta_{\text{H}_1}$		40
226	$\text{HCO} \xrightarrow{\text{CR}} \text{CO} + \text{H}$	$k_{226} = 421 \zeta_{\text{H}_1}$		40
227	$\text{HCO} \xrightarrow{\text{CR}} \text{HCO}^+ + \text{e}^-$	$k_{227} = 1170 \zeta_{\text{H}_1}$		40
228	$\text{H}_2 \xrightarrow{\text{CR}} \text{H} + \text{H}^+ + \text{e}^-$	$k_{228} = 0.93 \zeta_{\text{H}_1}$		40
229	$\text{C} + \text{C} + \text{M} \rightarrow \text{C}_2 + \text{M}$	$k_{229} = 5.99 \times 10^{-33} (T/5000)^{-1.6} n_{\text{Htot}}$ $= 5.99 \times 10^{-33} (T/5000)^{-0.64} \exp\left(\frac{5255}{T}\right) n_{\text{Htot}}$	$T < 5000 \text{ K}$ $T > 5000 \text{ K}$	87
230	$\text{C} + \text{O} + \text{M} \rightarrow \text{CO} + \text{M}$	$k_{230} = 6.16 \times 10^{-29} (T/300)^{-3.08} n_{\text{Htot}}$ $= 2.14 \times 10^{-29} (T/300)^{-3.08} \exp\left(\frac{2114}{T}\right) n_{\text{Htot}}$	$T < 2000 \text{ K}$ $T > 2000 \text{ K}$	50
231	$\text{C}^+ + \text{O} + \text{M} \rightarrow \text{CO}^+ + \text{M}$	$k_{231} = 6.16 \times 10^{-27} (T/300)^{-3.08} n_{\text{Htot}}$ $= 2.14 \times 10^{-27} (T/300)^{-3.08} \exp\left(\frac{2114}{T}\right) n_{\text{Htot}}$	$T < 2000 \text{ K}$ $T > 2000 \text{ K}$	51
232	$\text{C} + \text{O}^+ + \text{M} \rightarrow \text{CO}^+ + \text{M}$	$k_{232} = 6.16 \times 10^{-27} (T/300)^{-3.08} n_{\text{Htot}}$ $= 2.14 \times 10^{-27} (T/300)^{-3.08} \exp\left(\frac{2114}{T}\right) n_{\text{Htot}}$	$T < 2000 \text{ K}$ $T > 2000 \text{ K}$	51
233	$\text{H} + \text{O} + \text{M} \rightarrow \text{OH} + \text{M}$	$k_{233} = 4.33 \times 10^{-32} (T/300)^{-1} n_{\text{Htot}}$		52
234	$\text{OH} + \text{H} + \text{M} \rightarrow \text{H}_2\text{O} + \text{M}$	$k_{234} = 2.56 \times 10^{-31} (T/300)^{-2} n_{\text{Htot}}$		50
235	$\text{O} + \text{O} + \text{M} \rightarrow \text{O}_2 + \text{M}$	$k_{235} = 9.2 \times 10^{-34} (T/300)^{-1} n_{\text{Htot}}$		53



Table A1 – continued

No.	Reaction	Rate coefficient	Notes	Ref.
236	$\text{H} + \text{H} \xrightarrow{\text{dust}} \text{H}_2$	$k_{236} = (\text{see sec. 2.5})$		54
237	$\text{CO}_{(\text{gas})} \rightarrow \text{CO}_{(\text{ice})}$	$k_{237} = (\text{see sec. 2.6})$		
238	$\text{CO}_{(\text{ice})} \rightarrow \text{CO}_{(\text{gas})}$	$k_{238} = (\text{see sec. 2.6})$		
239	$\text{H}_2\text{O}_{(\text{gas})} \rightarrow \text{H}_2\text{O}_{(\text{ice})}$	$k_{239} = (\text{see sec. 2.6})$		
240	$\text{H}_2\text{O}_{(\text{ice})} \rightarrow \text{H}_2\text{O}_{(\text{gas})}$	$k_{240} = (\text{see sec. 2.6})$		

**Parameters:**

$$\begin{aligned}
 T_e &= 8.617343 \times 10^{-5} T, \quad T_e \text{ is the temperature measured in eV} \\
 k_{l,\text{H}} &= 6.67 \times 10^{-12} \sqrt{T} \exp\left(-\left(1 + 63590 \frac{1}{T}\right)\right) \\
 k_{h,\text{H}} &= 3.52 \times 10^{-9} \exp\left(-43900 \frac{1}{T}\right) \\
 n_{\text{crit,H}} &= 10^{\left(3 - 0.416 \ln\left(\frac{T}{10000}\right) - 0.327 \ln\left(\frac{T}{10000}\right)^2\right)} \\
 k_{l,\text{H}_2} &= \frac{5.996 \times 10^{-30} T^{4.1881}}{(1 + 6.761 \times 10^{-6} T)^{5.6881}} \exp\left(-54657.4 \frac{1}{T}\right) \\
 k_{h,\text{H}_2} &= 1.3 \times 10^{-9} \exp\left(-53300 \frac{1}{T}\right) \\
 n_{\text{crit,H}_2} &= 10^{\left(4.845 - 1.3 \ln\left(\frac{T}{10000}\right) + 1.62 \ln\left(\frac{T}{10000}\right)^2\right)} \\
 k_{l,\text{He}} &= 10^{\left(-27.029 + 3.801 \log(T) - 29487/T\right) a_{\text{He}}} \\
 k_{h,\text{He}} &= 10^{\left(-2.729 - 1.75 \log(T) - 23474/T\right) (1 - a_{\text{He}})} \\
 n_{\text{crit,He}} &= 10^{\left(5.0792 \left(1 - 1.23 \times 10^{-5} (T - 2000)\right)\right)} \\
 a_{\text{He}} &= (1 + n_{\text{Htot}}/n_{\text{crit,He}})^{-1} \\
 \sigma_{\nu 96}(E, E_0, \sigma_0, y_a, P, y_w, y_0, y_1) &= 10^{-18} \sigma_0 \left((x-1)^2 + y_w\right) y^{0.5P-5.5} \left(1 + \sqrt{y/y_a}\right)^{-P} \\
 x &= \frac{E}{E_0} - y_0 \\
 y &= \sqrt{x^2 + y_1^2}
 \end{aligned}$$

**References:** (1) Janev et al. (1987), (2) Abel et al. (1997); Ferland et al. (1992), (3) Cen (1992b); Aldrovandi & Pequignot (1973), (4) Aladdin database<sup>a</sup>; Abel et al. (1997), (5) Yoshida et al. (2006), (6) Glover & Jappsen (2007), (7) Omukai (2000), (8) Millar et al. (1997), (9) Harada et al. (2010), (10) Verner et al. (1996), (11) Kreckel et al. (2010), (12) Coppola et al. (2011); Ramaker & Peek (1976), (13) Karpas et al. (1979), (14) Grassi et al. (2011); Savin et al. (2004), (15) Mitchell & Deveau (1983); Corrigan (1965), (16) Lepp & Shull (1983); Glover et al. (2010), (17) Abel et al. (1997); Janev et al. (1987), (18) Stenrup et al. (2009), (19) Poulaert et al. (1978), (20) Abel et al. (1997); Schneider et al. (1994), (21) Dalgarno & Lepp (1987), (22) Glover et al. (2010), (23) Forrey (2013), (24) Glover & Abel (2008), (25) Nahar & Pradhan (1997), (26) Nahar (1999), (27) Voronov (1997), (28) Stancil et al. (1999), (29) Stancil et al. (1998), (30) Zhao et al. (2004), (31) Kimura et al. (1993), (32) Le Teuff et al. (2000), (33) Smith et al. (2002), (34) Anicich (2003), (35) Dean et al. (1991), (36) Harding et al. (1993), (37) Loison et al. (2014), (38) Murrell & Rodriguez (1986), (39) UMIST database<sup>b</sup> (McElroy et al. 2013), (40) KIDA database<sup>c</sup> (Wakelam et al. 2012), (41) Baulch et al. (2005), (42) O'Connor et al. (2015), (43) PHIDRATES database<sup>d</sup> (Huebner et al. 1992), (44) Richings et al. (2014b), (45) Dunn (1968), (46) van Dishoeck (1987), (47) Roberge et al. (1991), (48) van Dishoeck et al. (2006), (49) Sternberg & Dalgarno (1995), (50) Baulch et al. (1992), (51) Petuchowski et al. (1989), (52) Tsang & Hampson (1986a), (53) Warnatz (1984), (54) Cazaux & Spaans (2009); Grassi et al. (2017), (55) Walkauskas & Kaufman (1975), (56) Tsang & Hampson (1986b), (57) Smith et al. (2004), (58) Cohen & Westberg (1979), (59) Azatyan, Aleksandrov & Troshin (Azatyan et al.), (60) Linder et al. (1995), (61) Sidhu et al. (1992), (62) Adams et al. (1984), (63) McEwan et al. (1999), (64) Viggiano et al. (1980), (65) Smith & Adams (1977); Adams & Smith (1977), (66) Jones et al. (1981), (67) Rakshit & Warneck (1980), (68) Smith et al. (1992), (69) Federer et al. (1984), (70) Peart & Hayton (1994), (71) Woodall et al. (2007); McCall et al. (2004), (72) Takagi et al. (1991), (73) Larson et al. (1998), (74) Mitchell (1990), (75) Guberman (1995), (76) Rosén et al. (2000), (77) Jensen et al. (2000), (78) Alge et al. (1983), (79) Rosén et al. (1998), (80) Geppert et al. (2005), (81) Gerlich & Horning (1992), (82) Stancil & Dalgarno (1998), (83) Prasad & Huntress (1980), (84) Andreazza & Singh (1997), (85) Singh et al. (1999), (86) Barinovs & van Hemert (2006), (87) Le Teuff et al. (2000); Fairbairn (1969); Slack (1976), (88) Glover & Savin (2009)

<sup>a</sup> <https://www-amdis.iaea.org/ALADDIN>

<sup>b</sup> <http://udfa.ajmarkwick.net>

<sup>c</sup> <http://kida.obs.u-bordeaux1.fr>

<sup>d</sup> <http://phidrates.space.swri.edu>